Characterizing High-Energy Electrons in Space Using Science Imagers

by

Ashley Kelly Carlton

B.S., Wake Forest University (2011)

S.M., Massachusetts Institute of Technology (2016)

Submitted to the Department of Aeronautics and Astronautics
in partial fulfillment of the requirements for the degree of
Doctor of Philosophy in Aeronautics and Astronautics
at the
MASSACHUSETTS INSTITUTE OF TECHNOLOGY

September 2018

Author .... Signature redacted
Department of Aeronautics and Astronautics
August 13, 2018

Certified by .... Signature redacted
Kerri Cahoy
Associate Professor of Aeronautics and Astronautics
Thesis Supervisor

Certified by .... Signature redacted
Daniel Hastings
Professor of Aeronautics and Astronautics

Certified by .... Signature redacted
Insoo Jun
Technical Group Supervisor, NASA Jet Propulsion Laboratory

Certified by .... Signature redacted
Harlan Spence
Professor, University of New Hampshire

Accepted by .... Signature redacted ....
Hamsa Balakrishnan
Chairman, Department Committee on Graduate Theses

Characterizing High-Energy Electrons in Space Using Science Imagers

by

Ashley Kelly Carlton

Submitted to the Department of Aeronautics and Astronautics
on August 13, 2018, in partial fulfillment of the
requirements for the degree of
Doctor of Philosophy in Aeronautics and Astronautics

Abstract

Harsh radiation in the form of ionized, highly energetic particles is part of the space environment and can affect the operation, performance, and lifetime of spacecraft and their instruments. Jupiter has the largest and strongest magnetosphere of all of the planets in the solar system and it is dominated by high-energy electrons. Measuring and characterizing megaelectron volt (MeV) particles is fundamental for understanding the energetic processes powering the magnetosphere, interactions of the particles with surfaces of the Jovian satellites, and the effects of these particles on spacecraft near or in Jovian orbit. Electrons in Jupiter's magnetosphere can interact with spacecraft and lead to component failures, degradation of sensors and solar panels, and physical damage to materials.

Dedicated instruments to monitor the radiation environment are not always included on spacecraft due to resource constraints. Measurements of the high-energy (>1 MeV) electron environment at Jupiter are currently spatially and temporally limited, predominantly coming from the Energetic Particle Detector (EPD) on the Galileo spacecraft. In this thesis, we develop ways to use existing hardware on spacecraft to measure the energetic particle environment. Solid-state detectors are commonly used as scientific imagers on spacecraft. In addition to being sensitive to incoming photons, semiconductor devices also are affected by incoming charged particles collected during integration and detector readout. These radiation hits from the space environment are typically considered "noise" at the detector.

We develop a technique to extract quantitative high-energy electron environment information (energy and flux) from science imager radiation "noise". We use data from the Galileo spacecraft Solid-State Imaging (SSI) instrument, which is a silicon charge-coupled device (CCD). We post-process raw SSI images to obtain frames with only the radiation contribution. The camera settings are used to compute the energy deposited in each pixel, which corresponds to the intensity of the observed radiation hits. The energy deposited in the SSI pixels by incident particles from processed SSI images are compared with the results from 3D Monte Carlo transport simulations of the SSI using Geant4.

Simulating the response of the SSI instrument to mono-energetic electron environments, we find that the SSI is capable of detecting ≥10 MeV electrons (>90% of <10 MeV particles are stopped with 95% confidence). Using geometric scaling factors computed for the SSI, we calculate the environment particle flux given a number of pixels with radiation hits. We compare the SSI results to measurements from the Galileo EPD, examining the electron fluxes from the >11 MeV integral flux channel. We find agreement with the EPD data within 3-sigma of the EPD data for 43 out of 43 (100%) of the SSI images evaluated. 62% of fluxes are also within 1-sigma of the EPD data.

To demonstrate that the general technique is applicable to other imagers, we also analyze the Galileo Near-Infrared Mapping Spectrometer (NIMS). We find that NIMS is sensitive to ≥5 MeV electrons and the calculated fluxes are consistent with the EPD. This approach can be applied to other sets of imaging data (star trackers, etc.) in energetic electron environments, such as those found in geostationary Earth orbit. This thesis also includes a summary of required and recommended information (tests, models, etc.) for the use of science imagers as high-energy electron sensors.

Thesis Supervisor: Kerri Cahoy
Title: Associate Professor of Aeronautics and Astronautics

Acknowledgments

I would like to first acknowledge and thank my role model and advisor, Kerri Cahoy. Her intelligence, initiative, and compassion both in and out of the classroom serves as an outstanding example to her students. I would also like to thank Insoo Jun, Harlan Spence, Dan Hastings, Maria de Soria-Santacruz Pich, Paul Withers, and Greg Ginet for their technical guidance.

I would like to acknowledge my mentors and fellow students at the MIT SSL and STAR Lab and my colleagues at NASA JPL for their continued friendship and support: Farah, Annie, Whitney, Angie, Emily, Kit, Kat, Tam, Hyosang, Raichelle, Greg, Rachel, Marilyn, Beth, all of JPL group 5132, Wousik, Hank, Ken, Bogdan, Mitch, and Peg.

Lastly, I'd like to thank my family for their relentless encouragement and their sense of perspective. Their day to day support is in a large part responsible for my success and sanity: Dad and Sara, Mom and Gary, Kels and Fares, little 'C', Seana, Mike, Matt, Weston, KUSC

Thank you.

Contents

List of Figures

List of Tables

Acronyms

CCD Charge-coupled Device

CMOS Complementary Metal-oxide-semiconductor

DN Data (or Digital) Number

EDR Experiment Data Record

EPD Energetic Particle Detector

ESD Electrostatic Discharge

eV Electron-Volt

GEO Geostationary Earth Orbit

GIRE2 Galileo Interim Radiation Electron Model Version 2

GOES Geostationary Operational Environmental Satellite

HGA High-gain Antenna

IESD Internal Electrostatic Discharge

MCP Micro-channel (or Multi-channel) Plate

NIMS Near-Infrared Mapping Spectrometer

PDS Planetary Data System

SSI Solid-State Imaging

TID Total Ionizing Dose

Chapter 1

Introduction

1.1 Background

Harsh radiation in the form of ionized, highly energetic particles is part of the space environment. These particles sweep through the solar system in the solar wind and solar storms, are ejected from supernovae, and are also trapped as belts in planetary magnetic fields. A planetary magnetosphere is the region of space surrounding the planet in which the physical phenomena of electrically-charged particles is controlled by the magnetic field. The charged particles can affect spacecraft and satellites orbiting the planet.

Jupiter's magnetosphere is the largest and strongest of any planet in the solar system. Similar to Earth, Jupiter is approximately a magnetic dipole with a tilt of $\sim 11°$[46, 70], but Jupiter's magnetic field strength is more than an order of magnitude larger than Earth's and its magnetic moment is ~19,000 times larger [6, 96]. The magnetic field at the equator is proportional to the magnetic moment divided by the cube of the radial distance. Therefore, Jupiter's magnetic field is proportionally about twenty times stronger than Earth's magnetic field. Table 1.1 summarizes the comparison between Jupiter and Earth. The larger field strength means that Jupiter's magnetosphere can contain significantly more charged particles than Earth. Looking at Figure 1-1, the bow shock extends about 84 R_J towards the Sun (where R_J = 71,492 km is the radius of Jupiter), and the magnetotail can extend almost as far

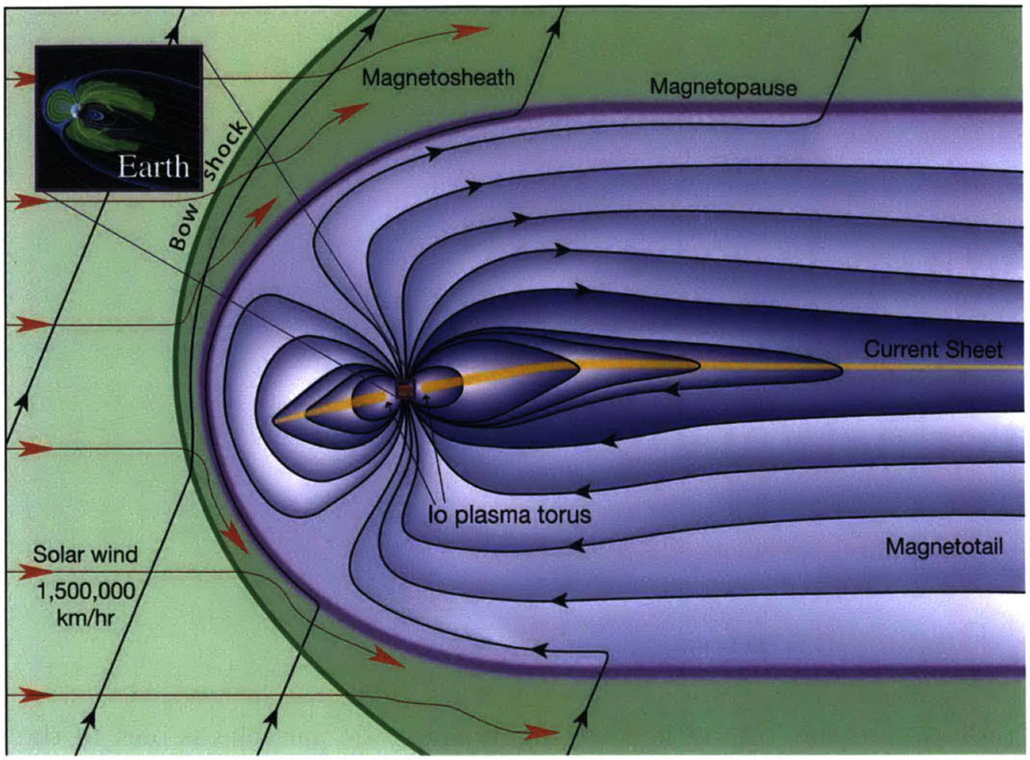

Figure 1-1: Structure of the Jovian magnetosphere. The magnetosphere is the dominating influence on energetic particles in the purple region. Earth's magnetosphere, shown in the top left corner, can fit inside Jupiter's radius. Image source: [5].

in the other direction as Saturn's orbit (~50-1000 R_J, or up to ~71 million km) [69, 77]. Jupiter's magnetosphere is thought to be powered by a liquid dynamo circulating metallic hydrogen. Eruptions of sulfur and oxygen from the Galilean moon Io's volcanoes form a cold torus that rotates with Jupiter at 5.9 R_J, generating ions through collisions and ultraviolet radiation, altering the dynamics of and supplying mass to the magnetosphere [63, 70, 97]. Figure 1-2 shows the relative locations of the Galilean moons of Jupiter. The particle number density of the plasma in the Io torus is about 2,000 particles per cubic centimeter and the effects from Io's plasma torus extend out to ~50 R_J [69]. At Earth, the only internal source of plasma is the ionosphere, so the cold plasma population falls off exponentially to just a few particles per cubic centimeter at 4-5 R_E (1 R_E = 6,371 km).

The rotation rate of Jupiter (~10 hours) is much faster than that of Earth (24 hours). The fast rotation at Jupiter, coupled with the strong magnetic field, forces cold plasma to expand by centrifugal force into a giant disk. The trapped cold plasma

Table 1.1: Comparison between Earth and Jupiter. The number of moons listed for Jupiter is from last reported count by [102].

Planet Parameter	Earth	Jupiter
Equatorial Radius [km]	6.38×10^3	7.15×10^4
Magnetic Moment [G-cm^3]	8.10×10^{25}	1.59×10^{30}
Dipole Tilt [°]	11.5	11
Rotation Period [hr]	24.0	9.9
Aphelion / Perihelion [AU]	1.01 / 0.98	5.45 / 4.95
Number of Moons	1	69

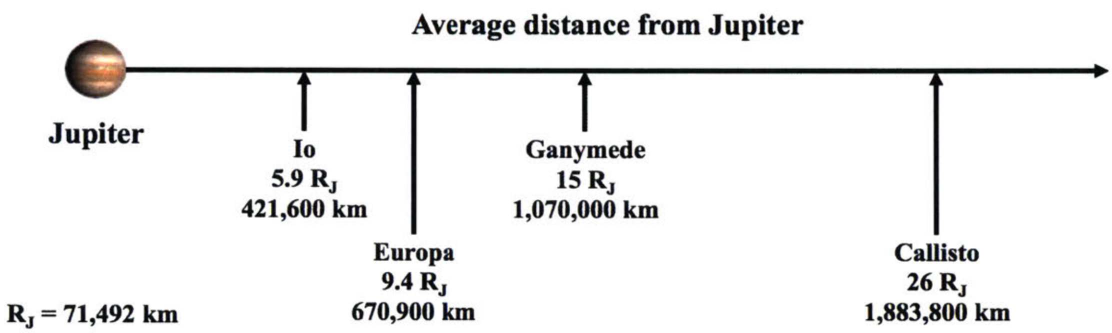

Figure 1-2: Relative locations of the four Galilean moons of Jupiter. The distances are to scale with the size of Jupiter in the image. Note: There are four smaller, inner moons (Metis, Adrastea, Amalthea, and Thebe) at 1.8-3.1 R_J that are not pictured.

in the magnetosphere co-rotates at velocities much higher than a spacecraft's orbital velocity. This is the opposite at Earth, where (at low altitudes) spacecraft orbit faster than the ionospheric plasma. The co-rotation at Jupiter breaks down around 20 R_J [36]. The magnetic field tilt and rotation rate cause the plasma disk to fluctuate so that at a given location plasma and radiation parameters vary significantly during a 10-hour period.

The Jovian radiation environment is dominated by trapped high-energy electrons. The high-energy electron spectra extends to much higher energies (>10 MeV)[1] than the spectra found in Earth's magnetosphere [15, 32, 33, 47]. At Earth, the most

[1]An electron-Volt (eV) is the amount of energy gained (or lost) by the charge of a single electron moving across an electric potential difference of one volt. 1 MeV = 10^6 eV.

extreme electron environment is at the outer Van Allen belt (~4-5 R_E from Earth), where the >1 MeV integral flux is $\sim 8.8 \times 10^5\,\mathrm{cm}^{-2}\,\mathrm{s}^{-1}$.[2] At Jupiter, the >1 MeV electron flux at 6 R_J is $> 1 \times 10^8\,\mathrm{cm}^{-2}\,\mathrm{s}^{-1}$, which is over two orders of magnitude greater than at Earth, extending up to energies of 100 MeV and above [36, 46]. Figure 1-3 compares the electron and proton integral fluxes in Jovian orbit (at Europa) and in geostationary Earth orbit (GEO).

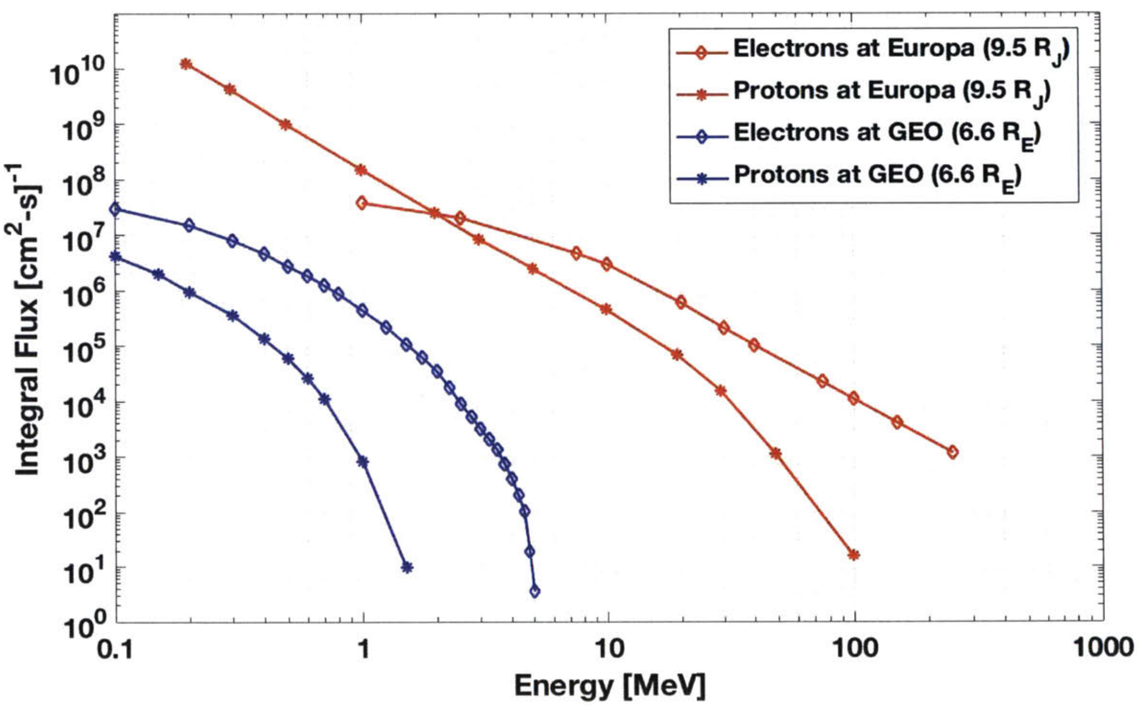

Figure 1-3: Comparison of the Jupiter (red) and Earth (blue) electron and proton spectra. The electron and proton spectra for Jupiter are using the GIRE2 model (see Section 1.3.2) at 9.5 R_J (at Europa). The Earth spectra is found using the AE-8 and AP-8 models at solar maximum at 6.6 R_E (at GEO) [100, 112].

[2]Found using the AE-8 model at solar maximum [112].

1.2 Characterizing the Jovian Radiation Environment

1.2.1 Science Motivation

Determining the composition of energetic particles is critical to our scientific understanding of the composition, structure, and dynamics of the magnetosphere. Increased temporal coverage and spatial measurements can improve current environment models, which are currently defined by limited data (see Section 1.3).

High-energy electrons affect the Jovian satellites (moons). The energetic electrons are a major contributor to exogenic processes, which affect the albedo and surface chemistry of the moon [25, 80, 89]. MeV electrons can penetrate through atmospheres, physically and chemically weathering the surfaces of moons. The penetration depths depend on the particle type, particle energy, and material, with particle doses at depths up to a few micrometers in rocky surfaces dominated by ions and at depths greater than ten micrometers by electrons [61, 62, 88]. The electrons are tens of keV to >25 MeV. The effects extend below the surface layer and are relatively permanent.

High-energy electrons can drive surface chemistry by ionization that catalyzes chemical reactions, which has direct impacts on the astrobiological potential of a satellite. Since metabolic reactions within living cells depend on chemical energy, it has been suggested that the Europa subsurface ocean has a high potential for sustaining biological activity if some oxidation-reduction chemistry is present [25, 52]. It is likely that Europa's briny subsurface ocean is a reducing environment and the irradiation of a surface by bombardment of charged particles leads to oxidation of the surface [28, 80].

1.2.2 Engineering Motivation

Knowledge of the high-energy radiation environment impacts spacecraft mission design, operations, and lifetime. Mission architectures are affected by trading mission lifetime against more desirable science that requires orbits closer to the planet with higher radiation exposure. For example, the Europa Clipper mission flower-petal

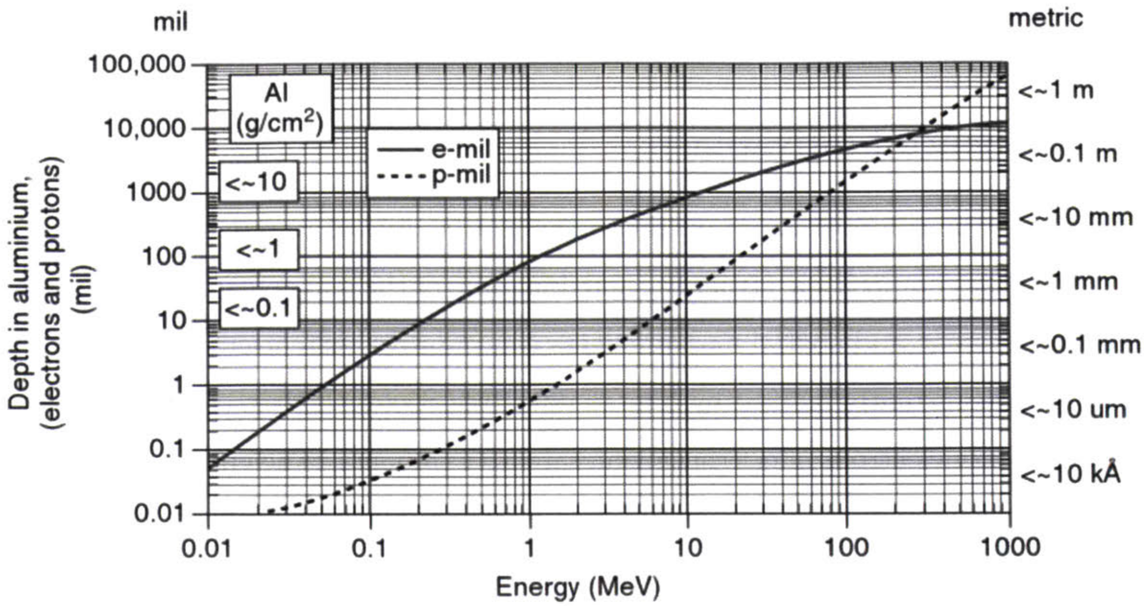

Figure 1-4: Electron (solid) and proton (dashed) penetration depth in aluminum for a range of energies (0.01 to 1000 MeV). For 100 mils (2.54 mm) of aluminum, protons must have energies above about 1 MeV and electrons must have energies above about 20 MeV to penetrate. Image source: Garrett and Whittlesey (2012) [44].

orbit is specifically designed to maximize science and mission life but minimize radiation exposure during the orbit [91]. For the Galileo spacecraft, during the nominal mission, the Solid-State Imaging (SSI) instrument only opened its shutter and took images when the spacecraft was greater than approximately 9 R_J from Jupiter to reduce radiation damage. When the mission was extended (three phases, from 1997 to 2003), the mission operators took greater risks, using the SSI instrument at 5.8 R_J, where the radiation environment is more intense.

The risk of anomalies and degradation to spacecraft are increased in high-energy electron environments (e.g., [8, 40, 54]). Internal (or bulk) charging occurs when MeV electrons penetrate satellite shielding materials and deposit charge on internal spacecraft components. For a spacecraft wall with a thickness of 100 mils (2.54 mm) of aluminum (typical for an Earth-orbiting spacecraft), electrons need energies in the range 0.5-5 MeV to penetrate, and protons need energies of 10-100 MeV (see Figure 1-4 from Garrett and Whittlesey (2012) [44]). If the component's resistivity is high, the rate of charge build-up can overcome the charge leakage rate of the material.

Table 1.2: Key effects of radiation on spacecraft and the high-energy particle populations that cause the radiation effects.

Radiation Effect	High-Energy Particles
Radiation dose, dose rate	100 keV - 50 MeV electrons
	1 MeV - 100 MeV protons
Surface charging, ESD	1 keV - 1 MeV electrons
Single event effects	1 - 100 MeV protons
	>1 MeV/Nuc. heavy ions
Internal charging, IESD	1 - 10+ MeV electrons

The induced electric field may then exceed the breakdown threshold for the material, causing electrostatic discharge (ESD) in the material [8, 38, 43, 117]. This can lead to anomalies such as component failures, degradation of sensors and solar panels, and serious physical damage to materials. Internal electrostatic discharge (IESD) can happen as a result of electron charges buried in dielectrics or on floating metals inside the spacecraft.

Total ionizing dose (TID) is a result of long-term radiation absorption and can lead to undesirable effects such as electron-hole pair production, transport, and trapping in the dielectric material. The total accumulated dose depends on orbit parameters (altitude, inclination, eccentricity), spacecraft orientation, and time. The integrated particle energy spectrum (fluence as a function of particle energy) is used to compute the TID. Figure 1-5 shows the dose depth curve for the Galileo mission as predicted by Galileo Interim Radiation Electron model version 2 (GIRE2). As TID increases, material and component degradation increases, leading to reduced functionality and greater susceptibility to failure. There is also evidence that dose rate affects the TID; electron-hole pair production, transport, and trapping in dielectrics can be more pronounced at lower dose rates (see Chen et al. (2010) for information on "enhanced low dose rate sensitivity" (ELDERS) and references therein [24]).

Increased information about the environment can supplement and refine models that are used for spacecraft design [33, 36]. The survivability and lifetime estimates

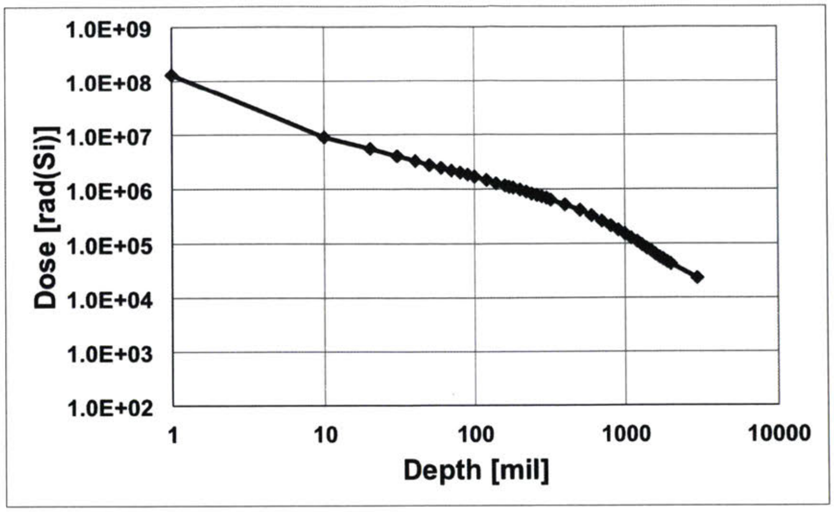

Figure 1-5: Dose depth curve for the Galileo mission through orbit 35, as predicted by GIRE2. Data are from I. Jun at NASA/JPL.

are developed based on the anticipated environment, influencing part selection (radiation tolerant or not), redundancy, shielding design (thickness, material, location), and software development (scrubbing, self-inspection, or not). This leads to significant impacts on mission cost and schedule, affecting the data that can be returned. For more information about mission design considerations in radiation environments, see Garrett and Whittlesey (2012) [44].

1.3 Particle Measurements at Jupiter

1.3.1 Limited High-Energy Electron Data

High-energy particle information about the Jovian magnetosphere is limited, both spatially and temporally. Table 1.3 shows a list of the spacecraft that have taken high-energy electron measurements at Jupiter. We limit the list to instruments capable of measuring >1 MeV electrons because it is the dominant species at Jupiter and the focus of this thesis. Figure 1-6 shows a plot of the orbit paths of the spacecraft that have recorded high-energy particle measurements with respect to Jupiter. Pioneer 10 and 11 and Voyager 1 and 2 made measurements during flybys in the 1970s and 1980s, respectively [110, 111, 113, 114]. For the most part, the information about the Jovian environment comes from the Galileo spacecraft Energetic Particle Detector (EPD) [116]. A top-down view of the Galileo orbits when the EPD made measurements can be found in Figure 1-7. While there were 35 orbits from ~5 R_J to over 100 R_J, the Galileo orbit was nearly equatorial around Jupiter, remaining within ±5° of the equatorial plane of Jupiter (see Figure 1-6). The axis of the magnetic field is tipped about eleven degrees from the planet's rotation axis, which causes Galileo to cross the magnetic equator roughly every five hours (Jupiter's rotation period is ten hours).

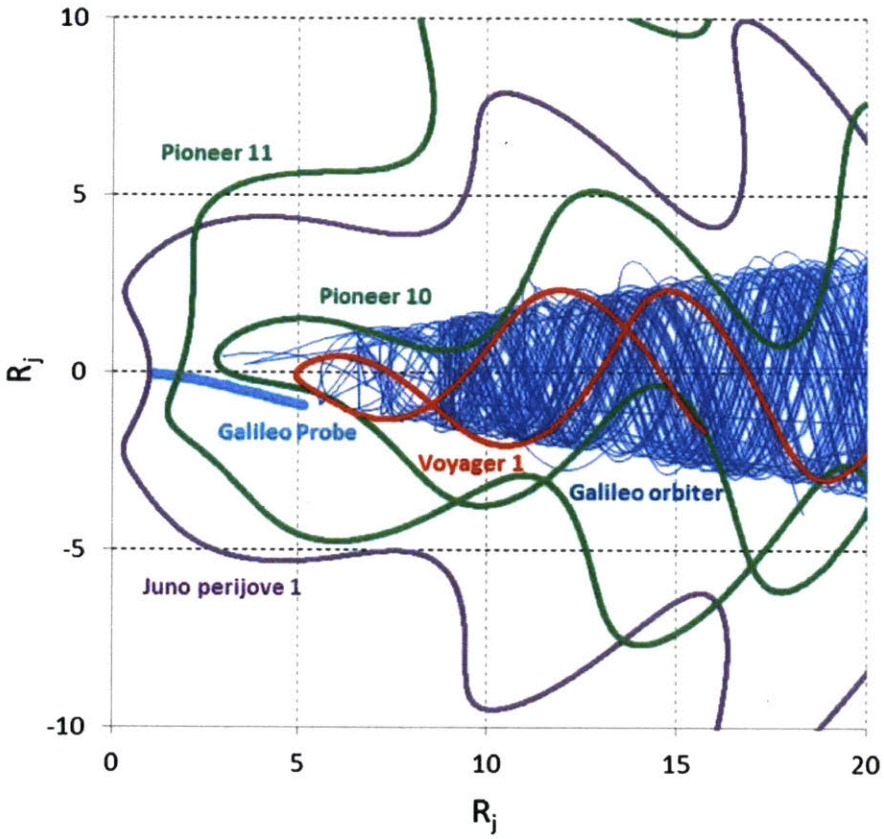

Figure 1-6: Map of the trajectories of spacecraft that have made high-energy measurements of Jupiter's magnetosphere in the magnetic dipole frame. The Pioneer 10 and 11 flybys are plotted in green. The Voyager 1 and 2 flybys are in red. The Galileo orbits are in blue. The first Juno perijove is in purple, for reference. Image source: Nénon et al. (2018) [84].

Table 1.3: Spacecraft that have made high-energy (>1 MeV) electron measurements at Jupiter. The instruments and energy ranges for each spacecraft are provided.

Spacecraft	Instruments	Electron Measurements
Pioneer 10 [110]	Geiger tube telescope (GTT)	>0.06, 0.55, 5, 21, 31 MeV
Pioneer 11 [111]	Trapped radiation detector (TRD)	>0.16, 0.26, 0.46, 5, 8, 12, 35 MeV
	Electron current detector (ECD)	>3.4 MeV
Voyager 1 [113]	Cosmic ray telescope (CRT)	3-110 MeV
Voyager 2 [114]		
Galileo [116]	Energetic particle detector (EPD)	>0.238, 0.416, 0.706, 1.5, 2.0, 11.0 MeV

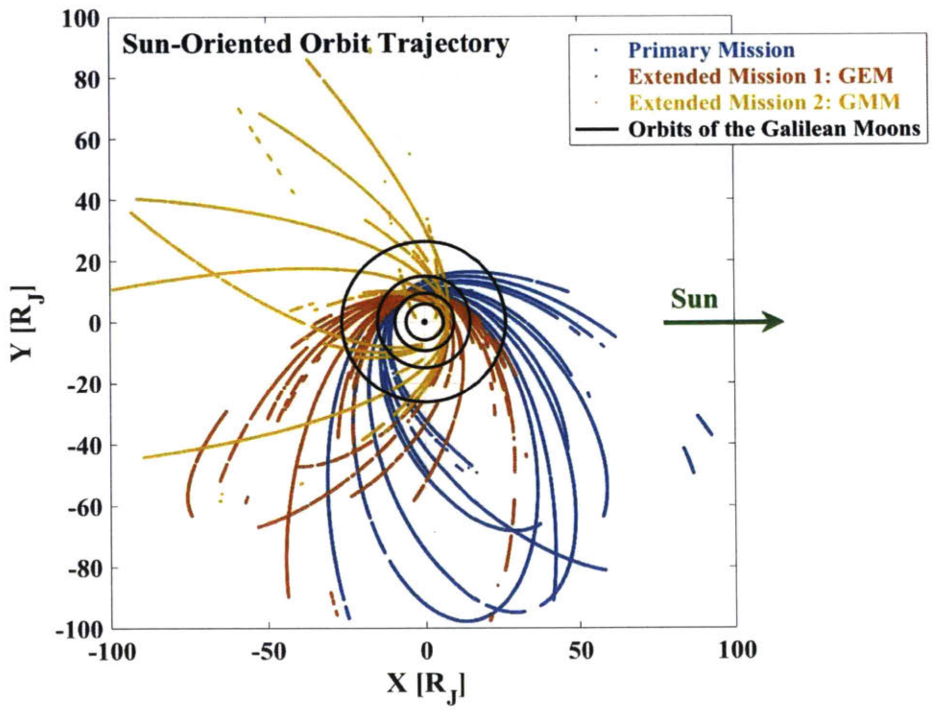

Figure 1-7: Polar view of the locations where Galileo EPD measurements were made in a sun-oriented frame (local time with Jupiter). Jupiter is the black dot in the center (to scale) and the four rings around it are the locations of the four Galilean moons.

1.3.2 Jovian Radiation Models

The first comprehensive model of the Jovian environment, which was the standard for decades, was the Divine and Garrett (D&G) model in 1983, which is built on empirical data from the Pioneer and Voyager spacecraft [36]. The D&G model was updated in 2005 to include synchrotron measurements from Earth-based observatories [47]. Presently, there are two models that are used as the standard. The Jovian Specification Environment (JOSE) model [104] by ONERA[3] in France, which is based on the Salammbô theoretical code [103] in combination with data from the Galileo EPD. The Galileo Interim Radiation Electron (GIRE) model combines the Galileo EPD dataset with the original D&G model (good coverage at $R_J < 8$ from the Pioneer and Voyager spacecraft) and synchrotron observations to estimate the trapped electron radiation environment [34]. The GIRE2 model addresses discontinuities at the boundary between the GIRE and D&G model and extends the model from ~16 R_J up to ~50 R_J [44, 45]. GIRE2 is the standard used in the United States and is the model used for comparison in this thesis. Table 1.4 provides an overview of the models.

1.3.3 Juno and Europa Clipper Missions

Juno, a NASA spacecraft that entered Jupiter orbit in July 2016, measures Jupiter's composition, gravity field, magnetic field, and polar magnetosphere. Nominal science operations started in December 2016. The science phase (altered from the original plan due to an early issue with the propulsion system) consists of 12 science perijoves (14 total perijoves) before the nominal end of mission in July 2018. An extended mission through July 2021 has recently been announced.[4] The Juno spacecraft orbits over the poles ($90 \pm 10°$ inclination) with a highly elliptical orbit, lasting approximately 53.5 days. The elongated orbit means that apojove reaches a distance of around 8 million kilometers, passing through Jupiter's magnetotail. Figure 1-8(a) shows the

[3] Office National d'Etudes et de Recherches Aérospatiales (ONERA) is the French national aerospace research center.

[4] `https://www.missionjuno.swri.edu/news/nasa-replans-junos-jupiter-mission`

Table 1.4: Overview of Jovian radiation models.

Model Name	References	Description and Comments
Divine and Garrett (D&G)	Divine and Garrett, 1983	First comprehensive model of the radiation and plasma environment around Jupiter, Empirical, from Geiger tube telescope (GTT) on Pioneer 10 and 11, and from the cosmic ray telescope on Voyager 1 and 2.
D&G, updated	Garrett et al., 2005	Includes data from Earth-based observations of the Jupiter synchrotron emissions
Jovian Specific Environment (JOSE)	ONERA, Sicard-Piet et al., 2011	Based on Salammbô theoretical code in combination with data from the Energetic Particle Detector (EPD) on the Galileo spacecraft
Galileo Interim Radiation Electron (GIRE) and GIRE2	Garrett et al., 2002 and 2012; de Soria-Santacruz et al., 2016	Empirical model, uses 10-min averages from the EPD on Galileo, V2 addresses discontinuities at the boundary between GIRE and the D&G models and extends from $\sim$16 R_J to $\sim$50 R_J.

tilt of Juno's orbit relative to Jupiter as the orbit precesses over time. At perijove, the closest approach ranges from 4,200 km to 7,900 km.

Measurements of the high-energy electron environment from a polar orbiter would greatly increase the spatial data coverage. Juno is equipped with detectors that can measure a maximum of 1 MeV for electrons and 3 MeV for protons. While these detectors cover the Juno primary science objectives, they do not cover the higher energies of concern (radiation dose, single event effects, internal electrostatic discharges) of up to 30 MeV electrons and 100 MeV protons, severely limiting the accuracy of total mission dose measurements. See Figure 1-9 for the energy detection ranges for Juno's Jovian Auroral Distribution Experiment (JADE) and the Jupiter Energetic-particle Detector Instrument (JEDI) compared to the energy ranges of concern for radiation-related effects.

A technique to extract high-energy electron information from science imagers already on Juno could yield important radiation environment information that would otherwise be unreported. Juno has three instruments that are charge-coupled devices

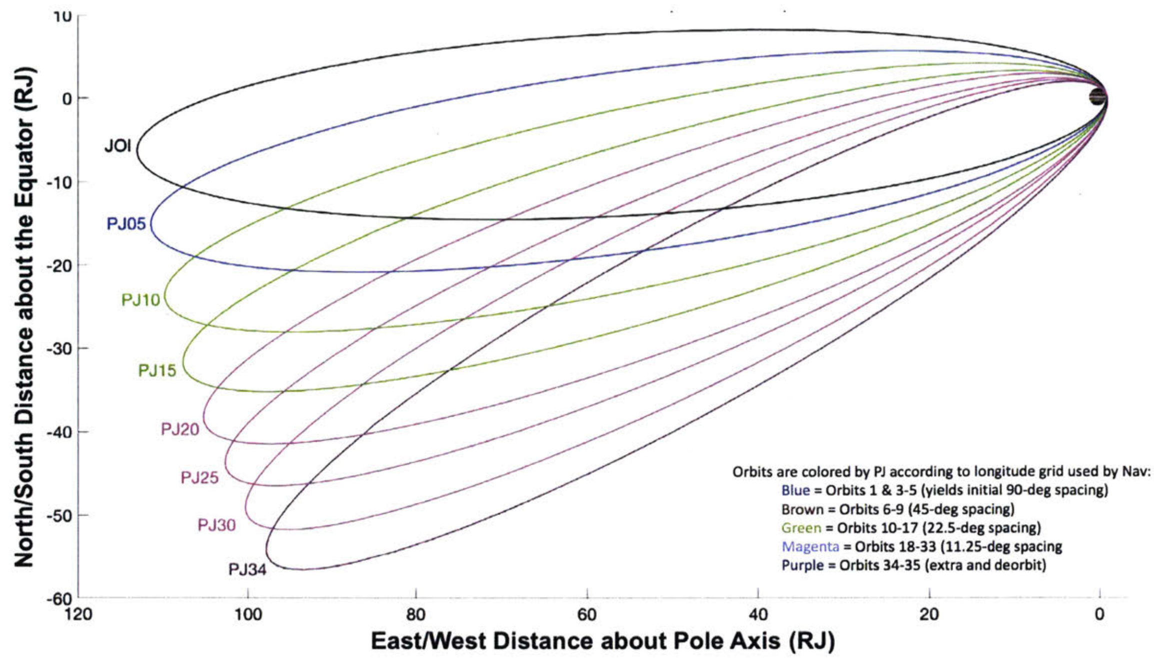

(a) Juno orbit paths as of June 2018.

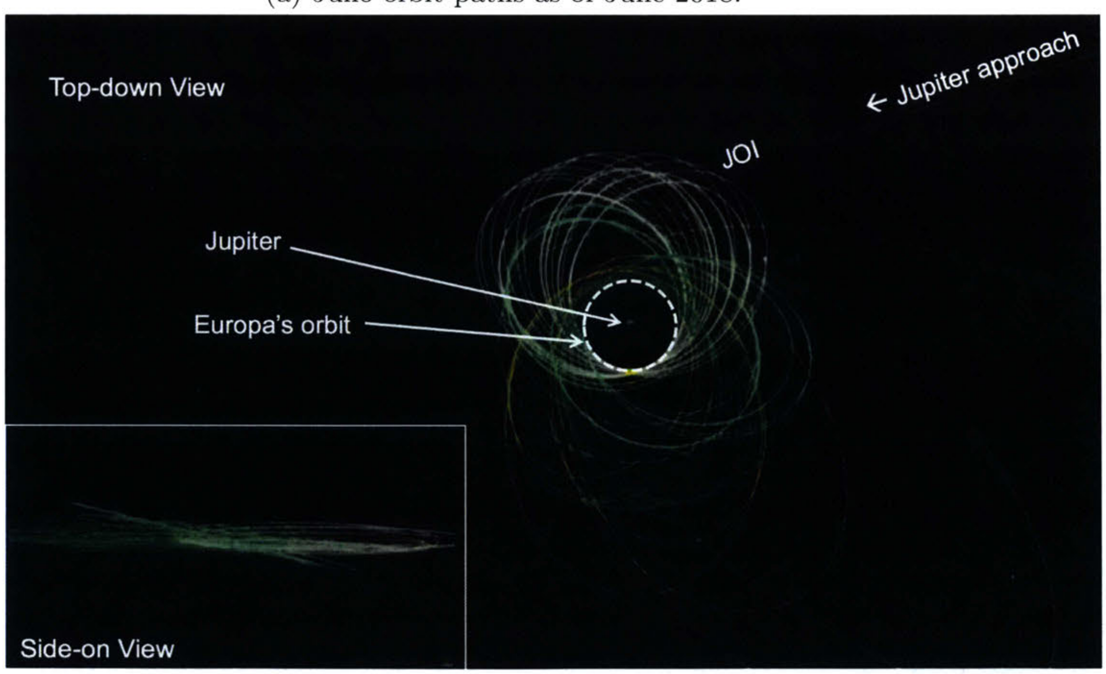

(b) Europa Clipper orbit plan.

Figure 1-8: Orbits of Juno as of June 2018 and the plans for Europa Clipper orbits on the top and bottom, respectively. Original images are from [16] and [49]; they have been annotated for clarity.

(CCDs): Juno Color Camera (JunoCam), the Advanced Stellar Compass (ASC), and the Stellar Reference Unit (SRU). Juno also has an Ultraviolet Spectrometer (UVS) that has a micro-channel (or multi-channel) plate (MCP) detector. Each of these instruments presents an opportunity to extract environment information and there are ongoing attempts to do this (see Section 2.4.1).

Europa Clipper, currently in Phase B of design, is a NASA spacecraft designed to assess the habitability of Jupiter's icy moon, Europa. Europa Clipper will orbit Jupiter rather than Europa directly to avoid the high-radiation environment close to Jupiter (see Figure 1-8(b)). On closest approach, Europa Clipper will come within 25 to 100 km of the surface of Europa. There are about 45 flybys of Europa planned for the 3.5-year mission. The main lifetime limiting factor is high-energy radiation [91].

At the time of writing, there are no instruments on Europa Clipper dedicated to MeV particle detection. There has been a proposed Radiation Monitoring System (RMS) that would include a charge monitor and dosimeters for TID, but its capability of providing electron spectrum measurement is being defined. There are instruments that are sensitive to MeV radiation: the Ultraviolet Spectrograph (UVS), Mapping Imager Spectrometer for Europa (MISE), Europa Imaging System (EIS), and MAss SPectrometer for Planetary EXploration (MASPEX). Europa Clipper will also have star scanners. Since these instruments are sensitive to MeV radiation, they could yield information about the high-energy radiation environment.

In summary, to gain a better understanding of the Jovian radiation environment, from both a science and engineering perspective, we need more data: greater orbit diversity of measurements (spatial and temporal coverage and energy range), more exposure time, and a larger area for evaluation (pixels, detector area). Juno and Europa Clipper have orbits that, if higher energy (>1 MeV) particle measurements were taken, would significantly improve the spatial and temporal knowledge of the Jovian magnetosphere.

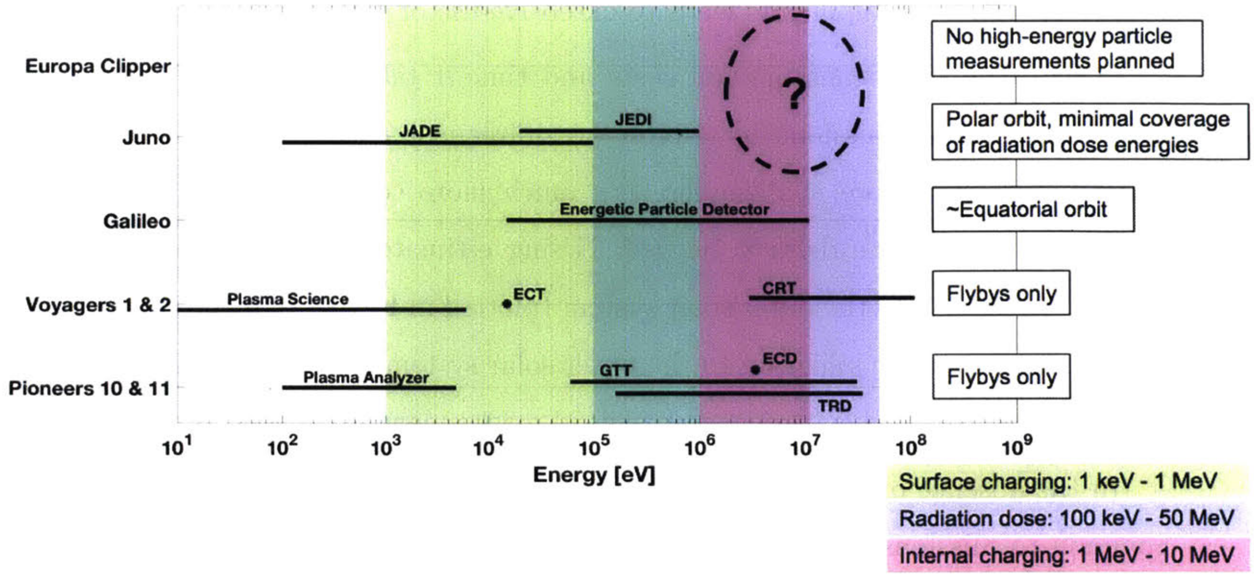

Figure 1-9: Energy ranges covered by instruments on spacecraft to Jupiter. The shaded regions correspond to the energy ranges of concern for specific radiation effects: the radiation dose and dose rate risks in blue, internal charging and internal electrostatic discharge (IESD) risks in pink, and surface charge risk in green. Pioneers and Voyagers made high-energy electron measurements in the zones of concern, but those missions were only flybys, resulting in limited temporal and spatial measurements. Galileo EPD made measurements over a period of 35 orbits, mainly equatorially around Jupiter. Juno orbits over the polar region of Jupiter, but has limited high-energy detection capabilities. For the Europa Clipper mission, currently in development, there are no dedicated high-energy particle measurements planned.

1.4 Motivation for Developing a Technique Using Science Imagers

Energetic particle detectors are not always included on spacecraft due to resource constraints (e.g., cost, complexity, schedule). From a sampling of energetic particle detectors designed for Earth orbit, Jupiter orbit, and interplanetary medium, we find commonality in design due to similar engineering constraints and scientific goals. We find that the average mass is in the 10's of kilograms, the average power needs are in 10's of Watts, and the sizes range significantly (depending on the types and energies of particles for detection) from about 10 to 40 cm in each dimension [59]. The amount of electronics can be significant as well, and the need for low-power, densely packed, radiation-tolerant components leads to extensive use of custom integrated circuitry.

Due to the significant mission costs and time it takes to reach the outer solar system, spacecraft missions to Jupiter are infrequent (see Sec. 1.3). In addition, orbiters are even more challenging: it's much more costly to orbit than to do a fly-by in terms of the delta-V needed. Using estimates of mission costs and wet masses of missions to the outer solar system (plotted in Figure 1-10), we find that the approximate cost per kilogram to the outer solar system is ~\$500,000/kg in FY2000 dollars. In contrast, the average cost to send mass to low Earth orbit is ~\$20,000/kg.

In the absence of energetic particle detectors, we explore how existing hardware, common to missions to the outer solar system, can be used as sensors of the high-energy electron environment. We focus our study on scientific imaging instruments ("imagers") for two reasons: (1) scientific imagers are common to exploration spacecraft, such as those designed for Jupiter and other exploratory missions, and (2) radiation effects are a well-observed and studied phenomena in imagers [30, 57]. We focus on solid-state devices, using semi-conducting detecting materials, where the

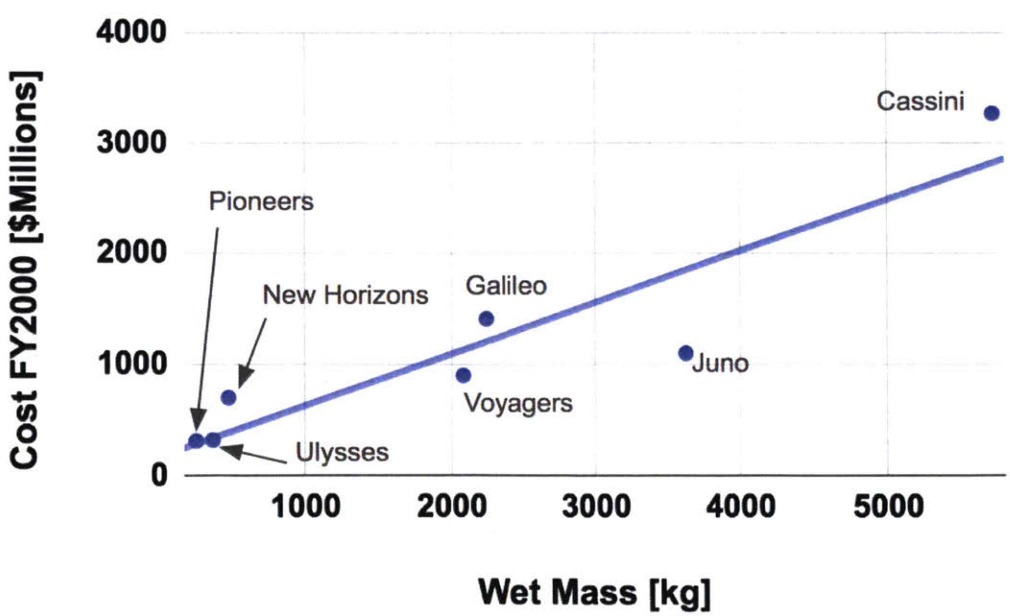

Figure 1-10: Approximate launch cost in FY2000 dollars per kilogram for missions to the outer solar system. The best fit line has a slope of ~\$500,000/kg in FY2000 dollars.

sensitivity to radiation manifests as noise [57]. There are well-documented (though limited) techniques for extracting radiation "hits" for proton noise, which we build upon to develop a novel method to identify electron noise. These techniques are discussed in Chapters 2 and 3.

This technique could be used in other environments (e.g., Earth orbit, or interplanetary) and could use other types of imagers (e.g., star cameras). For example, for an astrophysical observatory with sensitive detectors, such as the Transiting Exoplanet Surveyor Satellite, the final orbit may be relatively benign with regards to radiation, but the spacecraft must still traverse the Earth's radiation belts, providing the possibility of additional radiation measurements. We discuss other applications in Chapter 7.

1.5 Thesis Contributions

The goal of this thesis is to extract quantitative information about the high-energy (>1 MeV) electron environment at Jupiter using existing technologies on-board spacecraft. We propose using science imagers, which are sensitive to MeV electrons that are recorded as noise on the detector and detailed simulations of the instrument's response to high-energy electrons to determine the energy and flux of electrons in the environment.

We develop the technique using data from the Galileo spacecraft, which provides an excellent opportunity for analysis, since there are both imaging instruments and an energetic particle detector that can be used for validation. We use the Galileo Solid-State Imaging instrument, which is an 800 x 800 pixel CCD, to demonstrate the method. We identify and extract the electron radiation noise in the flight data and compare the noise to charged particle transport simulations in Geant4, a charged particle transport code [2], to determine the energy sensitivity of the instrument. We compute the integral flux and the results are then compared to the Galileo EPD for validation. We demonstrate that the technique is useful for a general imager by applying the method to another imager: the Galileo Near-Infrared Mapping Spectrometer (NIMS), which is a focal plane array spectrograph with seventeen individual photovoltaic diodes, also showing agreement with the EPD.

In summary, this thesis makes the following contributions:

1. Develops an approach for combining simulations using detailed mechanical and materials models of imaging cameras along with experimental image analyses to obtain particle energy measurements.
2. Creates a process for extracting electron radiation hits in an imager.
3. Demonstrates and validates a generalized procedure for calculating the environment integral flux from an imager.
4. Establishes guidelines for pre-flight testing and calibration, as well as in-flight operational procedures to use an imaging instrument for energetic particle measurements, including specific recommendations for the Juno and Europa Clipper missions.

1.6 Thesis Organization

In Chapter 1, we discussed the space radiation environment, focusing on the Jovian energetic electrons. We described the models that are used, the particle measurements and physics the models are derived from, and the effects of radiation on spacecraft. We discussed the need for in-situ particle flux and energy information, but illustrated the challenges with including dedicated energetic particle measurements. In Chapter 2, we summarize how imagers work and explain how high-energy charged particles affect imagers. We discuss previous work using imagers to detect radiation, reviewing the relevant literature. Chapter 3 describes the technique developed for calculating a flux measurement from an image, using detailed models of an imager and extracting radiation from a raw image. In Chapters 4 and 5, we analyze the Galileo SSI and Galileo NIMS instruments, respectively. We simulate high-energy particle transport in models of the instruments and extract high-energy radiation signatures from the raw images. We compare the computed fluxes to the Galileo EPD. We discuss the sensitivity of the technique to noise and other factors in Chapter 6 and compare the results to GIRE2. Chapter 7 describes how the technique can be applied to other missions and different environments and directions for future work.

Chapter 2

Literature Review

In this chapter, we will explain how imagers are sensitive to high-energy electrons and provide context for this work by reviewing previous efforts using imagers to detect radiation.

2.1 Solid-State Detectors

A solid-state detector (or a semiconductor-based device) is a photosensitive device that converts incoming photons into electric charge. The detecting medium is a semiconductor material such as a silicon or germanium crystal. Solid-state detectors include three main types of devices in space-based imaging: charge-coupled devices (CCDs), complementary metal-oxide-semiconductors (CMOSs), and infrared focal plane arrays. The imagers can be any shape, with hundreds to millions of imaging elements ("pixels"). Charge generation takes place at the semiconductor body of the device in two ways: (1) by the photoelectric effect, where photons create free electrons by promoting electrons into the conduction band, and (2) by ionizing energy loss, where an energetic charged particle creates an electron-hole (e-h) pair. The generated electric current is converted to a digital signal when the device is read out [57]. Section 2.2 explains more thoroughly the effects of energetic electrons.

The CCD is one of the most common types of solid-state imagers due to its low noise operation, high resolution, precise image geometry, and stability [18, 57]. CCDs

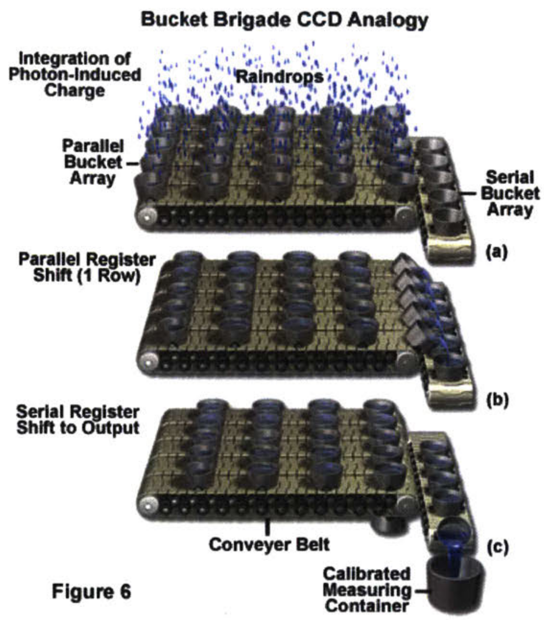

Figure 2-1: CCD operation and readout are analogous to a rain bucket brigade. Photons are collected like rain into individual pixels like buckets. Each pixel converts the photons into electrons. The pixels are read out line by line, like shifting the buckets and collecting the rain. Image source: [31].

typically consist of a matrix of potential wells, or pixels. Free electrons generated within the silicon lattice by the passage of charged particles, such as those found in the space environment, are stored in the individual pixels. Then, the charge pattern must be transferred out of the CCD, which is done in a controlled manner by modulating the gate potential across the CCD gates (thin conducting strips). The time reference to which the potential changes are synchronized is called a clock cycle. The end pixel or line of pixels is transferred to a special pixel array, called the serial register. The result is a sequence of charge packets emerging from the serial register, each of which is directly proportional to the photon(s) striking the particular location on the CCD. The final step is to convert the emerging charges into electric signals with preamplifiers on the chip. A commonly used analogy for the CCD serial readout is the rain bucket analogy, where each bucket (pixel) collects rain (photons, which are converted to electrons in the bucket), and an entire row is shifted in parallel into a series of reservoirs on a perpendicularly oriented conveyor. The accumulated rain in each bucket is measured in series by pouring the container into a calibrated container (an analog to digital converter). See Figure 2-1. For more information on general CCD operation, the reader is referred to Janesick (2001) and Ch. 46 of Webster and Eran (2014) [57, 115]. Figure 4-3 shows a diagram of the Galileo SSI CCD, which is an 800 x 800 pixel virtual phase CCD. A virtual phase CCD is an extension of the two phase CCD and is unique in that it requires only a single level of gate metalization to control CCD charge collection and transfer [58].

For a CMOS detector, each pixel has its own charge-to-voltage conversion electronics, enabling readout for each pixel. The increased electronics lead to less area for photon collection and increased complexity, leading to additional noise. However, CMOS technology is typically less expensive due to the manufacturing process and consumes less power compared to CCDs.

2.2 Charge Generation in Solid-State Detectors

A charged particle passing through semiconductor material, such as silicon, creates electron-hole (e-h) pairs by breaking a covalent bond in the silicon lattice. In a low energy state, the silicon crystal structure consists of atoms tetrahedrally bonded by sharing valence electrons (covalent bonding). A charged particle can break bonds creating "free" electrons and corresponding "free" holes. The electrons and holes are "carriers," or mobile charged particles. The total charge generated is proportional to the energy lost by the charged particle, $Q \propto \Delta E$. A charged particle must have enough energy to jump from the valence band to the conduction band. The band gap is dependent on the material, doping, and device configuration. For silicon, the band gap is $E_g = 1.12$ electron volts (eV).

Energetic electrons lose kinetic energy in matter in two ways: (1) through inelastic collisions with orbital electrons in the semiconductor, exciting and ionizing atoms along their trajectory, and (2) at higher energies, through bremsstrahlung radiation, which occurs when the particle is deflected or slowed down in the electric field of a nucleus[1], emitting radiation [57, 108]. It is also possible that the electrons elastically

[1] And, to a lesser extent, in the electric field of an atomic electron.

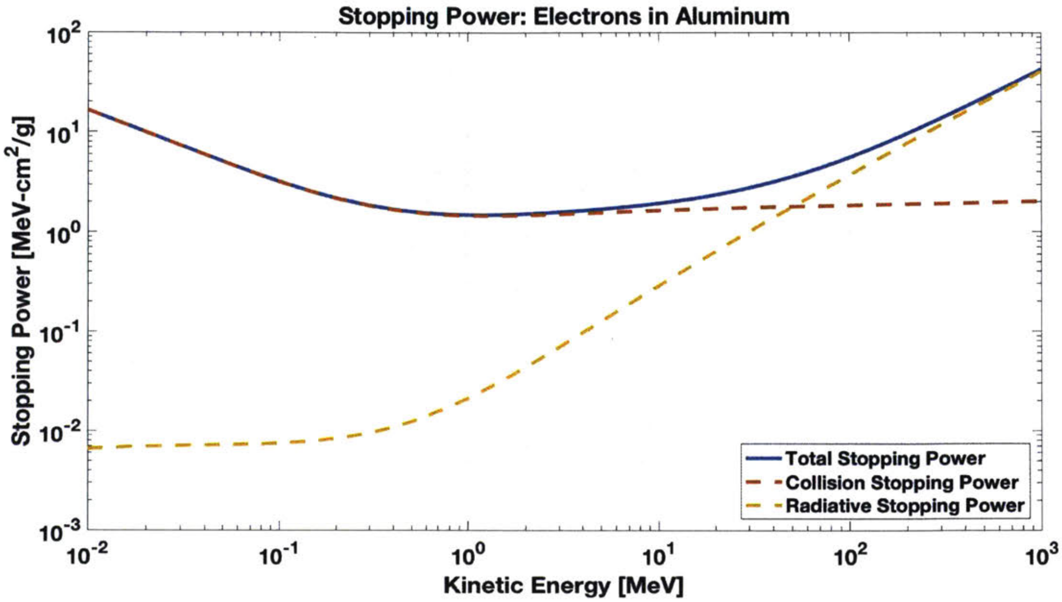

Figure 2-2: Stopping power of electrons in Aluminum with contributions from collisional and radiative losses. Data source: [86].

scatter from nuclear and electronic interactions or through nuclear excitation, but these processes are usually negligible and applicable at lower energies [108]. The stopping power $\frac{\mathrm{d}E}{\mathrm{d}x}$ for a material is a measure of the retarding force on the particle in matter. For electrons, the total stopping power is:

$$\left(-\frac{\mathrm{d}E}{\mathrm{d}x}\right)_{\text{total}} = \left(-\frac{\mathrm{d}E}{\mathrm{d}x}\right)_{\text{collisional}} + \left(-\frac{\mathrm{d}E}{\mathrm{d}x}\right)_{\text{radiative}} \tag{2.1}$$

The relative importance of each contribution depends on the material (atomic number, Z) and the energy (E) of the particle.[2] The two rates of energy loss are approximately equal when

$$1 = \frac{(\mathrm{d}E/\mathrm{d}x)_{\text{radiative}}}{(\mathrm{d}E/\mathrm{d}x)_{\text{collisional}}} \approx \frac{ZE}{800} \tag{2.2}$$

So, for Aluminum ($Z = 13$), the collisional and radiative losses are equal at approximately 60 MeV. A plot of the stopping power for electrons in Aluminum with the contributions from collisional and radiative losses is given in Figure 2-2.

The energy loss of a particle in a shielding medium is a function of the distance

[2]Collisional stopping power is proportional to Z and increases logarithmically with energy. Radiative stopping power is proportional to Z^2 and increases linearly with energy.

traveled and the type and initial energy of the particle. The atomic electrons either experience a transition to an excited state or to an unbound state into the conduction band (i.e., ionization). Nearly all energy loss (99.9%) is converted to electron-hole (e-h) pairs, called "ionizing energy loss" (IEL). The remaining energy is given to nonionizing interactions, including displacing silicon atoms, called "nonionizing energy loss" (NIEL). During IEL, conduction band electrons are collected in the nearest potential well, generating a transient event in an image [30, 57, 75]. Charged particles leave a electron-hole track producing approximately one electron-hole pair for every 3.65 eV of energy absorbed in silicon [57, 76]. The ionizing trail of charge left behind is not a permanent feature and can be erased simply by reading the CCD. This charge deposition by an energetic particle is what this thesis aims to extract from the flight data. More information on the space radiation impacts on imagers can be found in [57, 105, 118].

2.3 Radiation Identification in Science Images

The majority of the literature on space radiation detection with imagers is with reference to identifying and removing *proton* and *cosmic ray* radiation effects. Since the radiation is seen as a nuisance rather than data, anything resembling radiation (which could include other noise sources) is removed aggressively. Anderson and Bedin (2010) and Prod'homme et al. (2012) look at proton damage identification and charge transfer efficiency corrections for Hubble Space Telescope CCDs and Gaia CCDs, respectively [3, 92]. Cresitello-Dittmar, Aldcroft, and Morris (2001) identify warm pixels from the Chandra X-ray Observatory's star camera CCDs. The typical process is to identify radiation and then remove its contribution from the image signal that one is trying to measure. Techniques for identifying and removing radiation include outlier detection, where pixels that are a certain standard deviation above the surrounding pixels are identified and removed, and boxcar averaging in which pixels with more than a few standard deviations above the mean of the box (e.g., a 5 by 5 pixel box) are replaced with the average of the box [105]. The only literature on identifying or removing *electron* radiation noise from imagers in space is from a handful of works on Galileo, New Horizons, and Juno. These analyses will be discussed in detail in Section 2.4.1.

2.4 Imagers as Radiation Sensors

There have been a few instances in the literature where effects on an imager have been identified for the purposes of making measurements of the radiation environment.

Earth-based radiation detection. Earth-based imagers have been proposed as sensors for radiation detection [18]. For high-energy alphas (α) and protons, Li et al. and Burke et al. (1997) proposed the use of back-illuminated and front-illuminated CCDs, respectively, for charged-particle spectroscopy. They irradiated a large-area front-illuminated imager with α particles with energies up to 5.5 MeV and protons up to 13 MeV. These studies were for diagnostics of inertial confinement fusion implosions. They compared the tests to calculations and found agreement, concluding that CCDs could be used for proton and alpha particle spectroscopy [20, 56, 79]. Most recently, Archambault et al. (2008) characterized radiation-induced noise in CCDs that are now being used more frequently for medical radiation therapy, comparing four radiation filtration techniques [4].

Space-based radiation detection. In Grant et al. (2010, 2012) and Ford and Grant (2012), the Chandra X-ray Observatory advanced CCD imaging spectrometer (ACIS) team developed a technique to use the CCDs as radiation monitors. The Electron, Proton, Helium Instrument (EPHIN) is a particle detector on Chandra to monitor the local high-energy particle environment. Elevated temperatures on board have limited EPHIN's effectiveness as a radiation monitor; the signal is dominated by thermal noise. Given the degradation of EPHIN, the ACIS CCDs are used to measure the environment. The charge transfer inefficiency (CTI) for two of the CCDs (one backside-illuminated and one frontside-illuminated) is measured over time [42, 51, 50]. Grant et al. (2010, 2012) use ACIS CTI measurements from early in the mission and compare them to the EPHIN data. The algorithm detects CTI threshold crossings and shows good agreement with the EPHIN. This technique is the current state of the art for actively measuring proton radiation using active imaging CCDs.

Shen and Qin (2016) (and references therein) present cosmic ray estimates using spikes in raw solar images from the CCDs on the Solar and Heliophysics Observatory (SOHO) Extreme ultraviolet Imaging Telescope (EIT). They computed count rates and find agreement with the Geostationary Operational Environmental Satellite (GOES) 11 P6 channel (80-165 MeV) [101]. They employ a median filtering algorithm, which had been shown previously to be effective at identifying cosmic rays [35, 41].

2.4.1 Imagers as Electron Radiation Sensors

Literature on identifying noise in imagers due to electrons can be found from missions in (or flying by) the Jovian environment. In the New Horizons mission, which had an eleven day Jupiter dusk flyby in 2007, Steffl et al. (2012) examine the MeV electrons detected in the background noise of the Alice ultraviolet imaging spectrograph [106]. The imaging instrument is a microchannel plate detector with aluminum housing that is only 1.3 mm (50 mils) thick. The radiation environment at Pluto and the Kuiper belt did not require more shielding, as is needed for a Jupiter orbiter [107]. They find that the electron count rate is nearly linear with the expected flux. Using MultiLAyered Shielding SImulation Software (MULASSIS), they find that the imager is sensitive to $\sim$1-8 MeV electrons, which is consistent with the Aluminum shielding. Steffl et al. qualitatively compare the count rates to the measurements from the Pluto Energetic Particle Spectrometer Science Investigation (PEPSSI), which is only sensitive to $<$1 MeV electrons. While only measuring count rates, using the Alice UV imager proved valuable scientifically: in the days following closest approach, the spacecraft was able to combine the electron count rates with the PEPSII measurements to better understand the 35-90 R_J region downstream of Jupiter. The measurements of the Jovian magnetosphere as the spacecraft passed through contributed to significant updates to the magnetopause models, finding that the current sheet crossings all occurred northward of the model predictions, implying a stronger solar wind dependency than originally suggested.

For the Galileo spacecraft, Klaasen et al. (1997) select eight SSI images from the ninth orbit (C9) of Jupiter and calculate the measured radiation counts [electrons/sec] and the CCD charge [electrons] compared to the predicted rates from pre-flight testing [72]. At the time of the study, the Galileo Energetic Particle Detector (EPD) team was able to confirm that the SSI charge rate agreed qualitatively with the EPD (EPD final data products were unavailable at the time of Klaasen et al.'s 1997 paper). In further SSI calibration papers, Klaasen et al. (1999, 2003) go into a bit more detail to extract and examine electron radiation [73, 74]. Their method for computing the radiation noise was to select the first few lines of the image, average the DN, and subtract it from the remaining background. The background was selected by eye in rectangular patches. Figure 2-3 shows the radiation-induced count rates on the SSI as a function of distance from Jupiter. While good for a first order analysis, this is not a robust way to detect radiation in an image, since there is likely a radiation contribution in the first lines of the image. In addition, their assumption is that the non-radiation background sources are constant over the image regions so that the time dependence of DN/pixel is due only to radiation.

Fieseler (2000) examined the use of the Galileo star scanner, which is a photomultiplier tube, as an energetic electron detector. Fieseler used NOVICE, a charged particle transport code [64], to determine that the star scanner is sensitive to electron energies between 1-15 MeV. However, he did not compute scale factors relating the count rates observed to environmental fluxes. He compared his count rates to the EPD and found agreement with the >11 MeV electron channel [39]. Garrett et al. argue that Galileo's star scanner could have been used as a proper monitor of >20 MeV electrons, which Feiseler suggested [40, 39], if the star scanner had been calibrated pre-flight. The absence of a dosimeter and the lack of continuous EPD measurements during the Galileo mission have made it difficult to determine the overall mission dose.

In Carlson and Hand (2015), radiation hits were extracted from the Galileo Near-

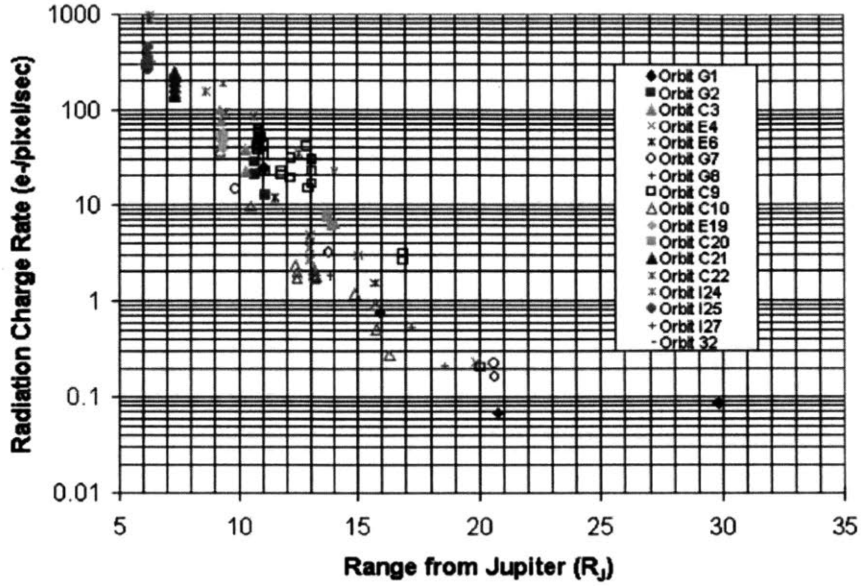

Figure 2-3: Computed electron radiation-induced count rates in Galileo SSI images as a function of distance from Jupiter. Image source: [74].

Infrared Mapping Spectrometer (NIMS) data from 9-11 R_J and the hits were compared to particle transport simulations. The full instrument was not modeled; slabs of representative tantalum were used for shielding in the model. The authors varied the amount of shielding and compared the simulation results to the transient event rates. The authors claim that the results are consistent with those expected at Europa orbit (9.4 R_J) [22]. However, they do not conclude anything about the energy or magnitude of that flux.

The closest literature to the methods developed in this thesis are from Becker et al. (2017a, 2017b). Becker et al. (2017a) examines electron radiation effects on three instruments on the Juno spacecraft: the stellar reference unit (SRU), advanced stellar compass (ASC), and Jupiter infrared auroral mapper (JIRAM) infrared imager[3] [11]. Using Geant4 for penetration analysis, they infer that the JIRAM imager is sensitive to >5 MeV electrons and the SRU and ASC instruments are sensitive to >10 MeV electrons. They compute the omnidirectional fluxes during the first and third perijoves, though a description of the factors converting the count rates to fluxes is not provided [12]. There is no energetic particle detector for comparison to or validation

[3]More information on JIRAM can be found: [1].

of their results.[4] For identifying radiation, they employ two methods depending on the count rate. The first method looks at clusters of pixels in a 7 x 7 pixel region and looks for local maxima in the regions or pixels that are above a detection threshold (>48 DN) compared to all the neighboring pixels. This is similar to the techniques mentioned previously for proton radiation detection. For JIRAM, they use a "DN processing" technique that calculates the total count rate based on the exposure time as a percentage of pixels above a threshold. While Becker et al. provide limited detail on their methodology and technique validation, their analysis demonstrates that imagers on Juno are being actively used to provide information about the near-Jupiter electron environment.

In summary, radiation detection is typically limited to high-energy spectrometers, and radiation hits are dealt with in CCDs as an annoyance that needs to be removed. In some cases, hit rates are computed, such as for the SSI and NIMS [72, 22], but they are not used to infer anything about the space environment. For the Chandra CCDs, radiation information is extracted, but energies and fluxes are not part of the technique in the algorithm. This thesis aims to extract the noise in solid-state devices and use the noise as a measurement of the high-energy radiation environment, including detail of the environment characteristics (energy spectra, particle species, flux).

[4]Becker et al. (2017a, 2017b) claim they have performed in-flight calibration by comparing measurements of Earth's proton belts to within ~25%. We contend that methods for protons around Earth cannot validate methods for electrons around Jupiter.

Chapter 3

Approach

Figure 3-1 shows a high-level block diagram of the technique developed in this thesis to extract high-energy electron information from an imager. In this chapter, descriptions are in terms of a general imager. The imager-specific details for SSI and NIMS can be found in Chapters 4 and 5, respectively.

In Section 3.2, referring to the simulations described in the left side (blue box) of Figure 3-1, we use detailed drawings to create a full mechanical model (geometry and materials) of the instrument. We use a particle transport code (Geant4) to model the passage of electrons through the instrument to the detector. The number of pixels with radiation energy deposited are used to relate measurements to the simulation environment. We determine the minimum energy that the imager is sensitive to and the integral flux at that energy in the environment.

In Section 3.3, referring to the image processing (right side, yellow box) in Figure 3-1, we collect the raw imager data, process the data to remove non-radiation contributions, and determine the energy deposited in the image. Combining this information with that from the simulation, we compute the integral flux for the individual image. We repeat the image processing to collect flux measurements from more images. The final step is to compare the calculated fluxes to the energetic particle measurements from the Galileo Energetic Particle Detector (EPD).

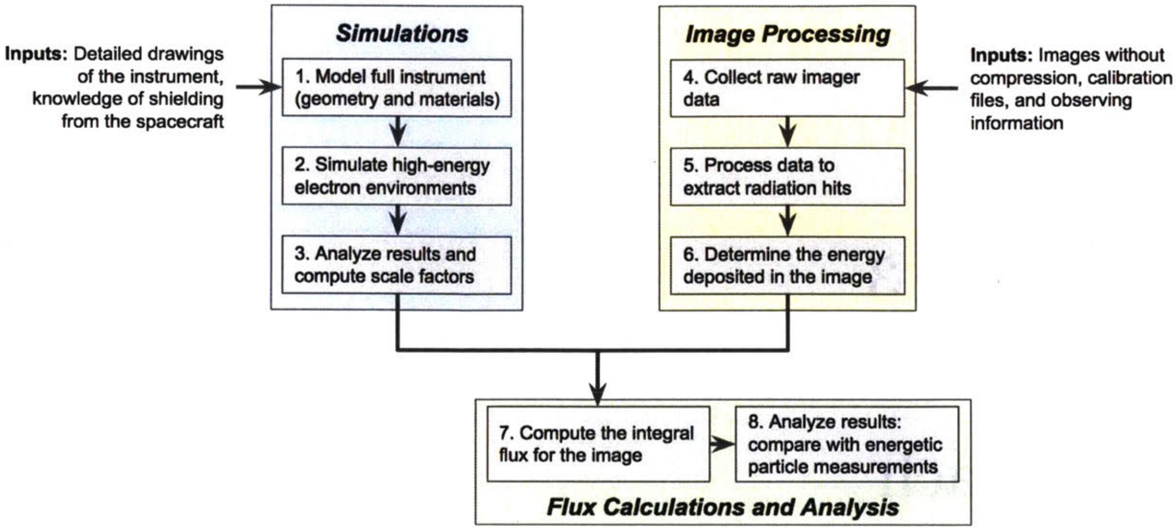

Figure 3-1: High-level block diagram of the modeling and image processing techniques developed in this thesis to infer measurements of the energetic particle environment from scientific imagers.

3.1 Overview of the Galileo Mission

Launched in October 1989, the Galileo spacecraft was a NASA mission that studied Jupiter and Jupiter's moons. The spacecraft arrived in December 1995 and continued to perform observations through September 2003, completing 34 orbits. Galileo consisted of both an orbiter and a probe, becoming the first man-made objects to orbit Jupiter and to descend into Jupiter's atmosphere, respectively. There was a spinning section of the spacecraft for gyroscopic stability, rotating at three rotations per minute, which contained four of the six science instruments. Figure 3-2 is a diagram of the Galileo spacecraft; the SSI and NIMS are located on the scan mirror platform.

The Galileo orbital periods were roughly two months each, in elongated ovals around the equatorial region of Jupiter, designed for close fly-bys of Jupiter's largest moons. Each orbit was numbered and named for the moon that the spacecraft encountered at closest range. For example, orbit "C3" was the third orbit of Galileo around Jupiter, with a closest approach to the moon, Callisto.[1] Figure 1-7 shows a polar view of the Galileo EPD measurements in a sun-oriented reference frame.

[1] C: Callisto, G: Ganymede, E: Europa, I:Io, J: Jupiter (no close moon encountered), A: Amalthea

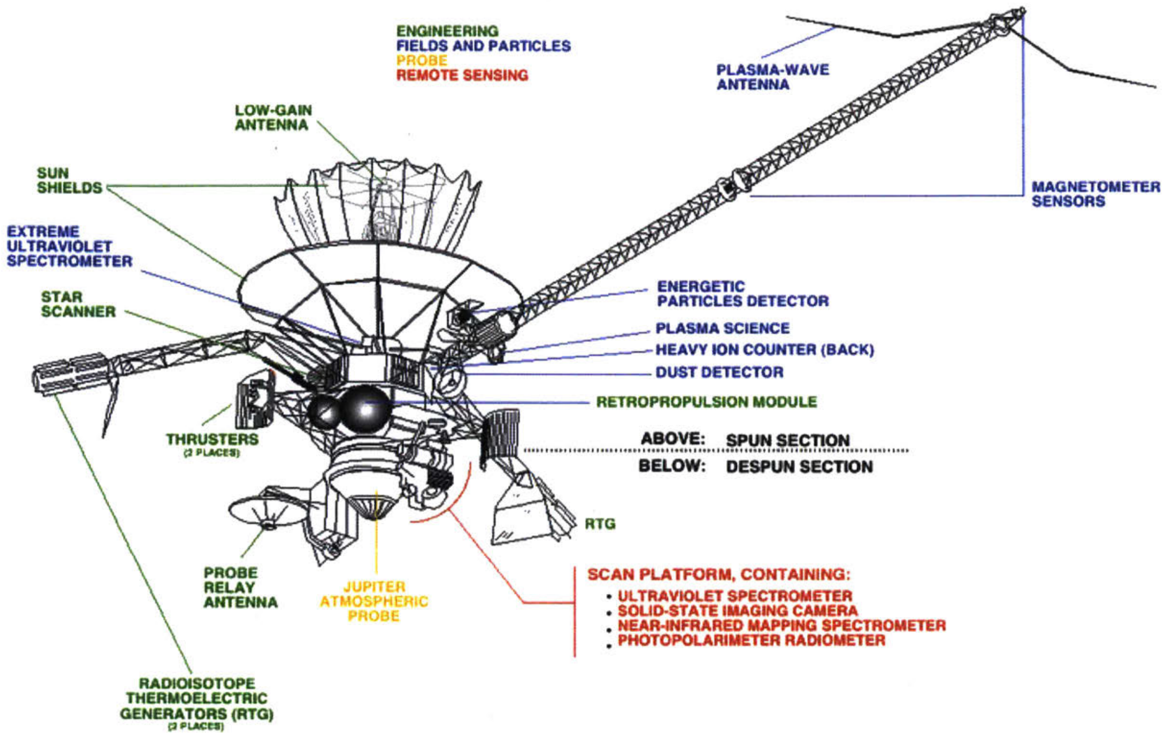

Figure 3-2: Diagram of the Galileo spacecraft with the main components and instruments labeled. The SSI and NIMS are part of the scan platform, to the bottom right of the drawing, labeled in red. The EPD is to the top right of the drawing, labeled in blue. Image source: NASA, 1989, `https://solarsystem.nasa.gov/galleries/galileo-diagram-labeled`.

Additional general information on the Galileo spacecraft can be found on its legacy site: `https://solarsystem.nasa.gov/missions/galileo/in-depth/`.

The radiation environment and its anticipated effects played a significant role in the design and operation of the spacecraft, and there were several anomalies attributed directly to radiation [40]. The spacecraft's gyroscopes often exhibited increased errors. Electrical arcing occurred several times between the rotating and non-rotating parts of the spacecraft, causing it to enter safe mode, which led to total loss of the data from the 16th, 18th and 33rd orbits. Radiation also caused phase shifts in Galileo's ultra-stable quartz oscillator. This thesis focuses on the radiation-induced noise in the imaging instruments.

Of relevance to this work, the Galileo high-gain antenna did not deploy completely

[60]. This failure led to drastically lower data return capabilities than originally anticipated. As a result, a majority of the images were compressed with loss of information, rendering them unusable for this analysis.

3.2 High-Energy Electron Transport Simulations

3.2.1 Modeling the Instrument

In order to simulate how electrons can reach the detector and deposit energy, we must have an accurate model of the instrument. This includes the physical geometry and materials of each of the elements. In addition, we model shielding from the spacecraft and other instruments around the imager to have a more accurate representation of how radiation would be blocked and subsequently enter the detector(s).

In this work, we model the SSI and NIMS in SolidWorks to produce a 3D CAD model, which we export as a STEP file. These CAD models previously did not exist for the Galileo SSI and NIMS instruments and had to be developed through a process of deciphering blueprints of the instruments and talking with the original designers and operators of the instruments. For modern instruments, the CAD model is generally available, eliminating a significant portion of the work preparing for the simulations.

3.2.2 Particle Simulation Description

We simulate electrons from the environment impacting the imager using a particle transport code called Geant4, version 10.01 [2]. Developed by CERN, Geant4 uses Monte Carlo methods: it does not solve explicit transport equations but obtains results by simulating individual particles and recording their average behavior (results are statistical). Particles are tracked from the source environment to the target (the detector, in this case). Geant4 is capable of modeling all particles relevant to the space environment: electrons, photons, protons, neutrons, and heavy ions. While Geant4 can be slow (it can take days to run a one billion electron simulation of a

Table 3.1: Simulation parameters used in Geant4 particle simulations.

Parameter	Value
Source environment	sphere radiating inwards
Source angular distribution	cosine-law
Radius of source sphere	150 cm
Number of source particles	1×10^9 e-
Number of runs	5
Energies simulated	1, 3, 5, 10, 30, 50, 100, and 200 MeV

detailed instrument), it offers benefits over other codes in that it can handle complex geometries, has extensive high-energy physics, and is capable of modeling secondary and tertiary particle transport.[2]

For the simulation environment, we place the instrument in a vacuum. We define a sphere encompassing the instrument and the representative spacecraft shielding. For the SSI and NIMS, this is a 150 cm radius sphere (large enough to envelop the entire instrument) with the instrument at the center.

In order to simulate an isotropic space environment, we select a cosine-law as a source angular distribution because the uniform, isotropic distribution on a surface produces a cosine distribution, which is defined as a distribution that the equal number of particles is coming in per unit "solid angle" [81]. In other words, the projected area seen by the impinging isotropic source particles will vary with the $\cos(\theta)$ dependency, θ being the angle from normal incidence. Also, we only simulate the incoming particles from a spherical source surface. As a result, the simulated flux is four times larger than the real environment. There is a factor of two due to the integration of the cosine of the angle of incidence with respect to the normal plane. There is an additional factor of two due to over-sampling because we are only simulating the inwards particles while the particles will be incoming and outgoing from the source surface in the real environment. This factor of four is accounted for in the flux calculation and is explained in a mathematical formulation in Appendix A.

[2]For an overview of other particle transport codes for space applications, see Jun et al., 2008 [66].

```
# Macro for mono-energetic runs
/gps/particle e-
/gps/energy 200 MeV
/gps/pos/type Surface
/gps/pos/shape Sphere
/gps/pos/centre 0. 0. 0. cm
/gps/pos/radius 150. cm
/gps/ang/type cos
/tracking/verbose 0

/random/setSeeds 01 02
/run/beamOn 1000000000
```

Figure 3-3: Example macro file for a Geant4 simulation.

We simulate one billion mono-energetic electrons per run for five runs (to build up statistics). The maximum number of particles that Geant4 can simulate is 2^{32-1}, which is roughly two billion particles. We simulate one billion particles for each run for simplicity. We simulate electron energies between 1 MeV and 200 MeV. The simulation parameters are summarized in Table 3.1. The physics list used is included in Appendix B. Figure 3-3 shows a simple example of a macro file for Geant4 that defines these parameters.

The output from Geant4 can be specified in one of the source files. For electrons that make it to the detector, we have the code report the original particle location, angle, and energy, the final particle location on the detector, the amount of energy it deposited, the length of its path, the physics process governing the interaction, and information about whether the particle is the primary electron or a secondary (or higher-order) particle.

3.2.3 Processing the Simulation Results

We read in and process the results using code written in MATLAB. We save information on the particle tracks that have deposited energy in the detector(s). For an array of pixels (like the SSI), we sum the energy deposited in each pixel and record the number of particles generating that total energy. For a multi-detector imager (like NIMS), we sum the energy deposited for each detector, where there is only one "pixel" per detector, and record the number of particles. We also calculate statistics on the number of primary and higher order particles that reach the detector, the

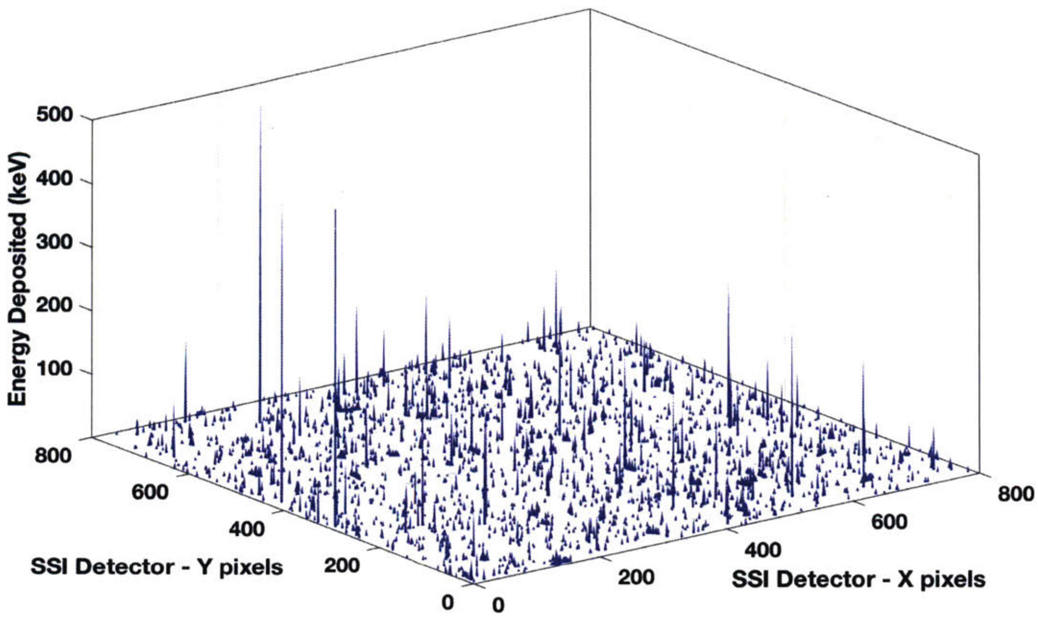

Figure 3-4: Example of the processed results from a simulation of one billion 100 MeV electrons impacting the Galileo SSI. The z-axis shows the total energy deposited in each pixel.

number of those that deposit energy, and the steps and tracks the particles took to reach the detector. Figure 3-4 shows an example of the processed Geant4 results of the simulated 800 by 800 pixel SSI detector, with the intensity scale representing the total summed energy deposited in each pixel.

Summarizing the inputs needed. For the simulations, we require:

- Detailed model of the instrument components and detector (geometry and materials)
- Rough model of the spacecraft and surrounding instruments (geometry, materials, and location relative to the instrument being analyzed)
- Access to and knowledge of a particle transport code, such as Geant4

3.3 Image Processing

3.3.1 Data Collection

To process the imager data, one must collect the raw image data, any image observational mode information, and relevant processing and calibration files (dark current measurements, blemish files, shutter offset files, etc.). For the raw image, we need the original data (or digital) number (DN) for each pixel (or detector). Raw images cannot have undergone lossy compression or on-board processing that includes radiation extraction. For each of the images, one must understand the observational modes (gain modes, frame rates, etc.) and how the instrument operates, such as how readout and shutter processes are carried out.

For both the SSI and NIMS, raw images and observational information are collected from the Planetary Data System (PDS), which can be accessed freely at: `https://pds-imaging.nasa.gov/`. Provided and supported by NASA, the PDS is a long-term archive of digital data products returned from NASA's planetary missions. The data from the PDS are in a standard format, details on which can be found through the PDS website and the PDS Standards Reference.[3]

3.3.2 Radiation Extraction

We process the flight data by subtracting the dark current and eliminating known detector blemishes. We remove anything else that should not be attributed to radiation, such as the observation target, like a moon or planet. Then, for imagers with pixel arrays, such as the SSI, we examine the DN of the pixels relative to the background. We have developed a technique for identifying the radiation hit pixels from other pixels. The SSI and NIMS radiation extraction details can be found in Chapters 4 and 5, respectively.

Once the radiation hits have been identified, we apply the calibrated instrument gain to convert the DN to electrons. Given the detector material, we convert electrons

[3] `https://pds.nasa.gov/datastandards/documents/sr/current/StdRef_1.10.0.pdf`

to the energy deposited in that pixel (or detector). For silicon and indium antimonide, for example, the ionization energy needed to create an electron-hole pair is 3.6 eV and 1.1 eV, respectively [76] (i.e., the delta-Energy for an electron to move from the valence band to the conduction band). The processed image is a matrix of energy deposited in each pixel for an array, which can then be binned to form a histogram of energy deposited by the number of pixels.

Summarizing the inputs needed. For the image processing, we require:

- Raw images that have not undergone lossy compression
- Gain factors relating the digital number (DN) to electrons
- Information on dark current and other calibration factors
- Detector readout information (line by line, frame modes)

3.4 Differential Particle Flux and Count Rate

A particle environment is often defined by the differential, directional, particle flux, $J(E, \theta)$, which is defined at a given location, direction (orientation) the particle is coming from, θ, and energy, E. The differential particle flux is the number of particles at an energy, E, within a given energy range dE, which cross a unit area, dA, perpendicular to the specified look direction, Ω, within a solid angle, $d\Omega$, in one second [10]. The units of the differential, directional flux are: #/cm^2-s-sr-MeV. We consider particles coming from all space, so the angular dependence is known. For an isotropic distribution, such as that found in the space environment, the differential directional flux is integrated over the solid angle and is called the *omnidirectional* differential flux. Figure 3-5 shows a simple diagram of the variables.

A detector measures the count rate of particles within the solid angle and an energy range (or a passband ΔE). To convert the count rate measured by the detector to an environmental flux, a geometric factor is required. The geometric factor is a combination of efficiencies and the physical view factor of the detector. The count rate is the integral of the differential flux over the solid angle and energy bandpass of

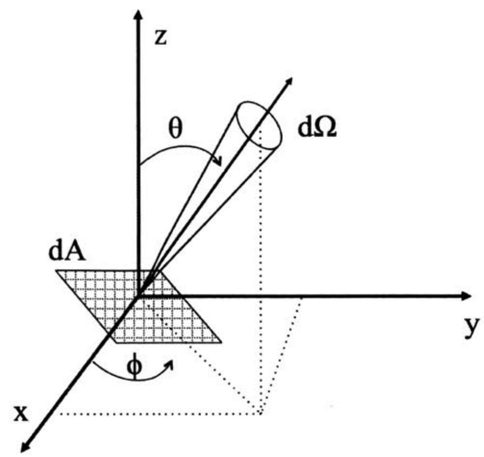

Figure 3-5: Diagram of the solid angle and area for a generalized flux calculation.

the detector, which is given by:

$$\mathrm{CR} = \int_{E_{\min}}^{E_{\max}} J(E)K(E)\mathrm{d}E \tag{3.1}$$

where CR is the count rate on the detector in counts per second; $K(E)$ is the geometric factor at the energy E in cm^2-sr; $J(E)$ is the differential flux at the energy E in $\#/\text{cm}^2$-sr-s-MeV; $E_{\min}$ and $E_{\max}$ are the minimum and maximum energies, respectively, over which the differential flux and geometric factors are defined [67, 115].

For an imager, we define the minimum threshold energy, $E_{\min}$, which includes contributions from all energies higher than the threshold as well. To define the energy that the imager is sensitive to, we choose the integer MeV energy at which >90% of particles are stopped, with 95% confidence, below that energy. For an imager that is differentially shielded (there are shorter or longer paths to different parts of the imager based on the location), there may be multiple possible integral energy channels. Rewriting Eq. 3.1 in terms of the integral flux,

$$\mathrm{CR} = \int_{E_{\min}}^{\infty} \left(\frac{\mathrm{d}I(E)}{\mathrm{d}E}\right) K(E)\mathrm{d}E \tag{3.2}$$

where the units are:

$$\frac{\#}{\mathrm{s}} = \left[\frac{\frac{\#}{\text{s-sr-cm}^2}}{\mathrm{MeV}}\right][\text{sr-cm}^2]\mathrm{MeV}$$

Geometric Factors

To determine the electron flux in the environment from pixels with energy deposited in them on the detector area, we break the factor $K(E)$ into two scaling factors. The number of particles that reach the detector and deposit energy depends on: the energy of the source particles, the number of source particles, the shielding materials (response to energetic particles, i.e., generation of secondaries) and geometry (thickness), and the surface area and material of the detector. The scale factors are calculated from the simulations.

We define two scaling factors: K_1 is the ratio of the number of particles reaching the detector to the number of pixels with energy deposited due to radiation in the detector area. K_2 relates the number of particles reaching the detector to the number of particles originating from the external environment. Figure 3-6 shows the relationship between the scale factors. Scale factors will be different for a given instrument, and must be calculated through analysis of charged particle transport simulations. They need only to be calculated once and can be done before, during, or after the mission. Ideally, the calculated scale factors would be validated by experiments on the ground.

To calculate the scale factors, we examine the mono-energetic simulation results. Starting with the known simulation environment, the simulated source particle flux, $f_{\text{sim}}(E)$, for a given energy is from one billion source electrons, coming from a 4π steradian sphere with radius $r_{\text{sim}} = 150$ cm. Recall, the simulated flux is a factor of four larger than the real environment. This is accounted for in the scale factors. Then, we examine the number of particles P_1 that make it through the spacecraft and instrument shielding and reach the detector. We relate the two quantities with scale factor K_2, which has units of steradian:

$$K_2(E) = \frac{P_1}{f_{\text{sim}}(E)} \tag{3.3}$$

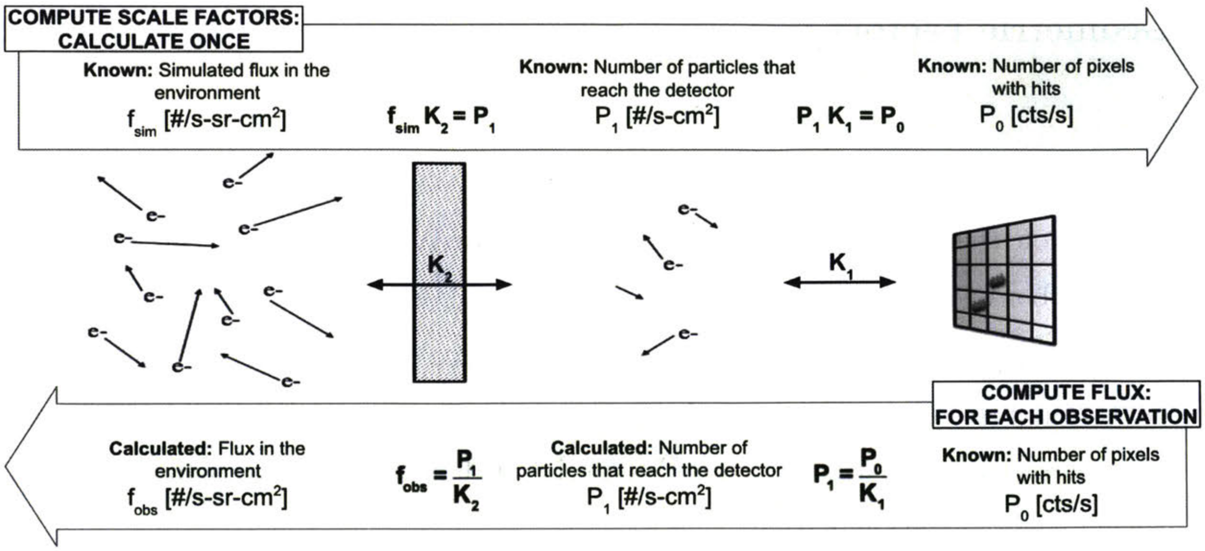

Figure 3-6: Description of how to calculate scale factors using simulation results and how to use the scale factors to compute the flux in an observation. This diagram should be read starting at the top left-hand corner and moving clockwise around the figure.

where the units are:

$$\text{sr} = \frac{[\#/\text{s-cm}^2]}{[\#/\text{s-sr-cm}^2]}$$

Next, we count the number of pixels that have energy deposited in them and compute the ratio with the total number of pixels analyzed, P_0, and compare it to the number of unique particles (primary and higher orders) that reach the detector and deposit energy. Since P_0 is the fraction of the pixels with hits, the scale factor includes the pixel area: 15 mm x 15 mm per pixel. P_0 and P_1 are related with the scale factor K_1, which has units of square centimeters:

$$K_1 = \frac{P_0}{P_1} \tag{3.4}$$

Then, for each imager observation, the scale factors are used to calculate the flux in the environment. The only known quantity is P_0, which is the percentage of pixels with energy deposited in them over the exposure time. Using K_1, one can find the number of particles that created those pixel hits. Using K_2, one can then find the estimated flux in the environment. A summary of how the scale factors are calculated

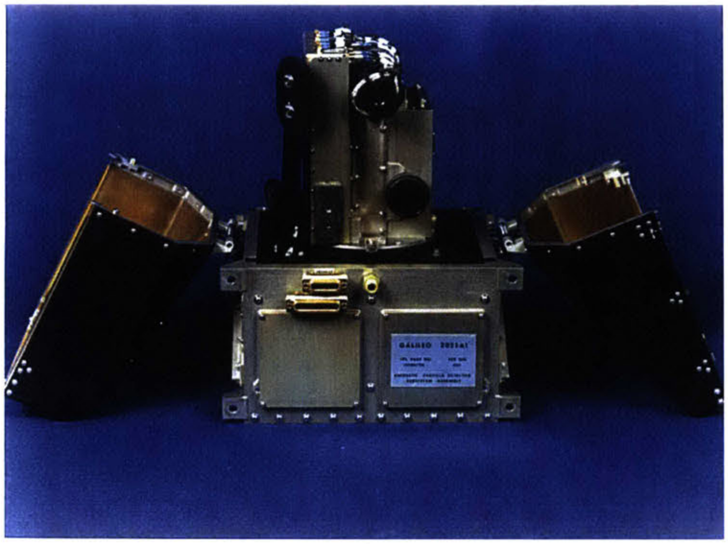

Figure 3-7: Photograph of the Galileo EPD. Image source: Williams et al. (1992) [116].

and then how they are used to find the flux from an observation is given in Figure 3-6.

Putting it all together, starting with P_0, the environmental flux is calculated as follows:

$$f_{\text{sim}}(E) = \frac{P_0}{K_1 K_2(E)} \tag{3.5}$$

In the literature, the geometric factor is typically reported as just one factor. We can combine the two scale factors to be $K(E) = K_1 K_2(E)$ with units of sr-cm^2.

3.5 Comparison with the Galileo Energetic Particle Detector

To assess the accuracy of the method developed, we compare the calculated fluxes from the images to the Galileo Energetic Particle Detector (EPD). The EPD provides 4π steradian angular coverage spectral measurement for Z$\geq$1 ions, electrons, and the elemental species helium through iron. The EPD consists of two telescopes called the Low Energy Magnetospheric Measurement System (LEMMS) and the Composition Measurement System (CMS) (see Figures 3-7 and 3-8). The LEMMS is the most applicable for our studies. The LEMMS detector head is a double-ended telescope

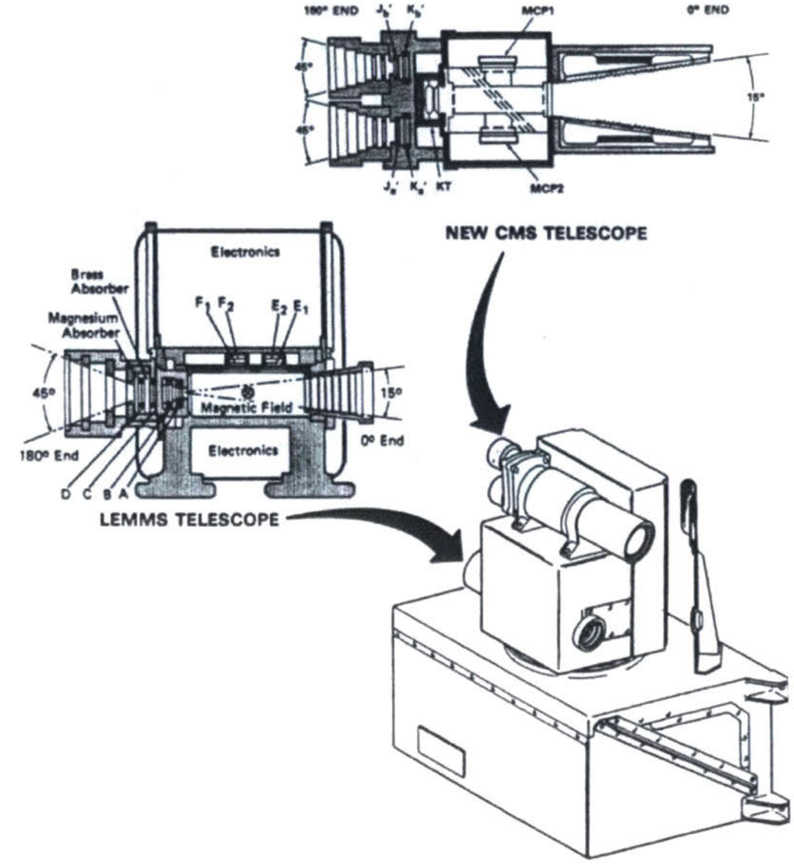

Figure 3-8: Schematic of the EPD telescope heads and the overall EPD configuration. Image source: Williams et al. (1992) [116].

(the detector receives particle measurements from two sides) containing eight heavily shielded detectors providing measurements of electrons from 15 keV to >11 MeV, and ions from 22 keV to ∼55 MeV, in 32 ranges of energy channels. Of the LEMMS channels, the most important ones for our study of the SSI and NIMS are the DC3 and DC2 electron channels, which are integral flux measurements of >11 MeV and >2 MeV electrons, respectively. More information on the EPD can be found in [116].

The goal is that the techniques developed in this thesis will be capable of computing fluxes from images that are comparable to measurements from the EPD. Agreement with the EPD data is not necessarily validation; there is a spread in the EPD data, which comes from variations in the environment and statistical uncertainties in the measurement. But, the calculated fluxes from the imagers should have relative

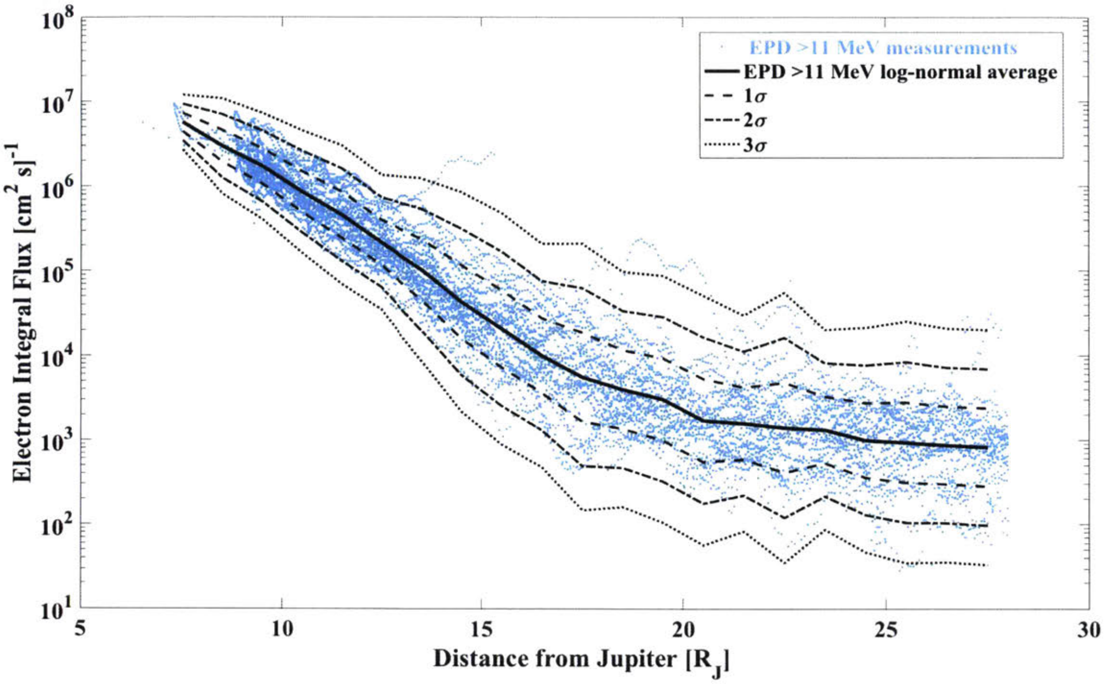

Figure 3-9: Galileo EPD >11 MeV integral flux channel (DC3) as a function of distance from Jupiter in R_J (blue dots). The log-normal average of the data is plotted as a solid black line. The 1σ, 2σ, and 3σ spreads are drawn in dashed lines. Data are from [65]. Computed fluxes from images are directly compared to the data in this plot.

agreement with the EPD measurements. Figure 3-9 shows the EPD >11 MeV electron integral flux measurements as a function of radial distance from Jupiter (in R_J). Jun et al. (2005) find a log-normal fit to the EPD data DC3 integral flux, which is shown as a solid black line in Figure 3-9. The statistical spread (1σ, 2σ, and 3σ) on the flux average is marked with dashed lines [65]. The flux values computed from the images will be plotted directly on the data in Figure 3-9.

Another system commonly used for looking at environmental data around Jupiter (and also Earth) is the magnetic B and L system, which is relative to the Jovian magnetic field axis. Looking at the EPD data in terms of the L-shell, computed using the VIP4 magnetic field model [27], removes some of the radial "ripples" seen in Figure 3-9 inside ~16 R_J. Unfortunately, the L-shell concept starts to lose its meaning beyond this distance. Therefore, we present the radial distance system in this work.

Chapter 4

Analysis of the Galileo Solid-State Imaging Instrument

4.1 SSI Instrument Overview

The Galileo Solid-State Imaging (SSI) experiment on the Galileo mission is a high-resolution, multi-spectral charge-coupled device camera, designed to study Jupiter and its satellites [13]. The principal investigator is Dr. Michael Belton, originally affiliated with Kitt Peak National Observatory. The optical system used is a modified flight spare of the narrow-angle telescope flown on Voyager consisting of a 1500 nm focal length (f/8.5), all-spherical, catadioptric telescope. The SSI operates in a spectral range of approximately 375 nm to 1100 nm using eight filtered band passes. The field of view of the telescope is 0.46 degrees with an angular resolution of 10.16 microradians/pixel. The telescope dimensions are approximately 90 x 25 x 30 cm^3, with a mass of 28 kg, and peak power draw of 23 W. Additional details on the telescope can be found in Belton et al. (1992) [13]. A photograph of the SSI and a labeled diagram of the key components and optical path can be found in Figures 4-1 and 4-2, respectively.

The detector is an 800 by 800 pixel virtual-phase, frontside-illuminated, silicon CCD. The dimensions of the detector are 12.19 mm by 12.19 mm with a 65.6 pixel per millimeter pixel density. Each pixel is 15 µm by 15 µm. The full-well capacity is

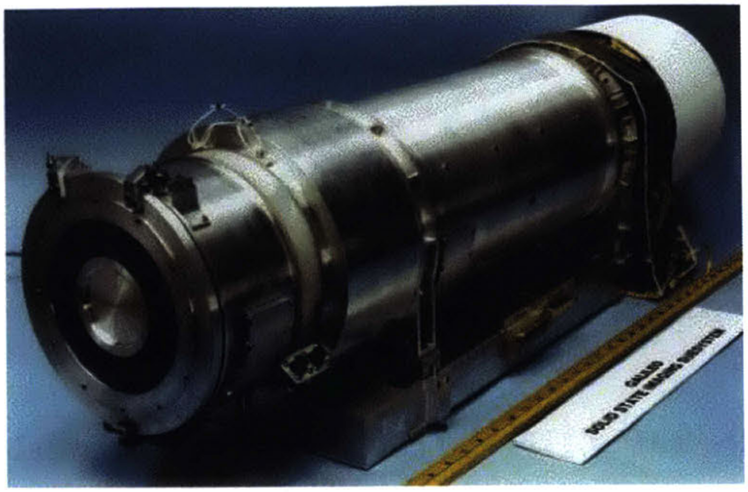

Figure 4-1: Picture of the SSI instrument from [13]. The entrance aperture is on the left, the white appendage on the far right is the radiative cooler for the detector, and the box beneath the main body of the telescope is for camera electronics.

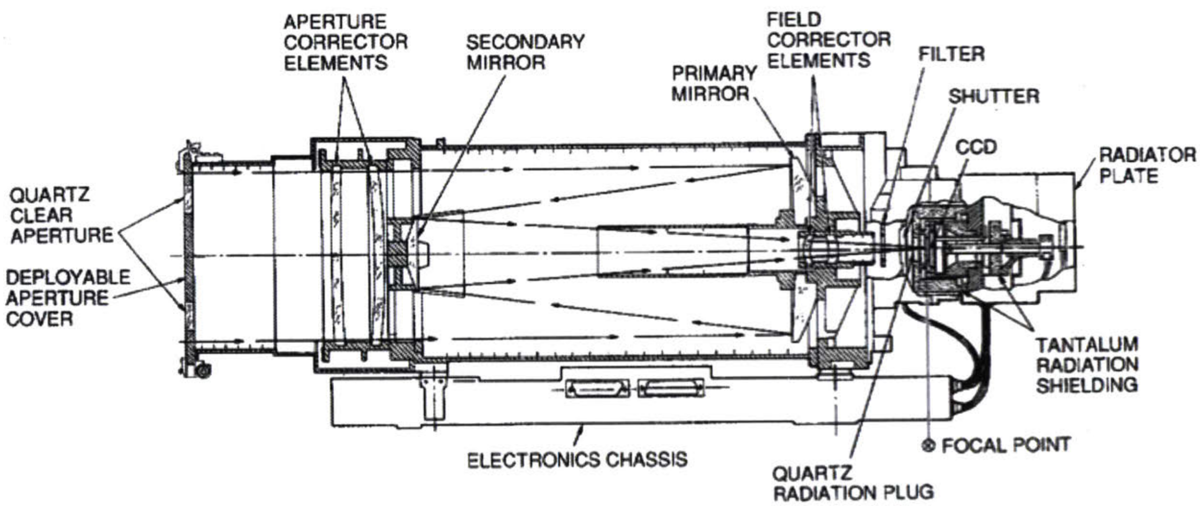

Figure 4-2: Labeled diagram of the basic elements of the SSI instrument from [13].

108,000 e- (in normal modes) and the noise floor is ±30 e- [13, 58, 71]. During image readout, all 800 lines are simultaneously shifted in the column (parallel) direction causing the first image line to be shifted through an on-chip amplifier. This line readout process is repeated until all 800 lines have been readout. The line readout rate (and therefore the associated noise from radiation and other sources) is identical for all the SSI operating modes. As long as the external radiation flux is fairly constant on a time scale of one frame cycle, the radiation noise will show a top-to-

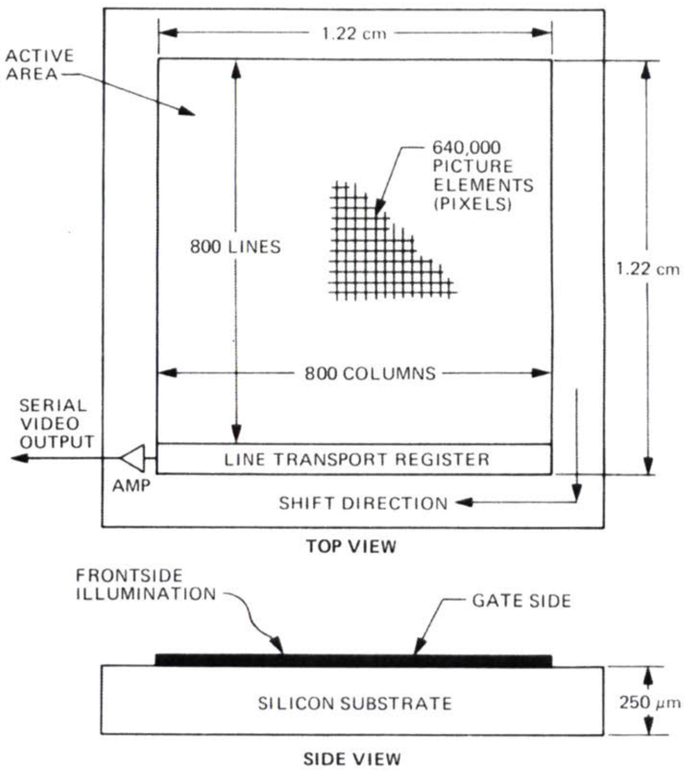

Figure 4-3: Layout of the 800 by 800 pixel virtual-phase CCD for the Galileo SSI. Image source: Janesick et al. (1981) [58].

bottom gradient, since the lines at the top are read out first (less integration time for radiation accumulation) and the bottom lines are read out last (more integration time for radiation accumulation). A schematic of the SSI CCD can be found in Figure 4-3. For more details on the camera system, detector response, and early in-flight performance, see Janesick et al. (1981), Klaasen et al. (1984), and Belton et al. (1992) [13, 58, 75], and references therein.

4.2 Particle Transport Simulations in the SSI

We model the Galileo SSI instrument in three dimensions, a cut-away visualization of which is shown in Figure 4-4 with labels of the key components. Both the materials and physical placements are accounted for in the geometry.[1] We include representative

[1]Information to build the geometry came from individuals at the Jet Propulsion Laboratory: Shawn Kang, Michael Cherng, Ken Klaasen, and Herbert Breneman.

shielding from the spacecraft (1.4 steradian aluminum cone), but it is negligible for the most part: the SSI is on the scan platform, which is >1.5 m from the spacecraft, so the Galileo spacecraft blocks a solid angle of only ~1.4 steradian (11% of 4π steradian) as viewed by the SSI.

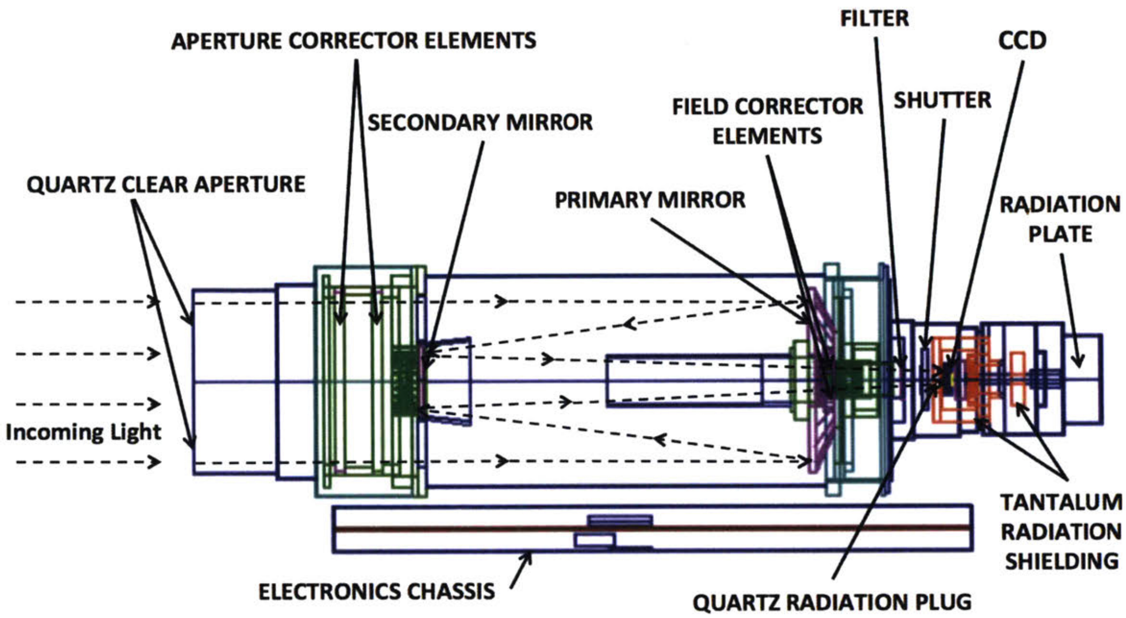

Figure 4-4: Cut-away visualization of the geometry built in Geant4 of the SSI. The key components are labeled and colors correspond to the material of the element (yellow: silicon, dark blue: aluminum, cyan: titanium, green: invar, pink: silica, red-orange: tantalum, brown: circuit board). Shielding from the spacecraft is not shown in this diagram. The visualization is produced using the software HepRep [90].

4.2.1 Geant4 Results

We perform mono-energetic electron simulations as described in Section 3.2.2. Table 4.1 shows the averaged results from five runs of Geant4 simulations of one billion electrons at the following energies: 1, 3, 5, 10, 30, 50, 100, and 200 MeV. For each energy, the number of unique primary and secondary *particles* that reach the detector (and deposit energy) and the number of *pixels* with energy deposited in the 800 by 800 pixel array are recorded. Secondary particles are any order (2nd, 3rd, etc.) particles higher than primary particles. We find that roughly 10% of particles reaching the detector are primaries, which is consistent with Becker et al. (2017b) [12]. In Table 4.1,

Table 4.1: Averaged results of five Geant4 simulations of one billion electrons with energies 1, 3, 5, 10, 30, 50, 100, and 200 MeV for particles that reach the SSI detector and deposit energy. Columns B and C are the numbers of unique primary and secondary particles that deposit energy on the detector, respectively, and their sum is in Column D. Column E is the total number of pixels with energy deposition ("hits").

A	B	C	D	E
Energy [MeV]	Avg. # Hits from Primaries	Avg. # Hits from Secondaries	Avg. # Particles that Reach Detector (B + C)	# of Pixels with Energy Deposited
1	0	0	0	0
3	0	4.2	4.2	6.0
5	0.6	13.2	13.8	30.4
10	41.4	101.2	142.6	240.6
30	308.4	1014.8	1323.2	2532.6
50	611.4	2581.2	3192.6	6061.4
100	1165.2	8006.8	9172.0	17988.8
200	1971.6	20602.2	22573.8	44797.0

Columns B and C are the numbers of unique primary and secondary particles that deposit energy on the detector, respectively, and their sum is in Column D. Column E is the total number of pixels with energy deposition ("hits"). The results for each of the individual runs are provided in Appendix C.

The mono-energetic simulations of 1, 3, and 5 MeV electrons result in little or no energy deposited on the detector (fewer than 0.01% of pixels with hits). For electrons below 10 MeV, over 90% of the intensity of the primary electrons are stopped, so we assert that the SSI is capable of integral electron energy detection of $\geq$10 MeV. The minimum equivalent shielding of aluminum for the detector is 18.7 mm (or $\sim$740 mils), which was calculated using the FASTRAD software.[2] The equivalent aluminum shielding thickness corresponds to a dose depth penetration of $\sim$10 MeV electrons [29], which is consistent with the simulation findings.

[2]FASTRAD Software, TRAD, Tests, & Radiations `http://www.fastrad.net`

4.2.2 Scaling Factors

Following the process outlined in Section 3.4, to convert the fraction of pixels with energy deposited to the flux in the environment, we find two scaling factors from the simulation results. Referring to the mono-energetic simulation results, in Table 4.1, ignoring 1, 3, and 5 MeV because those runs deposit little or no energy on the detector, there is roughly a common factor relating the fraction of pixels with energy deposited (column E) to the number of unique primaries and secondaries that reach the detector (column D). This number includes the size of a SSI pixel (2.25×10^{-6} cm^2). Every particle traverses roughly two pixels on average. Using the known simulated environmental flux, we calculate the second scale factor, K_2, for each energy. Table 4.2 shows the scale factors for 10-200 MeV with the 95% confidence interval and Figure 4-5 shows the combined scale factor for the SSI, $K(E) = K_1 K_2(E)$.

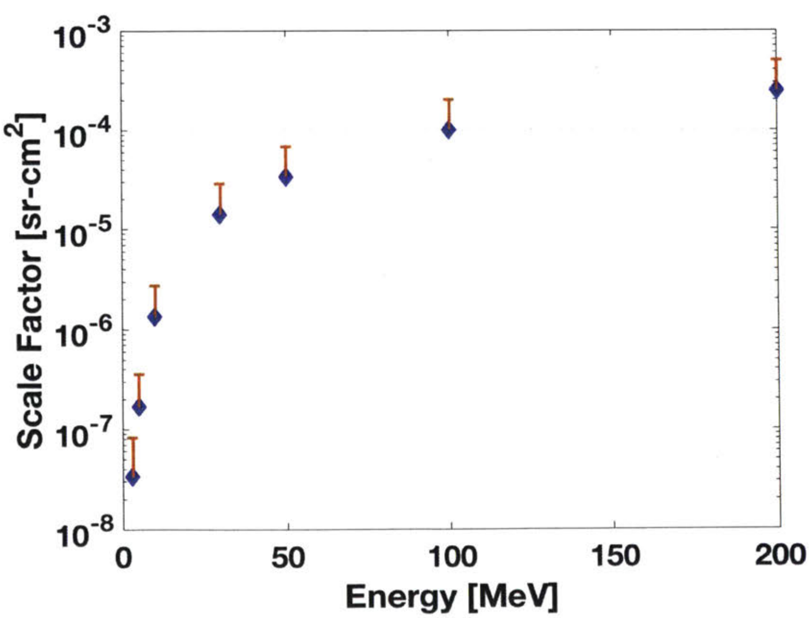

Figure 4-5: Combined calculated scale factor as a function of energy for the SSI.

Table 4.2: Scale factors computed for the averaged results of five Geant4 simulations of one billion electrons with energies 10, 30, 50, 100, and 200 MeV for particles that reach the SSI detector and deposit energy. K_1 is the scale factor converting the particles reaching the detector to the fraction of affected pixels. K_2 is the energy-dependent geometric scale factor that relates the particle count rate at the detector to the environmental flux for a given energy. Each scale factor includes the 95% confidence interval.

Energy [MeV]	Particles per Pixel Scale Factor, K_1 [cm^2-cts/particle]	Geometric Scale Factor, K_2 [sr]
10	$2.636 \pm 0.0130 \times 10^{-6}$	0.5067 ± 0.028
30	$2.991 \pm 0.0049 \times 10^{-6}$	4.701 ± 0.164
50	$2.967 \pm 0.0074 \times 10^{-6}$	11.34 ± 0.185
100	$3.064 \pm 0.0057 \times 10^{-6}$	32.59 ± 0.279
200	$3.100 \pm 0.0030 \times 10^{-6}$	80.21 ± 0.424

4.3 SSI Data Analysis

4.3.1 Data Collection

We collect the raw images and their associated calibration files (dark current, blemish, and shutter offset files) from the PDS.[3] We use the U.S. Geological Survey's Integrated Software for Imagers and Spectrometers (ISIS), which is a software package for digital image processing, to read in the PDS-formatted images and output them to text files. There are other processing tools for missions (including Galileo) but they all involve processing and "correcting" of the data, so we do not use them. The only routines we use are: `gllssi2isis`, which converts the Galileo SSI image to ISIS formatting, and `isis2ascii`, which converts the ISIS image to text. The file includes some header information for the image as well.

Due to an anomaly with the Galileo high-gain antenna [60], severely reducing the data downlink capability, a majority of the images were highly compressed with loss of information. Data were compressed in three ways: block-adaptive rate control

[3]`https://pds-imaging.jpl.nasa.gov/`

(BARC) as they recorded to the tape or integer cosine transfer (ICT) or Huffman compressed as they were read from the tape and transmitted to Earth. There are some instances when compression was not used as well. Figure 4-6 shows the cumulative exposure time for each compression type binned by integer R_J. The majority of the exposure time was spent in BARC and ICT modes, which are lossy and smooth over radiation or remove it completely before transmission. One mode of ICT compression is lossless and can be used for our analysis, but in general, ICT compression is not an option. The on-board despiking routine replaces an unusually high pixel with an average from the surrounding pixels. Therefore, we select the images that have not undergone lossy compression or spike reduction on-board, leaving only 767 out of a total of 4002 (19%) of images for evaluation in this study.

Occurring for the first time just before Galileo's arrival at Jupiter, the tape recorder began periodically sticking. This anomaly did not have any apparent permanent damage but led to changes in operating rules, including limiting high-speed recording, additional cooling after imaging, and unstick movements before frames. From the reduced data expectations from the HGA anomaly, the tape sticking reduced the image data return by an additional 30% [72].

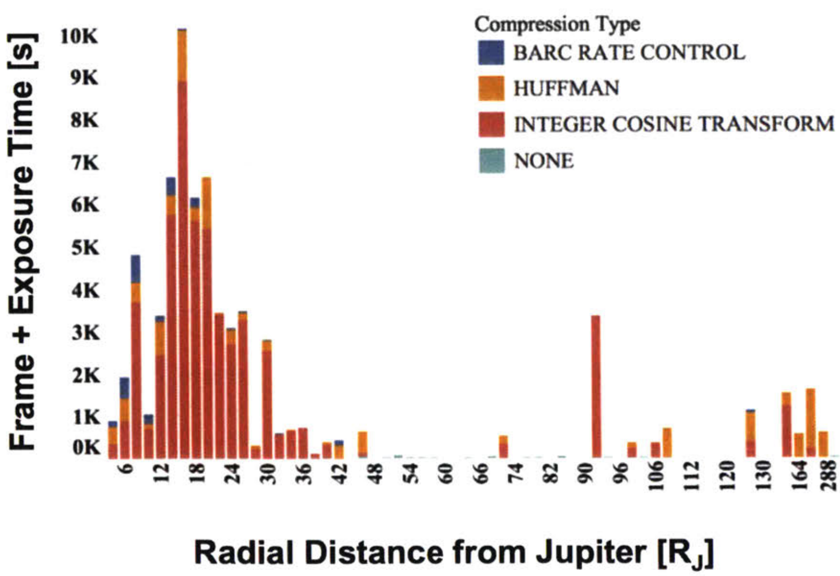

Figure 4-6: Comparison of total exposure times for SSI compression types.

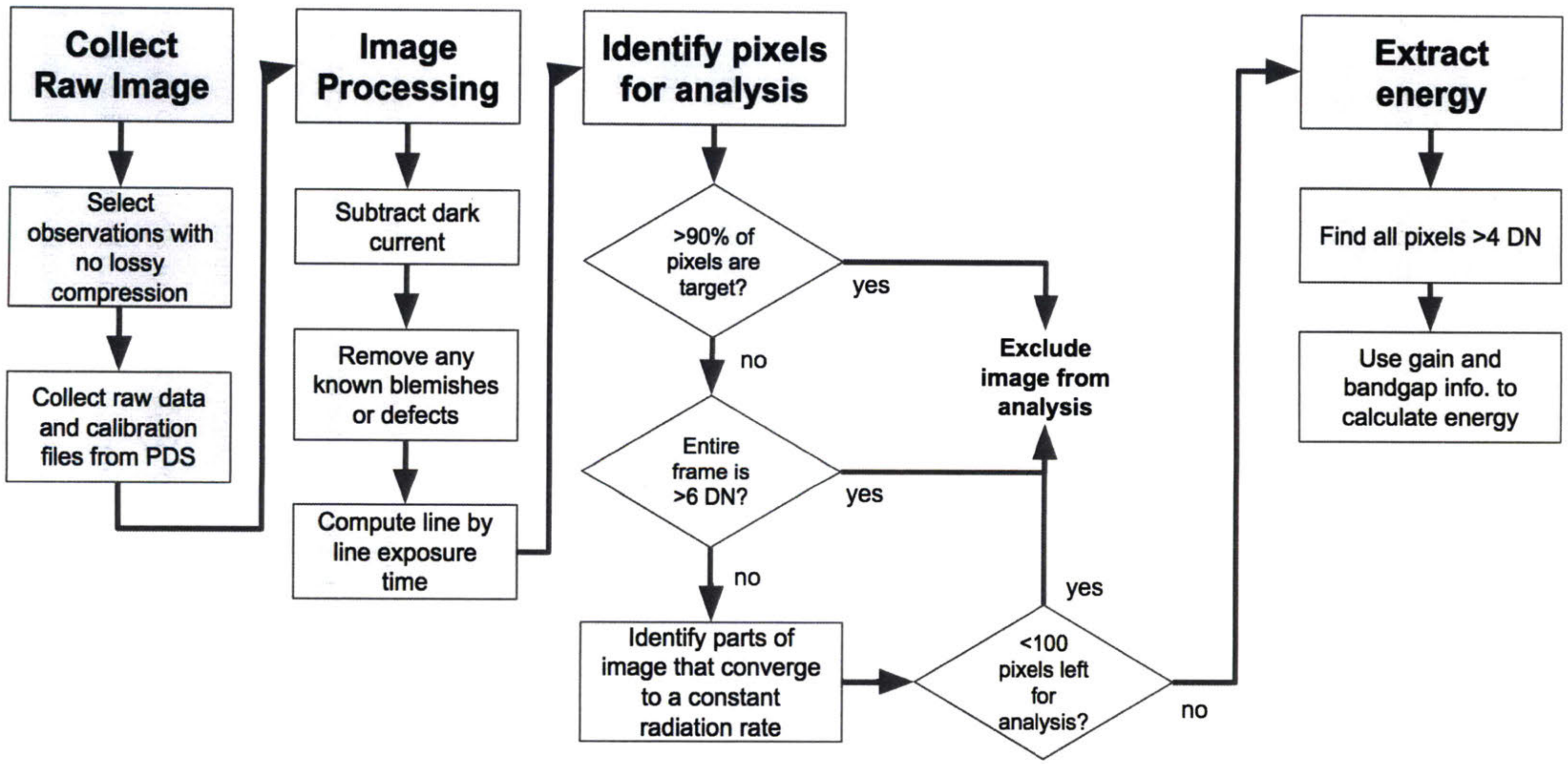

Figure 4-7: SSI image processing flow diagram. See Section 6.2.1 for a discussion of the DN threshold sensitivity.

4.3.2 Image Processing

To collect the radiation noise from an SSI image, we must remove any pixels that may be affected by other sources. We remove the dark current, known blemishes, and the target of the observation (such as a moon or planet). We calculate the exposure time for the image and convert the DN to the energy deposited in each pixel. Figure 4-7 shows a diagram of the image processing pipeline.

Subtract the dark current. Dark current occurs due to thermal energy in a device. If the temperature is high enough, electrons are freed from the valence band and become collected within the potential well of a pixel. The dark current electrons become part of the signal, indistinguishable from the object photons (and radiation noise). Dark current is a strong function of the temperature of the device and extensive calibration is typically required. For the SSI, dark current files are created for each combination of gain state, frame mode, compression type, etc.

We subtract the dark current file for each image based on the time of the image, gain state, frame mode and rate, clock state, exposure mode, readout mode, and blemish mode. Dark frames for calibration were taken only three times during the mission once at Jupiter and were taken at >50 R_J, where the flux is only approximately 1.26×10^5 e-/cm^2-s-MeV at 1 MeV, though Klaasen et al. (2003) claim no noticeable change in the dark current over each of the dark current updates [74].

Remove blemishes. Column blemishes and dark spikes are due to single-pixel defects in the SSI CCD. These defects are primarily from high-energy heavier particles (protons from solar particle events, heavy ions in the form of cosmic rays) and/or from neutrons generated by the spacecraft's radioisotope thermoelectric generators (RTGs). The blemishes can be annealed and appear at a rate of about two to three per orbit [73]. As such, there is an associated blemish file for the majority of the images, which contains information on specific pixels and columns that should be ignored in the analysis. There are known long-term charge traps in the detector at column 170 and 610, so these columns are ignored in the analysis as well [71].

Table 4.3: Gain states for converting digital number to electrons. The gain state ratio factors are found in the calibration files. Uncertainties from the original calibration can be found in the JPL calibration report [71]. Temperatures are in Kelvin (K).

Commanded Gain	Ratio Factors	Conversion	Notes
0 = Gain 1	1.00	1822 e-/DN	Summation mode only, ~400 K full scale
1 = Gain 2	4.824	377.4 e-/DN	Low gain, ~100 K full scale
2 = Gain 3	9.771	186.5 e-/DN	~40 K full scale
3 = Gain 4	47.135	38.66 e-/DN	High gain, ~10 K full 255 DN scale

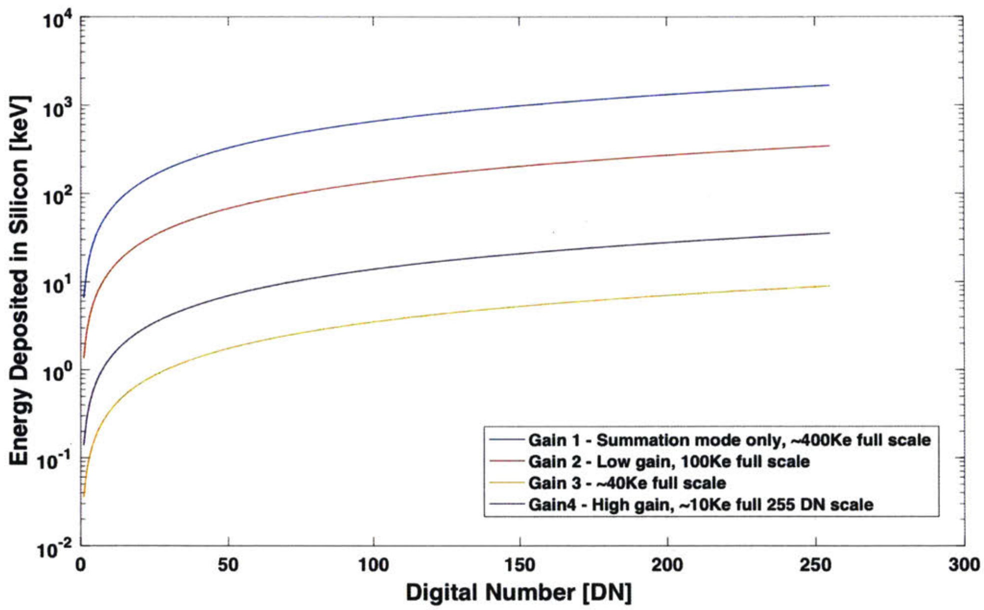

Figure 4-8: Conversion from the digital number (DN) to energy deposited for the SSI gain states.

Conversion to electrons using the gain states. The calibrated instrument gain is used to convert the digital number (DN), ranging from 0 to 255, in the image to electrons. There are four gain states and their factors can be found in Table 4.3. For silicon, to convert the electrons to the energy deposited in each pixel, we apply the ionization energy needed to create an electron-hole pair: 3.6 eV/e- [76].

Radiation Exposure Time and Shutter Files. The readout of the detector is roughly linear, allowing us to calculate the average exposure time for each line. For a given observing mode, we can calculate the time the image is exposed to radiation using a combination of the exposure duration, readout duration, prepare time, and end of erasure time. See Appendix D for details on SSI observing modes and how to calculate the radiation integration time [71].

The shutter offset file, which is independent of all camera modes, contains the line dependencies due to the acceleration of the shutter blades, which travel in a vertical direction. The offset file contains 800 values, one for each line. Measured and calibrated during cruise to Jupiter, the values in the file are assumed to be unchanged through the duration of the mission [73].

4.3.3 Radiation Extraction

To collect the radiation noise from an SSI image, we must identify and remove any pixels that may have contributions from sources, such as the moon or target of the image. The radiation extraction steps (determination of pixels for analysis) are summarized on the right half of Figure 4-7. We take a conservative approach and only evaluate pixels we are confident are due to radiation and not another source. This conservatism is opposite to that of traditional noise removal algorithms that err on the side of identifying more pixels (e.g., [4, 92]); those algorithms remove anything with the slightest chance of being radiation.

If over 90% of the pixels are from the target, the image is excluded from the analysis. The remaining background is dominated by stray light from the target and there are too few pixels remaining. If the entire image frame contains pixels with a high DN ($\geq$6 DN, which corresponds to $\sim$2,300 electrons in the most common gain state), we exclude the image from the analysis. In this case, the image is assumed to be saturated.

To extract the target in the image, we remove the high DN regions along each line of pixels. The background of the image should be uniform across the line since the radiation rate per line on the SSI isn't spatially dependent: the radiation is omni-

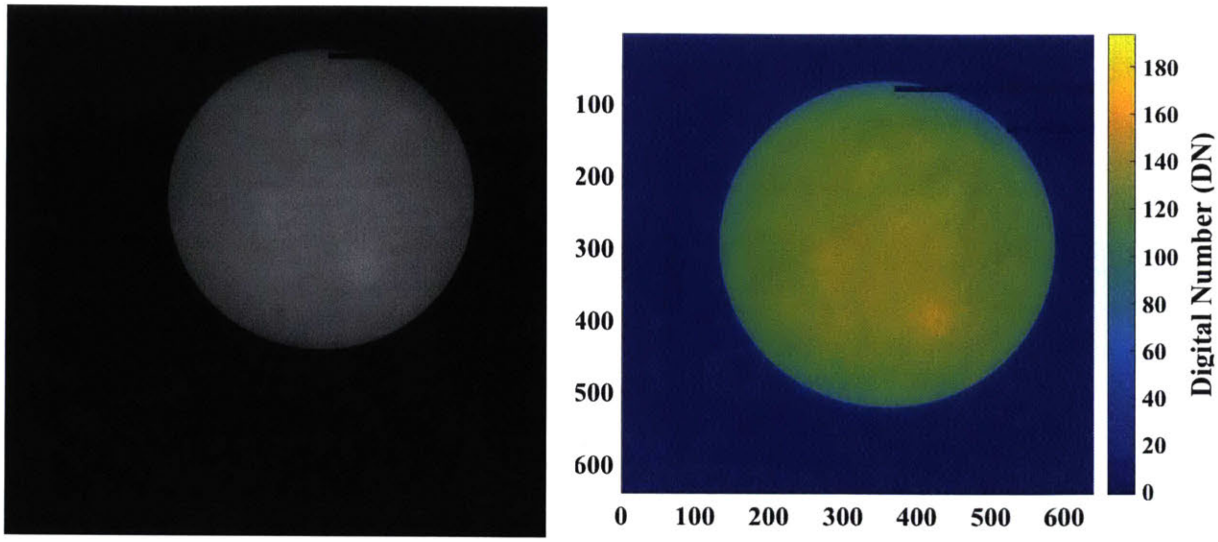

Figure 4-9: Right: Raw image of 3926r observation, retrieved from the PDS on 20 April 2018. Left: Contrasted image of 3926r observation to show the DN range.

directional and the SSI is equally shielded in the plane of the detector. The particle simulations confirmed this claim (see Figure 3-4). We continue to remove the pixels along the edges of the target until the remaining pixels converge to a linear, constant background rate.[4]

Using SSI image 3926r as an example (see Figure 4-9 and the next section for more details on observation 3926r), Figure 4-10 shows an example of the DN across one line (line 400) of the image. The moon, Europa, is near the center of the image. At about column 200 and less, the background of the image is roughly constant, as well as columns greater than 700. Then, looking at the columns with nearly constant rates, we select the DN hits that are above the background. For the SSI, we select a threshold of >4 DN. See Section 6.2.1 for a discussion of the DN threshold sensitivity. In most cases, in the region identified as the target, there are pixels with DNs much greater than the target average. These are likely radiation hits as well, but they are excluded from the analysis for now.

Once a set of pixels is identified for analysis, we require that there need to be

[4]There is a glow along the outside of the actual target that comes from reflection internal to the telescope and albedo from the target, so this is removed as part of the process. See Appendix D for more details.

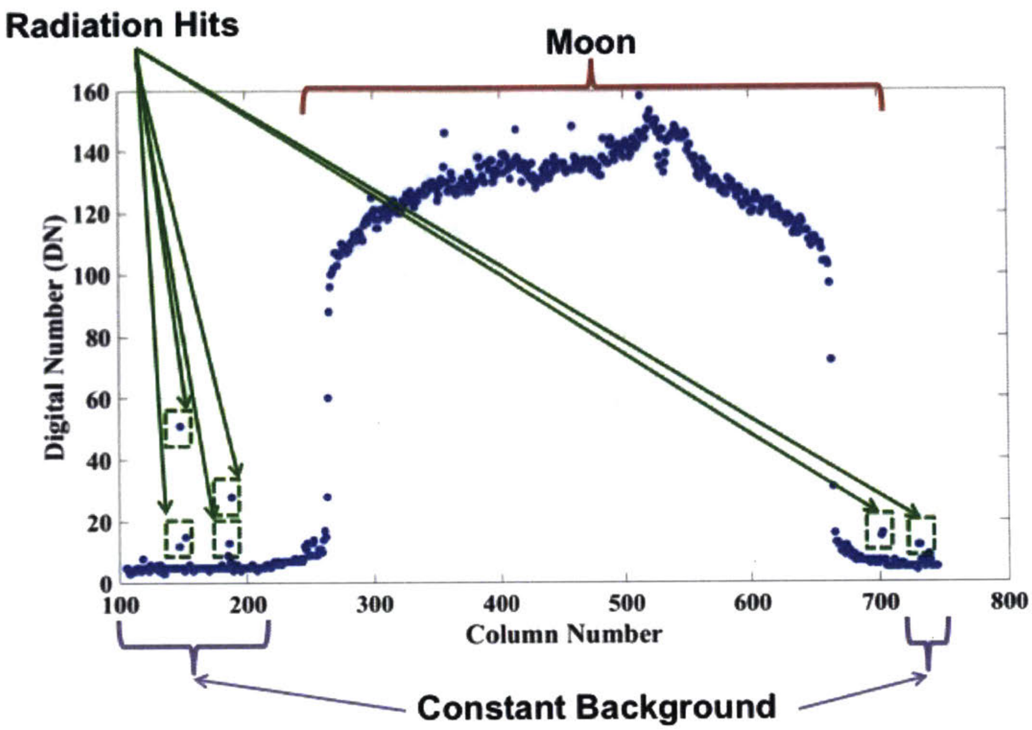

Figure 4-10: Example of line 400 of SSI observation 3926r. We identify the region dominated by the moon for removal and the constant background region, from which we can extract radiation hits.

greater than 100 pixels remaining for analysis for statistical reasons. When the constraints outlined in this section are applied, 766 out of 4002 images are available for analysis. The intersection of these images with the possible images based on requiring lossless compression leaves 179 images for analysis.

4.4 Example of Calculating the Flux from a SSI Observation

We demonstrate the calculation of the flux from SSI image '3926r', observed during the second orbit of the Galileo mission at Jupiter. The observation target is Europa.

Table 4.4: SSI observation 3926r parameters.

Image Parameters	Values
Orbit number	2
Target	Europa
Distance from Jupiter	10.67 R_J
Observation time	1996-09-07 14:43:23.490Z
Gain state	3 (186.5 e-/DN)
Telemetry format	IM8
Compression type	ICT (lossless)
Frame duration	8.667 s
Exposure duration	529.17 ms
Prepare Time	2 s
End of Erase Time	1.14165 s
Dark current file	3f8.dc04.cub
Blemish file	n/a
Shutter file	calibration.so02F.cub

Relevant observation details can be found in Table 4.4. Figure 4-9 shows the raw data for observation 3926r and the raw data contrasted with a DN scale. The observation has an exposure duration of 529.17 ms and a frame duration of 8.667 s.

A 640 by 640 pixel subset of the 800 by 800 pixel full array is used. To enhance the data return following the high-gain antenna (HGA) deployment failure, there are windowing options available. The image may be edited so that only an image area (called a cut-out window) remains. For 3926r, the cut-out window starts at line 1, sample 105, and has a width of 640 samples and a height of 640 lines.[5]

We subtract the dark current (filename `3f8.dc04`). Upon eliminating the moon (procedure outlined in Section 4.3.1), one can see the radiation hits as bright pixels within the otherwise dark, photon-deficient environment surrounding the moon.

[5] `https://pdsimage2.wr.usgs.gov/archive/go-j_jsa-ssi-2-redr-v1.0/go_0017/document/redrsis.htm`

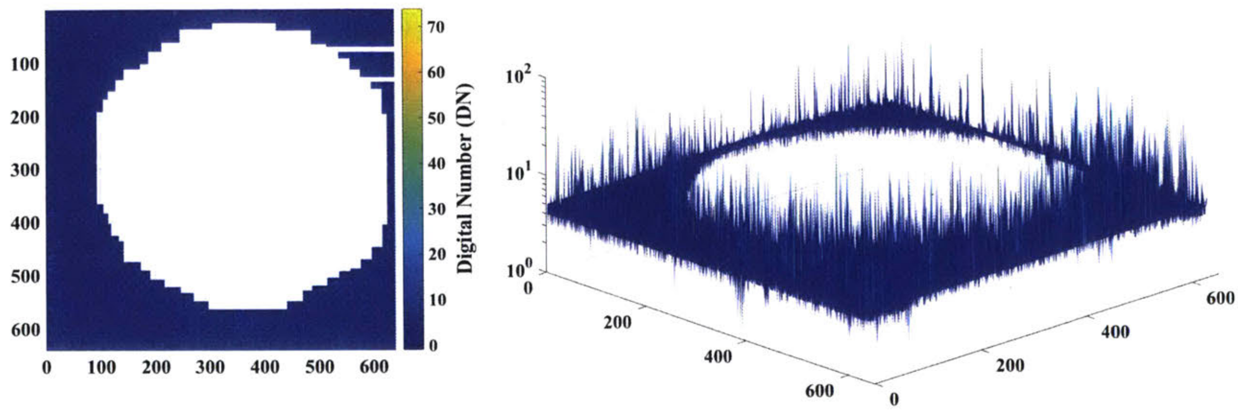

Figure 4-11: Contrasted image of 3926r with the dark current and target, Europa, removed. On the right, the DN on the z-axis is in log-scale to demonstrate the higher frequency and magnitude of radiation hits at the bottom half of the image. Notice, the lower half of the image has more radiation by eye than the top half. This is due to the readout of the detector, that starts line by line at the top of the image.

Figure 4-11 shows the contrasted image remaining and, on the right of the figure, the log-scale of the DN, demonstrating the increasing frequency and magnitude of radiation hits in the image as line number increases. Of the original 409,600 pixels, 176,665 pixels (43.13%) are available for radiation analysis. We find the number of pixels with >4 DN to be 150,402 pixels. From here, we turn the number of pixels with 'hits' into the percentage of the pixels evaluated. P_0 is the percentage of pixels with hits, scaled to the number of pixels with hits per unit time. The average exposure time per line for this image is 3.5293 s. This is roughly from the total readout time (8.666 s) divided by the average line number. See Appendix D for more details on how the exposure time is computed.

$$\begin{aligned} P_0 &= \frac{\text{percentage of pixels with hits}}{\text{exposure time}} = \frac{\frac{150{,}402\text{px}}{176{,}665\text{px}}}{3.5293\,\text{s}} \\ &= 0.2412\,\text{cts}\,\text{s}^{-1} \end{aligned}$$

Using the scale factors determined in Section 4.2, we compute the ≥10 MeV integral flux. For ≥10 MeV, $K_1 = 2.636 \pm 0.013 \times 10^{-6}$ cm^2 and $K_2 = 0.5067 \pm 0.028$ sr. Following Eq. 3.5:

$$\begin{aligned} f_{\text{obs}}(E \geq 10 \text{ MeV}) &= \frac{P_0}{K_1 K_2 (E \geq 10 \text{ MeV})} \\ &= \frac{0.2412 \, \text{cts} \, \text{s}^{-1}}{(2.636 \times 10^{-6} \, \text{cm}^2)(0.5067 \, \text{sr})} \\ &= 1.8060 \times 10^5 \, \text{e-} \, \text{cm}^{-2} \, \text{sr}^{-1} \, \text{s}^{-1} \end{aligned}$$

The flux in observation 3926r observation flux is calculated to be 1.8×10^5 e- cm^{-2} sr^{-1} s^{-1}. The closest EPD measurement to 3926r was taken less than two minutes after the SSI image and has a >11 MeV flux of 4.53×10^4 e- cm^{-2} sr^{-1} s^{-1} (or, 5.69×10^5 e- cm^{-2} s^{-1}). The 3926r observation is within 1σ of the EPD log-normal average fit, which is shown in Section 4.5.

4.5 Comparison to EPD

We calculate the ≥10 MeV flux for 43 SSI observations. Figure 4-12 shows the fluxes compared with the log-normal EPD fit as a solid black line, as a function of the distance from Jupiter (in radii of Jupiter, R_J) and the 1σ, 2σ, and 3σ on the fit. For the SSI fluxes, the 1σ error bars are included. The error bars on the SSI flux measurements are purely based on Poisson counting statistics. The 1σ error is $\pm\sqrt{N}$, where N is the number of pixels with radiation hits considered. Then, the upper and lower limits of the number of particles with radiation hits are used to compute the lower and upper 1σ bounds on the flux. The error bars for each SSI image are small; some are within the size of the data point marker (and note that the y-axis scale is logarithmic). The SSI-calculated fluxes show excellent agreement to the EPD, demonstrating confidence in the method. The results are interpreted in further detail in Chapter 6.

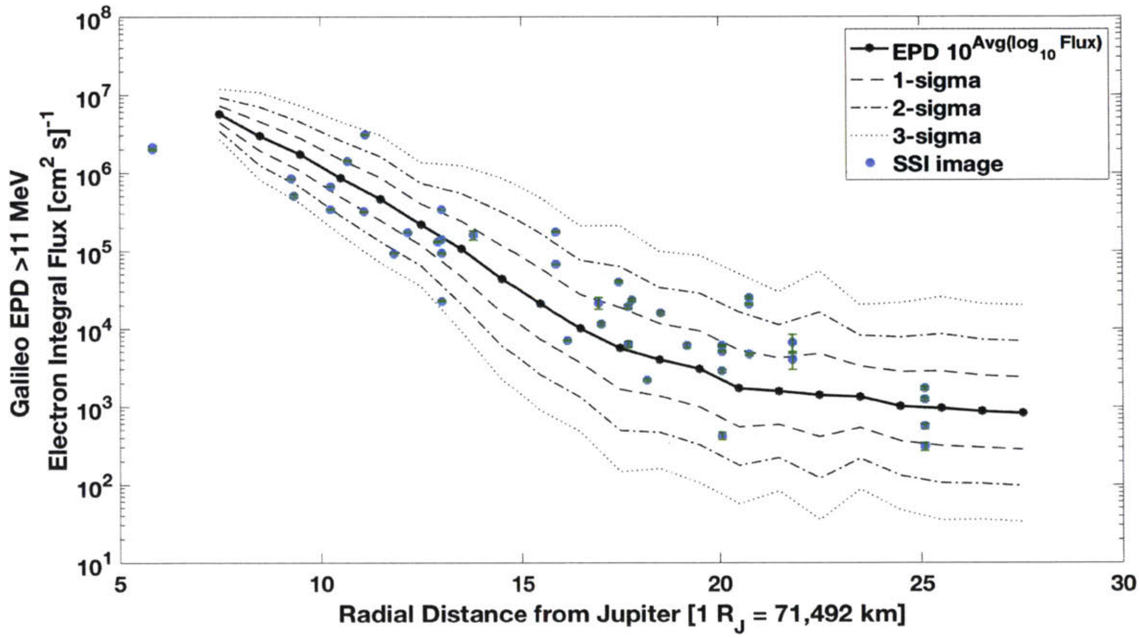

Figure 4-12: SSI results for 43 images compared with the log-normal fit of the Galileo EPD >11 MeV integral flux channel (solid black line) as a function of distance from Jupiter in R_J The dashed lines represent the 1σ, 2σ, and 3σ spread of the EPD log-normal fit.

Chapter 5

Analysis of the Galileo Near-Infrared Mapping Spectrometer

5.1 Instrument Overview

To demonstrate the technique with another instrument, we analyze the Galileo Near-Infrared Mapping Spectrometer (NIMS), which is an imaging spectrometer covering the spectral range 0.7 to 5.2 micrometers, overlapping with the SSI [23]. NIMS measures both reflected sunlight and emitted thermal radiation in a region not studied by the Pioneer and Voyager spacecraft. The spectral resolution is 0.0125 μm at wavelengths below 1 μm, and 0.0250 μm at wavelengths above 1 μm, yielding 204 spectral elements in nominal mode.

The instrument acquires spatial information by utilizing motions of the spacecraft scan platform, pushbroom imaging, and motions of a secondary mirror. The secondary mirror moves in a direction perpendicular to the mounting plate and sweeps out twenty pixels yielding an effective field of view of ten milliradians over the mirror sweep time (1/3 second). The instantaneous field of view is approximately 0.5 by 0.5 milliradians. Instrument cycle times vary from about 1/60 second to 8 and 2/3 seconds. The raw instrument data are organized using the spacecraft clock. With a knowledge of the start and stop time of a given observation, the data can be organized into a viewable object, normally known as a "cube", of stacked images with spatial coordinates on the front and spectral coordinates along the "back" axis.

A complete description of the NIMS instrument and scientific objectives is provided in Carlson et al. (1992) [23].

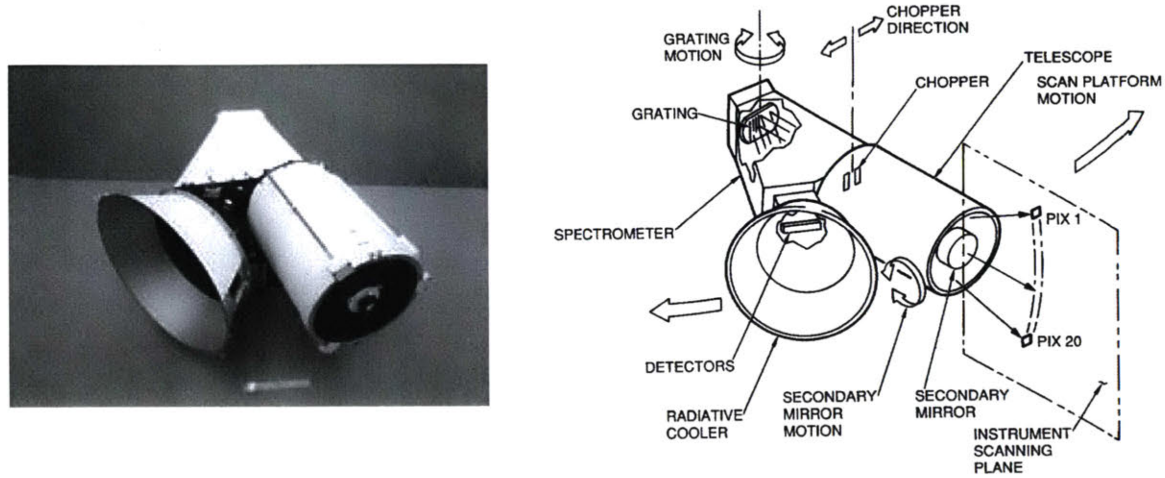

Figure 5-1: Photograph (left) and labeled diagram (right) of the NIMS instrument from Carlson et al. (2012) [23]. The telescope is on the right of each image, the radiative cooler is facing left of each image, and the spectrometer is in the background.

NIMS Detectors

NIMS consists of seventeen individual imaging elements (fifteen indium antimonide and two silicon pixels) arranged linearly along the plane of dispersion and illuminated by focused light from the grating. Each of the photodiode detectors has an active area of 0.2 mm by 0.2 mm. The spacing, material, wavelength, and detector number of each detector can be found in Figure 5-2. Sensor values are measured simultaneously in all detectors and are spaced approximately evenly across the wavelength region; a set of seventeen values is acquired at each of twenty cross-track positions (via a secondary scanning mirror) in a period of 1/3 second. There are four commandable gain ranges for all detectors except for detectors 15, 16, and 17, which have automatic gain ranging with two gains.

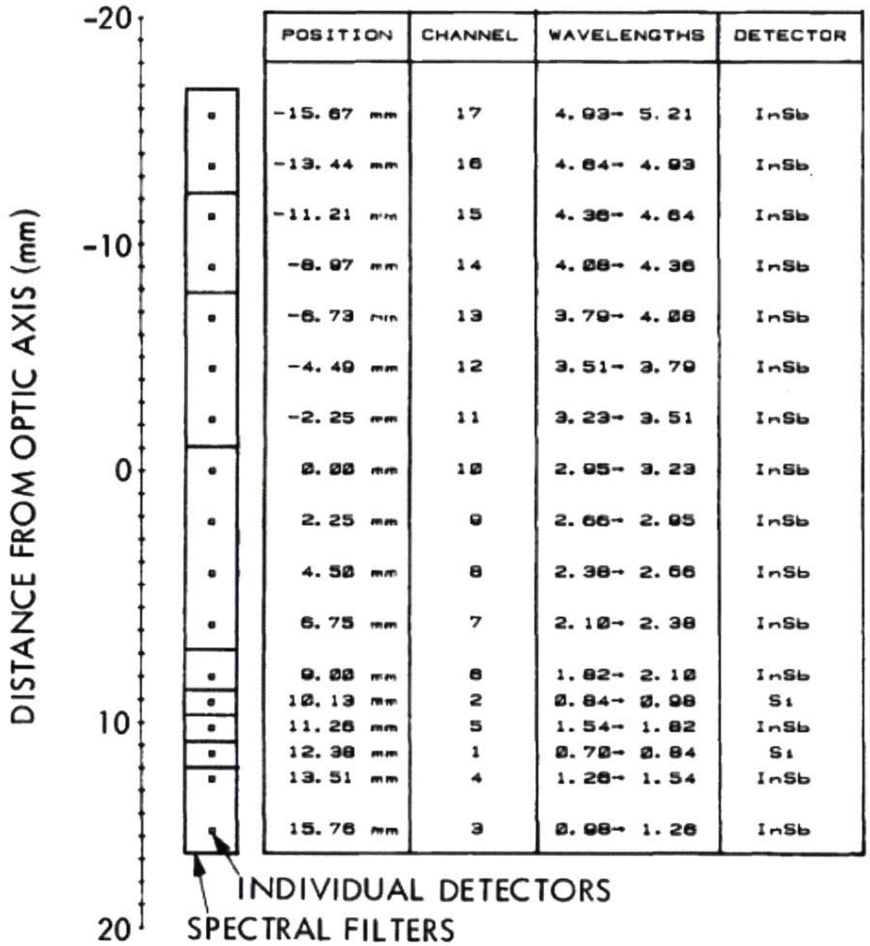

POSITION	CHANNEL	WAVELENGTHS	DETECTOR
-15.67 mm	17	4.93- 5.21	InSb
-13.44 mm	16	4.64- 4.93	InSb
-11.21 mm	15	4.36- 4.64	InSb
-8.97 mm	14	4.08- 4.36	InSb
-6.73 mm	13	3.79- 4.08	InSb
-4.49 mm	12	3.51- 3.79	InSb
-2.25 mm	11	3.23- 3.51	InSb
0.00 mm	10	2.95- 3.23	InSb
2.25 mm	9	2.66- 2.95	InSb
4.50 mm	8	2.38- 2.66	InSb
6.75 mm	7	2.10- 2.38	InSb
9.00 mm	6	1.82- 2.10	InSb
10.13 mm	2	0.84- 0.98	Si
11.26 mm	5	1.54- 1.82	InSb
12.38 mm	1	0.70- 0.84	Si
13.51 mm	4	1.26- 1.54	InSb
15.76 mm	3	0.98- 1.26	InSb

Figure 5-2: NIMS detector spacing along the optical axis, with the wavelength detection ranges and individual detector materials. The figure is from Table 2 of Bailey (1979) [7].

5.2 Particle Transport Simulations of Galileo NIMS

We model the Galileo NIMS instrument in SolidWorks to produce a CAD file. An annotated diagram of the modeled instrument can be found in Figure 5-3. Figure 5-4 shows the focal plane array, which contains the detectors and is modeled in greatest detail. The detectors can be seen through the sapphire window. Representative shielding from the spacecraft and SSI are also included but not pictured in the figures.

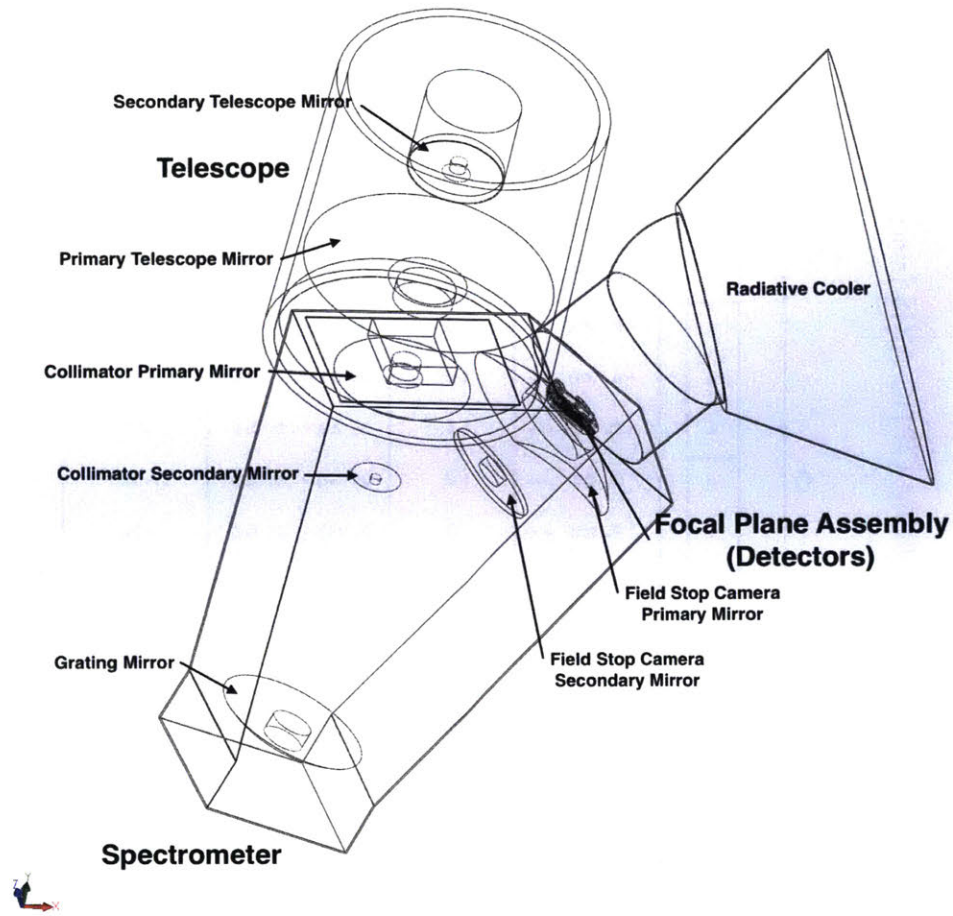

Figure 5-3: Annotated visualization of the NIMS CAD model. Shielding from the spacecraft and other instruments is not shown. CAD modeling assistance was provided by Tao Sevigny.

Figure 5-4: CAD model of the NIMS focal plane assembly. The seventeen detectors can be seen through the sapphire window. The outer shielding is roughly 5 mm of tantalum (shown in gray). CAD modeling assistance was provided by Tao Sevigny.

We perform mono-energetic electron simulations as described in Section 3.2.2. We simulate one billion electrons with the energies from 1 MeV to 100 MeV. For each energy, we record the number of unique primary and secondary particles that reach each detector and deposit energy and the number of detectors (effectively pixels) that are affected.

The mono-energetic simulations of <4 MeV electrons result in little or no energy deposited on the detector (fewer than 0.1% of pixels with hits). The simulation results are shown in Figure 5-5. For electrons below 5 MeV, over 90% of the intensity of the primary electrons are stopped, so we find that NIMS is capable of integral electron energy detection of ≥5 MeV. This threshold is consistent with findings from a FASTRAD ray tracing analysis in which we found a minimum equivalent aluminum shielding for each detector. The average minimum thickness is 8.22 mm of equivalent aluminum, which corresponds to a dose depth penetration of ~4 MeV electrons [29]. As an example, Figure 5-6 shows the least shielded paths to NIMS detector #16 from the FASTRAD analysis. Accounting for the pixel size of the individual detector elements (200 μm by 200 μm), for the scale factors, we find $K_1 = 0.93$ cm^2 electrons per detector and $K_2(E \geq 5\text{MeV}) = 0.0290$ sr. The combined scale factor is $0.0270\,\text{cm}^2\,\text{sr}$.

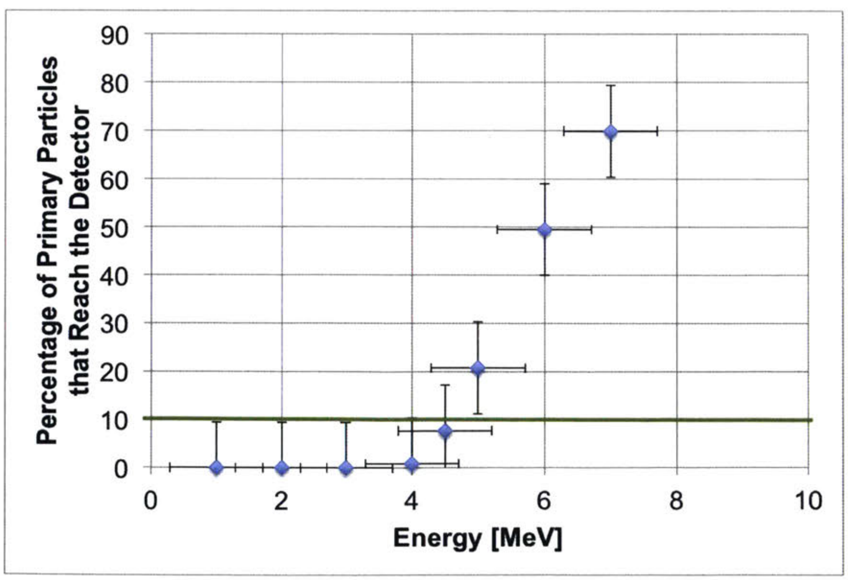

Figure 5-5: Percentage of primary particles that reach the NIMS detectors as a function of energy simulated in Geant4.

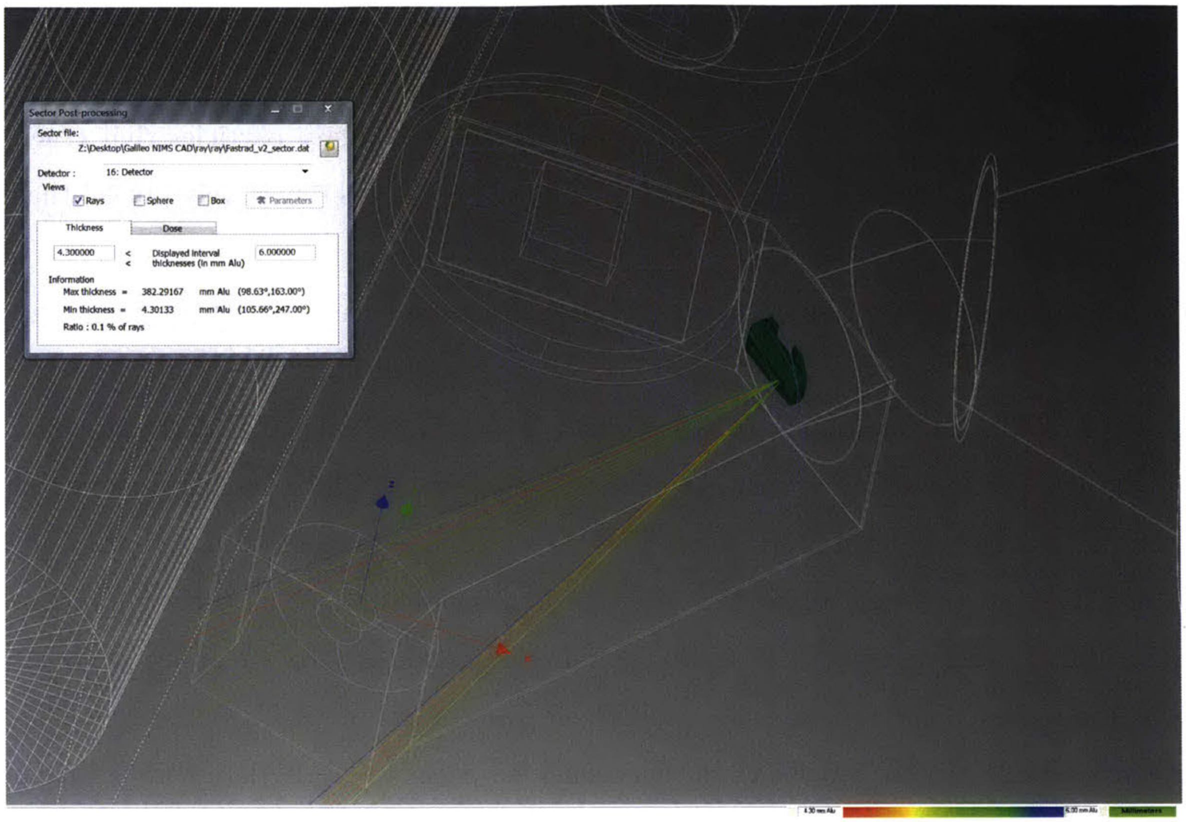

Figure 5-6: NIMS FASTRAD ray tracing results for an individual detector (#16).

5.3 NIMS Data Analysis

5.3.1 Data Collection and Image Processing

The raw instrument data is organized by spacecraft clock. A detailed description of the structure of the Experiment Data Record (EDR) may be found in the Galileo Software Interface Specification [68]. The data are recorded and stored with lossless compression and are fully recovered on the ground. Data can be found on the NASA PDS at: `ftp://pdsimage2.wr.usgs.gov/PDS_Archive/Galileo/NIMS`.

Two of the NIMS detectors are excluded from analysis. Detector 8, covering the 2.4-2.6 μm wavelength range, failed during the C3 encounter. Detector 3, covering the 1.0-1.26 μm range, failed during the E6 encounter. The data acquired after these failures are erratic and judged to be scientifically unusable [82]. Future work includes analyzing the available data from Detectors 8 and 3 from the first Galileo orbits.

5.3.2 Radiation Extraction with SPECFIX

Radiation hits (called "spikes" in the documentation) have been identified by the NIMS team using an algorithm called SPECFIX and removed them from the aggregated files [37]. SPECFIX identifies radiation hits from outliers relative to the mean of their nearest neighbors in a "brick" of a certain size that covers the temporal domain, the spatial domain (across adjacent detectors), and the spectral domain. Spikes are selected whose magnitude is large enough ($\geq$6 DN) to be distinguished from the instrument noise ($\sim$3 DN). The radiation hit information is saved (time stamp and value in DN of each hit for each detector) for observations near Europa, Ganymede, and Callisto. SPECFIX also subtracts the dark current files, though the darks were not taken regularly but are assumed to be invariant over a number of observations [82]. The SPECFIX approach is generally very effective, but can generate false positives at boundaries of data dropouts or for detectors at the edge (detectors 1 and 17) or next to a bad detector (detectors 3 and 8). This disqualifies detectors 2, 4, 7, and 9, leaving spikes identified from detectors 5, 6 and 10-16 as appropriate for this analysis. Spike files can be found with the rest of the raw Galileo NIMS data on the PDS.[1]

5.3.3 Analyzed Orbit Radiation Rate Data

We analyzed 40 observations from six orbits (G1, G2, C3, C4, E6, and G7). For each observation, we sum the spikes recorded for each detector. The spike counts are normalized by the exposure duration of the observation. Figure 5-7 shows the radiation rate for each detector. The rates are roughly grouped by the observation's distance from Jupiter: 13 observations at 9-11 R_J, 17 observations at 12-17 R_J, 2 observations at 18-20 R_J, and 8 observations at 23-29 R_J. It is clear from the figure that observations made closer to Jupiter have statistically significant higher radiation rates than those observations made farther away, as expected.

[1] For example, the spikes for Europa fly-bys can be found here: `ftp://pdsimage2.wr.usgs.gov/PDS_Archive/Galileo/NIMS/go_1006/europa/spike/`.

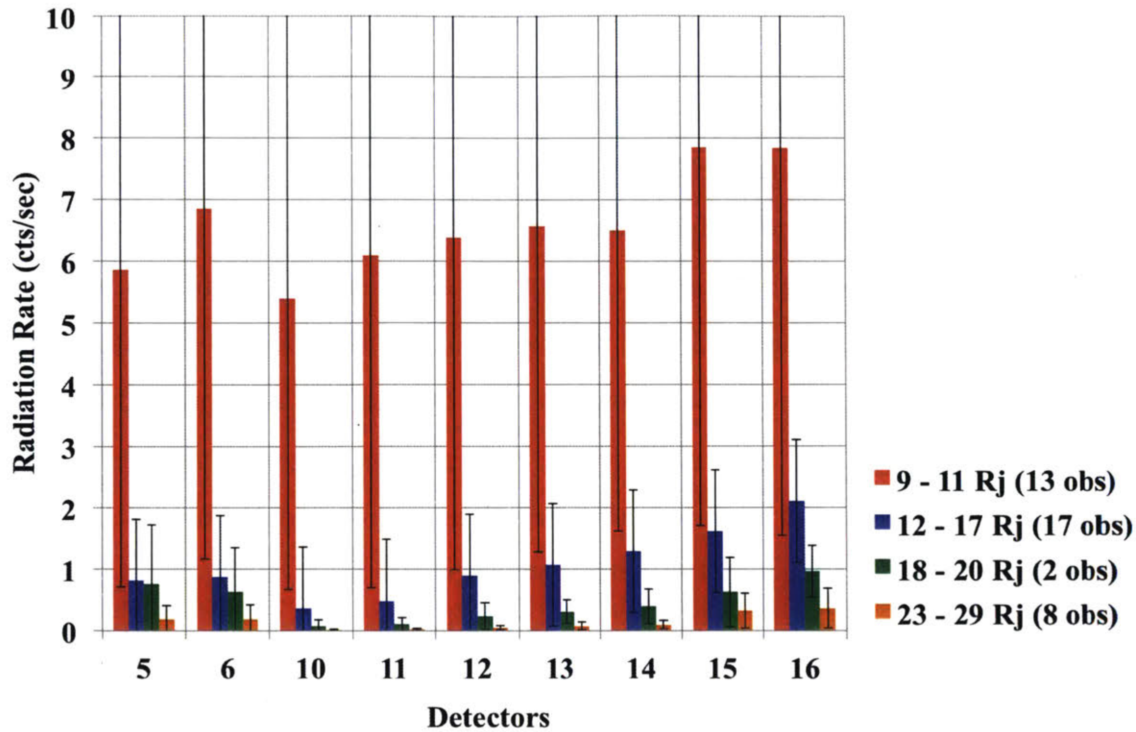

Figure 5-7: Radiation rates for each detector from 40 NIMS observations from six orbits. The radiation rates are binned by their relative distance from Jupiter.

In addition, the hit rate varies for each of the detector and seems to increase as a function of detector number from detector 10 to 16. Detector 10 is located near the center of the NIMS array and detector 16 is located close to the edge of the array. This is likely due to the asymmetrical shielding the instrument would receive from the configuration of the detectors (see Figure 5-2). The differential shielding is encouraging as it may be possible to extract multiple energy channels, which will be investigated in future work.

5.4 Comparison to Galileo EPD

Applying the scale factors to the NIMS radiation rates for each observation and detector, we calculate the $\geq$5 MeV integral flux. Figure 5-8 shows the integral flux for 40 NIMS observations compared to the two EPD integral flux channels that are closest to the determined NIMS sensitivity: DC2 and DC3, which measure the >2 and

>11 MeV electron fluxes, respectively. Each detector is pictured with a different color, showing the spread in the NIMS detection capabilities. The NIMS flux measurements lie between the two, as would be expected from a $\geq$5 MeV measurement. Detector #16 fluxes are higher in all cases than the detector #10 fluxes, reflecting the gradient in shielding from the outer edge of NIMS to the middle (more shielded) portion. The NIMS-calculated fluxes demonstrate that the method is generalizable to another type of imager. The results are interpreted in further detail in Chapter 6.

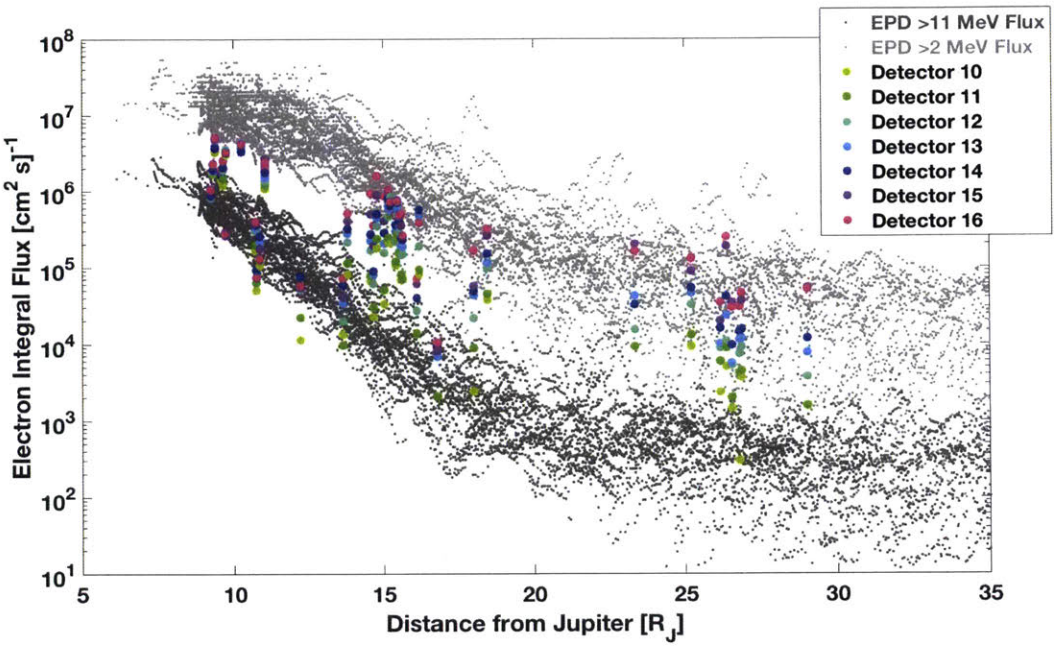

Figure 5-8: Calculated fluxes from NIMS observations for each detector compared to the Galileo EPD >11 MeV and >2 MeV integral electron flux

Chapter 6

Results

6.1 Limitations, Confidence, and Uncertainties

6.1.1 Systematic Uncertainties

We identify several sources of error and uncertainties that may affect the SSI data analysis. In general, we do not expect the final flux calculations to be significantly affected by these uncertainties. The gain state ratios are found to be relatively unchanged (<%1) from each calibration update to the original ground calibration [72, 73, 74]. However, the calibration was based on few calibration images. In-flight re-determination of the gain state ratios are correct within ±1% [74]. The gain state factors are harder to determine because they trade directly with operating temperature and efficiency. Over the mission lifetime, in-flight calibration found minimal changes in the mean pixel data (or digital) number (DN) [73, 74]. The changes are about 0.5 DN per pixel for gain states 1, 2, and 3, and about 1 DN per pixel for gain state 4.

Of the uncompressed images considered in the study of the SSI, we saw very few instances of saturated frames. In the cases where the image is >6 DN across the whole frame, we exclude the image from our analysis (see Section 4.3.3). Other factors to consider that are not included in this analysis are the thermal effects on quantum efficiency and calibration and instrument response to uncertainties.

Since it is challenging to quantify the systematic uncertainties described, the error bars on the SSI flux measurements are purely based on Poisson counting statistics. We assume a Poisson distribution because, considering radiation events over an interval of time, the events occur independently of the time since the last event. The 1σ error is $\pm\sqrt{N}$, where N is the number of pixels with radiation hits considered. Then, the upper and lower limits of the number of particles with radiation hits are used to compute the lower and upper 1σ bounds on the flux.

6.1.2 Limitations on the Radiation Extraction Procedure

It is possible that pixels are also affected by galactic (or anomalous) cosmic rays and from solar energetic particles. These heavier ions would require higher energies to penetrate through the spacecraft shielding and deposit energy. For a proton, the minimum energy would be roughly 100 MeV. The flux of galactic cosmic rays and protons at those energies are very low compared to the electron flux: <10 cm^{-2}-s^{-1} proton integral flux at >100 MeV at Europa [98]. Therefore, while there are some contributions to radiation hits misidentified as electrons, this number is marginal compared to electron-induced hits. This is typically not a concern for a dedicated particle detector due to complex coincidence detection schemes.

To assess how the radiation extraction method works compared to the literature, we compare the radiation average rates computed from Klaasen et al. (2003) to radiation rates computed using the technique developed in this thesis. Referring to Figure 6-1, we show agreement with the literature. There is a bigger discrepancy close to Jupiter, which we believe is due to the fact that Klaasen et al. (2003) take the first few lines of the image as the "background" and subtract the average of the background from the image to identify the hits. The number of pixels with hits are divided by the average exposure time, which means that if there are high-energy hits in the lines selected for the background, the radiation will be over-accounted for, especially when the flux is high.

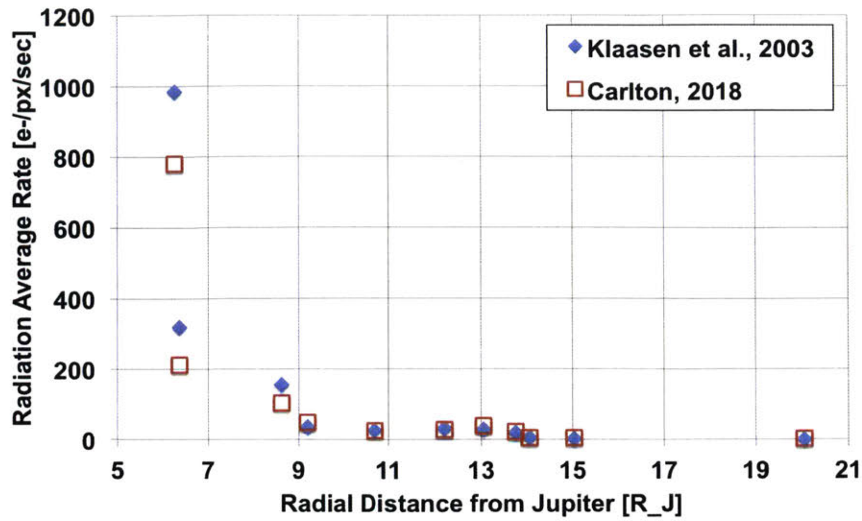

Figure 6-1: Comparison between the radiation rates calculated by Klaasen et al., 2003 and to the rates calculated with the method developed in this thesis.

6.1.3 Statistical Variations in the Geant4 Simulations

Since the Geant4 simulations are statistical in nature, we perform simulations of many billions of particles. The confidence intervals are provided for the scale factors in Table 4.2. For the confidence on the minimum threshold detection energy, the 95% confidence interval for $n = 5$ runs is calculated as follows: we find the average of the five runs (μ), compute the standard deviation (σ), the standard error (SE= $\sigma/\sqrt{5}$), and then the 95% confidence interval (C.I.=SE$\cdot$1.96). We find little deviation in the computed values over the five billion particles simulated for each energy. For $\geq$10 MeV, $K_1 = 2.636 \pm 0.013 \times 10^{-6}$ cm^2 and $K_2 = 0.5067 \pm 0.028$ sr.

Other particles from nuclear reactions such as positrons and gammas can also deposit energy, however their contribution is negligible compared to the electrons; for example, for a one billion 50 MeV electron simulation, 26,252 electrons, 4,236 positrons, and 37 gammas deposit energy. For a simulation of one billion 10 MeV particles, we find 1,043 particles that deposit energy in the detector, coming from 1,032 electrons, 10 positrons, and 1 gamma. These particles are all accounted for in the Geant4 simulation physics.

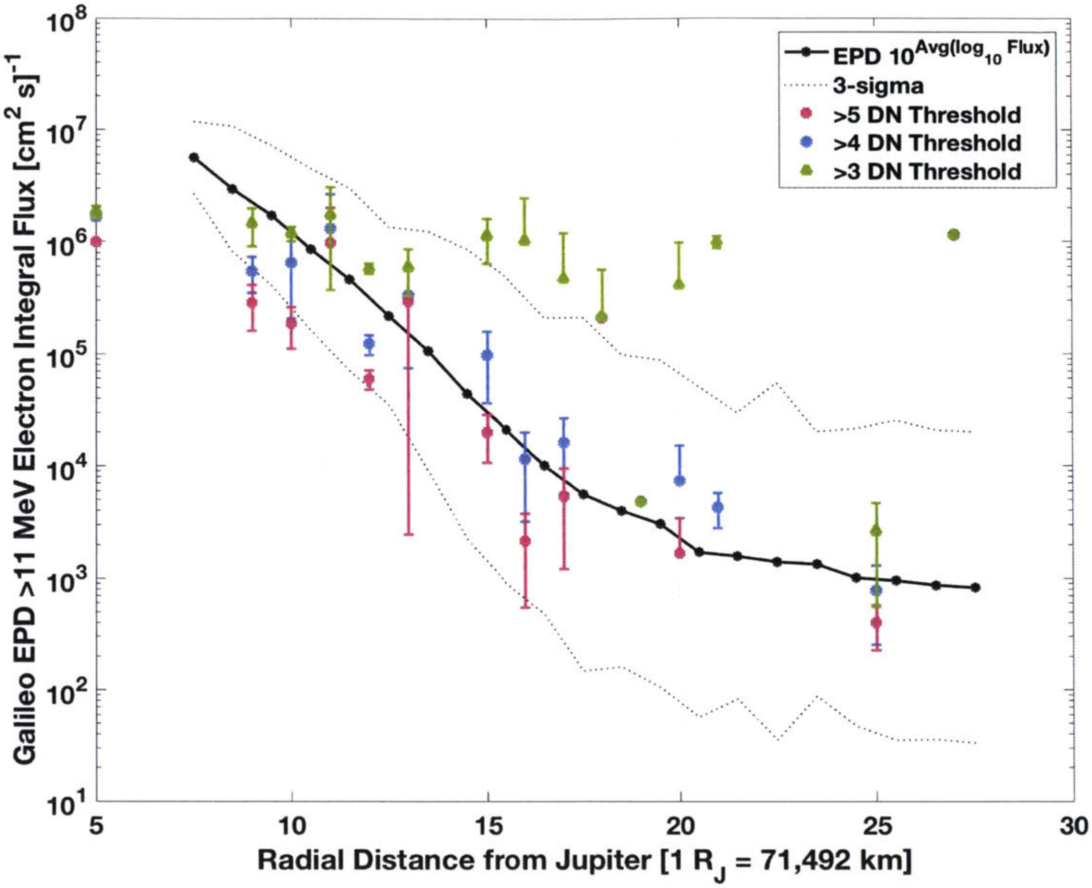

Figure 6-2: Comparison of the choice of SSI DN threshold for radiation detection. For radiation hits >5, >4 and, >3 DN, we calculate the fluxes and compare them to the EPD. The EPD 3σ is also shown in dashed lines.

6.2 Sensitivity Analysis

6.2.1 Sensitivity to Variations in DN

We assess how sensitive the fluxes calculated are to variations in the DN. For the SSI, we selected a threshold of >4 DN for pixels to be considered radiation hits over noise. In addition, there is a slight variation in the DN measured for a given calibration target, as discussed in Section 6.1.1. To assess the flux calculation sensitivity to the choice of DN, looking at Figure 6-2, we compare the fluxes from the SSI if the following DN thresholds are selected: >5 DN, >4 DN, and >3 DN. The plot shows the averages per orbit with the associated error bars. We see that the >4 DN threshold is the best fit to the EPD data. A threshold of >5 DN underestimates the radiation contribution slightly and a threshold of >3 DN overestimates the flux, particularly at greater radial distances from Jupiter. For the most part, the >5 DN threshold fluxes are still within 3σ of the EPD flux. This is consistent with the fact that we expect the high-energy radiation to deposit high amounts of energy, corresponding to high DNs. Therefore, we are confident about the conservative threshold choice in this work of >4 DN.

6.3 Results Compared to GIRE2

At the time of writing, the Jovian radiation model used by the community is the Galileo Interim Radiation Electron model version 2 (GIRE2) model (see a description in Section 1.3.2). Figure 6-3 shows the SSI fluxes plotted with the EPD >11 MeV and the GIRE2 >10 MeV integral electron fluxes. Figure 6-4 shows the EPD, GIRE2, SSI fluxes, and NIMS fluxes.

6.4 Comparison of Simulation Histograms

For each of the mono-energetic simulations, we build a histogram of the energy deposited in the detector. Figure 6-5 plots the histograms of energy deposited for simulations of the SSI instrument. We try to identify distinctive shapes of the mono-energetic histograms by fitting splines and Gaussians to the histograms. Then, the fitted curves would be used as a basis function and fit to the SSI energy histograms. In other words, for each energy, the multiplicative factor for the curve to match the SSI would translate to the flux for the given energy. However, even for ten billion particle runs in an effort to resolve the histogram shape, we find that the shapes of the histograms are similar, meaning that multiple energy channel extraction is not presently possible with the SSI instrument. Future work includes investigating multiple energy channel extraction with NIMS.

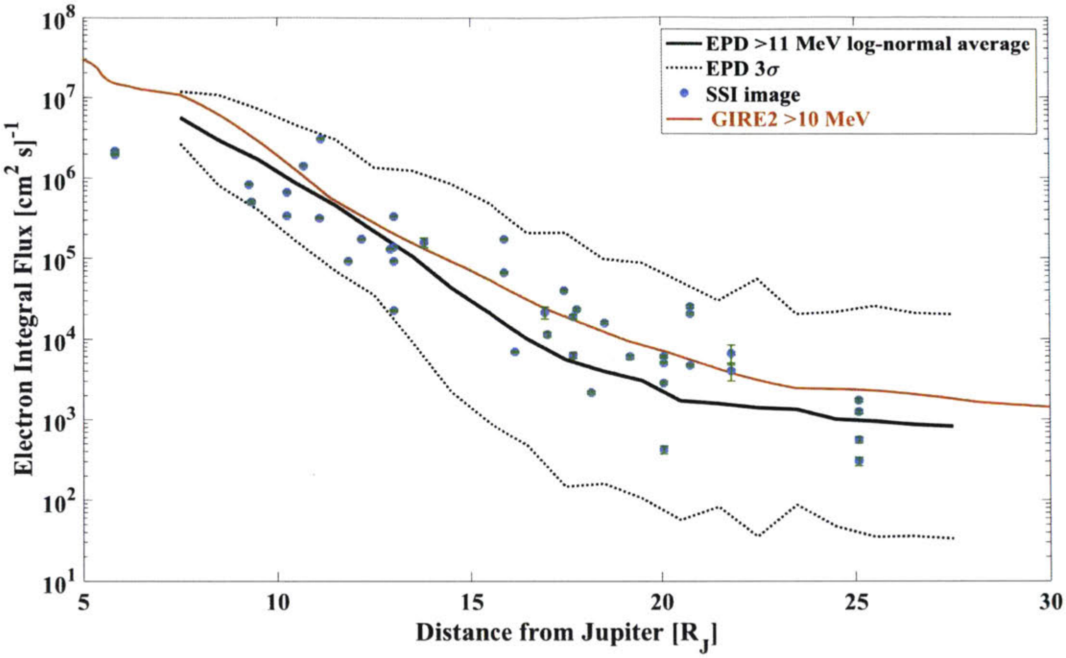

Figure 6-3: Comparison of the calculated SSI fluxes to the Galileo EPD >11 MeV and to the GIRE2 >10 MeV integral electron fluxes at the magnetic equator as a function of radial distance from Jupiter. The EPD 3σ is also shown in dashed lines.

We also looked into pulse shape discrimination techniques for distinguishing the curves. We looked into this by dividing the tails of the histogram curves by the total for each histogram curve. For the energies analyzed (5, 10, 30, 50, 100, 200 MeV), the curves are still not distinguishable from one another for the SSI. A challenge is to reduce the noise in the simulation histogram curves, without leaving the linear regime. If there are greater than 10% to 20% of pixels with hits, there are likely to be pixels with double hits, and it would be impossible to distinguish between two low energy particles in a pixel or a single higher energy particle.

Looking at Figure 6-5, the shapes of the energy deposition curves for 30 to 200 MeV are similar. In order to better understand why these curves look similar, we plot the energy deposited on the detector as a function of the kinetic energy of the particles at the detector (see Figure 6-6) and find the results are consistent with the stopping power of electrons in silicon. From ~1 to 80 keV, there is roughly a linear ratio between the energy at the detector and the energy deposited. This is because the majority of the lower energy particles are depositing all of their energy on the

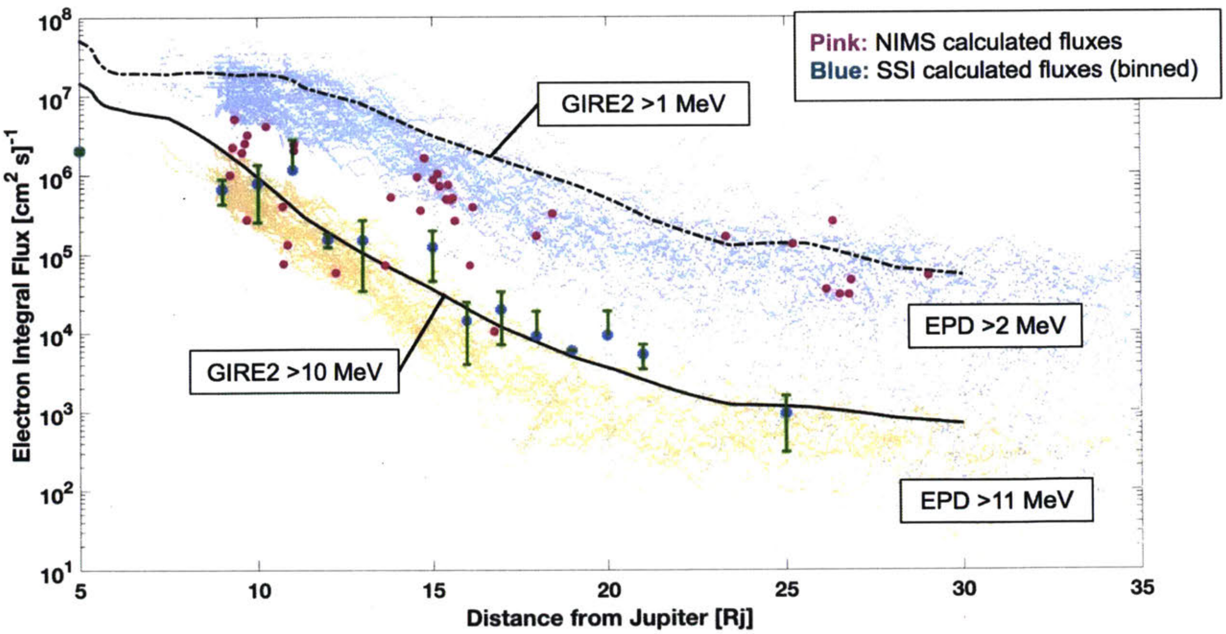

Figure 6-4: Comparison of the calculated SSI and NIMS fluxes to the Galileo EPD >11 MeV and >2 MeV and to the GIRE2 >10 and >1 MeV integral electron fluxes at the magnetic equator as a function of radial distance from Jupiter.

detector. For ≥100 keV, the incident energy does not affect the energy deposited on the detector. From ~10^{-1} to 10^{2} MeV, the stopping power is nearly flat, indicating approximately the same stopping power (MeV-cm^2/g). The continuous-slowing-down approximation (CSDA) range for 90 keV electrons is ~0.4734 g/cm^2 [86]. Dividing by the density of silicon (2.33 g/cm^3), that gives an approximate thickness of silicon of 20 µm, which is very close to the 15 µm thickness of the detector sensitive layer in the model, showing that the Geant4 model physics are self-consistent.

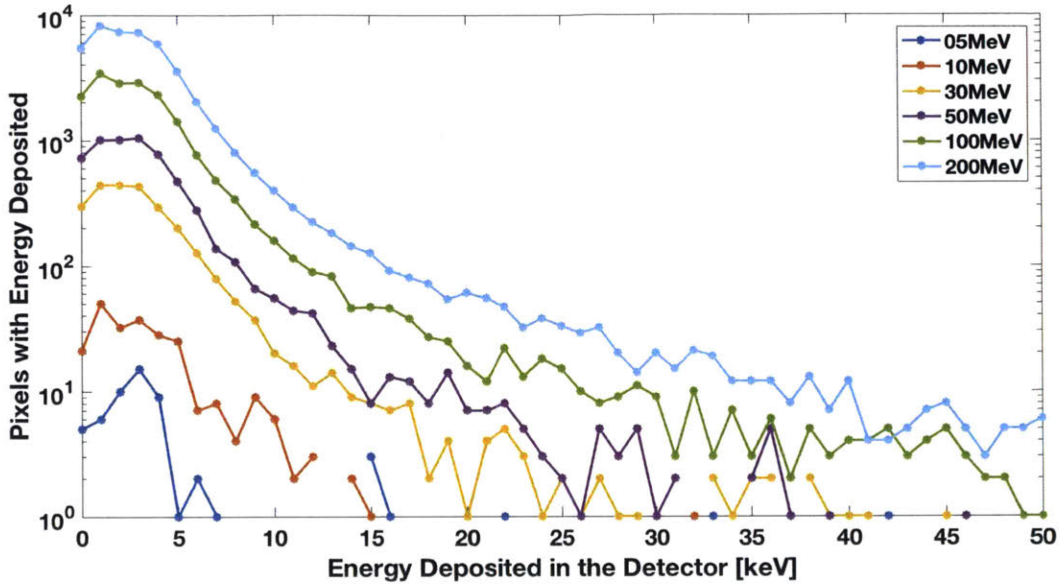

Figure 6-5: Histograms of the energy deposited from the Geant4 simulations of 5, 10, 30, 50, 100, and 200 MeV electrons. The histogram bin widths are 1 keV.

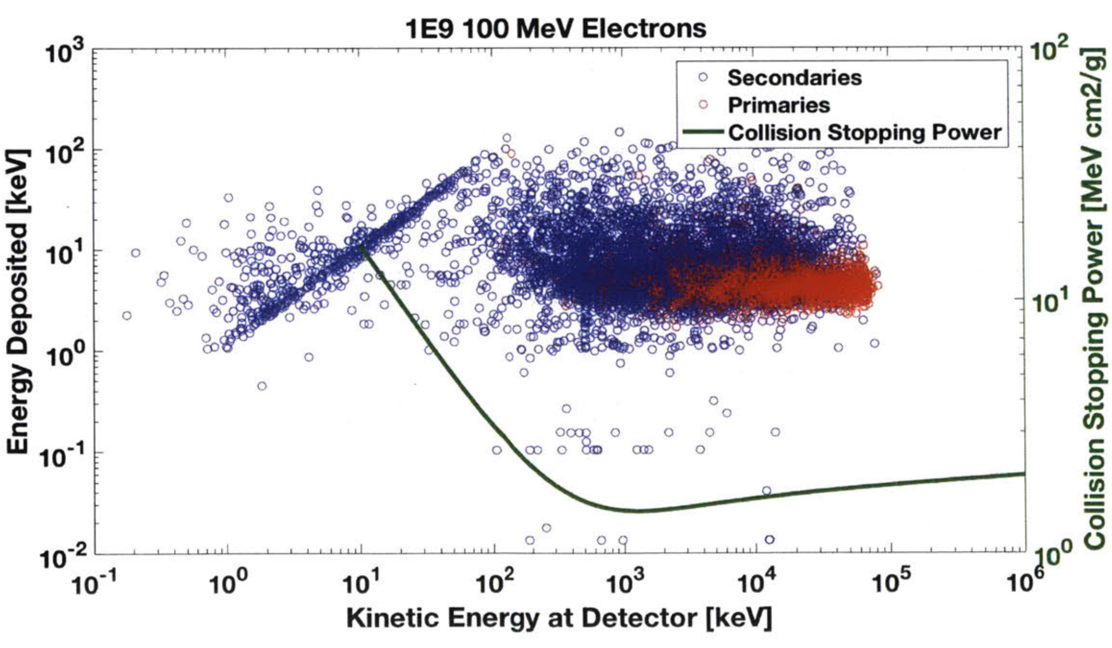

Figure 6-6: Energy deposited in the detector (left y-axis) as a function of the energy of the particle reaching the detector for 100 MeV electrons simulations of the SSI instrument. The primary particles are red circles and the secondaries are blue circles. The collision stopping power is plotted in green on the right y-axis.

Chapter 7

Conclusions

7.1 Jovian Applications

Juno, a mission already in orbit around Jupiter, and Europa Clipper, a mission planned for launch in the 2020s, both present opportunities for increased radiation environment knowledge using their imagers. This section identifies the instruments that could be used on each spacecraft, describes the datasets and information needed, and provides recommendations for calibration and operating procedures for the Europa Clipper mission.

7.1.1 Juno

While already in orbit around Jupiter, the Juno spacecraft carries several scientific and engineering instruments that are sensitive to and capable of measuring high-energy electrons. Figure 7-1 shows a diagram of the Juno spacecraft, pointing out its instruments. Becker et al. (2017b) show that the Stellar Reference Unit (SRU) and Advanced Stellar Compass (ASC) can be used to measure the >10 MeV electron flux and the Jupiter Infrared Auroral Mapper (JIRAM) can be used to measure the >5 MeV electron flux at Jupiter [11, 12]. The SRU and ASC are CCDs and JIRAM is an HgCdTe focal plane infrared imager. We have requested the imager data from the SRU and the ASC, as those products are not currently available through the PDS.

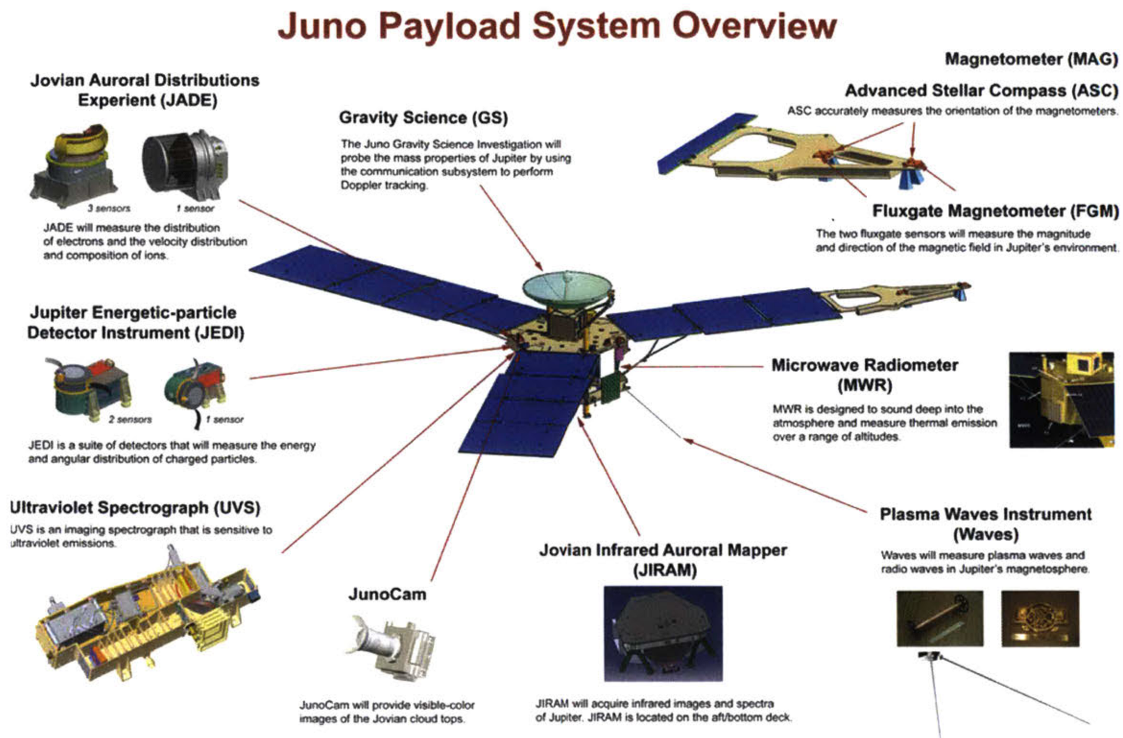

Figure 7-1: Diagram of the Juno payload system from NASA's Jet Propulsion Laboratory www.nasa.gov/.

As future work, we will compare the flux results using the method developed in this thesis to the results presented by Becker et al. (2017b).

Juno also has an ultraviolet spectrograph (UVS). It is a MCP analyzer, similar to the UV instrument used on New Horizons by Steffl et al. (2012) [106] to measure MeV electrons. Further information on the Juno UVS can be found in Gladstone et al. (2017) [48]. The UVS system primarily operates at perijove ($\sim$3 hours) and at apojove (1-2 days). We would suggest operation at intermediate locations during the orbit since the orbital period is $\sim$53 days.

JunoCam, which is a wide-angle visible spectrum camera imaging the cloud tops of Jupiter, is hosted primarily for the purposes of education and public outreach [53, 83]. The detector is a 1640 x 1214, 7.4-micron pixel array. Typically, the instrument is used a few hours on either side of perijove, and then remains off through the remainder of the orbit. The instrument was only predicted to survive radiation through the first three months on orbit, but is still collecting data at the time of writing [53, 83]. Monitoring the degradation of the system will provide valuable information on the performance of these types of systems in extreme radiation environments. The JunoCam system has the operational ability to take non-compressed frames and can take dark fields (though data volume return is a challenge). There is an on-board median filtering system that can be used to correct the electron radiation damage, but it is not used for all observations. It is also worth noting that there is an engineering model of the instrument that could be used for calibration using radiation testing.

7.1.2 Europa Clipper

The planned Europa Clipper mission has several instruments that are sensitive to and capable of measuring MeV radiation (shown in Figure 7-2 with green boxes). Each of the four science instruments discussed can measure rough integral flux and some may provide differential flux and energy spectra. The measured electron energy sensitivity threshold should be determined using instrument shielding. Beam tests and transport simulations should be performed before Jupiter orbit insertion to calibrate the instrument response to radiation and to compute the scale factors required to calculate the flux. The next paragraphs go into detail for the instruments describing the current (planned) radiation-related efforts and additional efforts that are needed to implement this technique and those that are recommended to increase the fidelity, quantity, or coverage of the radiation data.

The ultraviolet spectrometer (Europa-UVS) is a MCP detector, which is sensitive to radiation. There is a UV-blocking coating around the edge of the MCP which allows for UV and radiation measurements to be made simultaneously [95]. Initial simulations by the UVS team indicate that the MCP is sensitive to $>$15 MeV electrons. UVS will incorporate a dosimeter that will provide absolute TID rate. The MCP was tested in a $<$3 MeV electron beam. UVS radiation data will be part of the housekeeping telemetry. Some of the challenges involve the use of this instrument in high radiation environments due to concerns about damage. We recommend beam-line tests of the full instrument to enable verification of transport simulations and the characterization of the instrument response to secondary particles generated in the

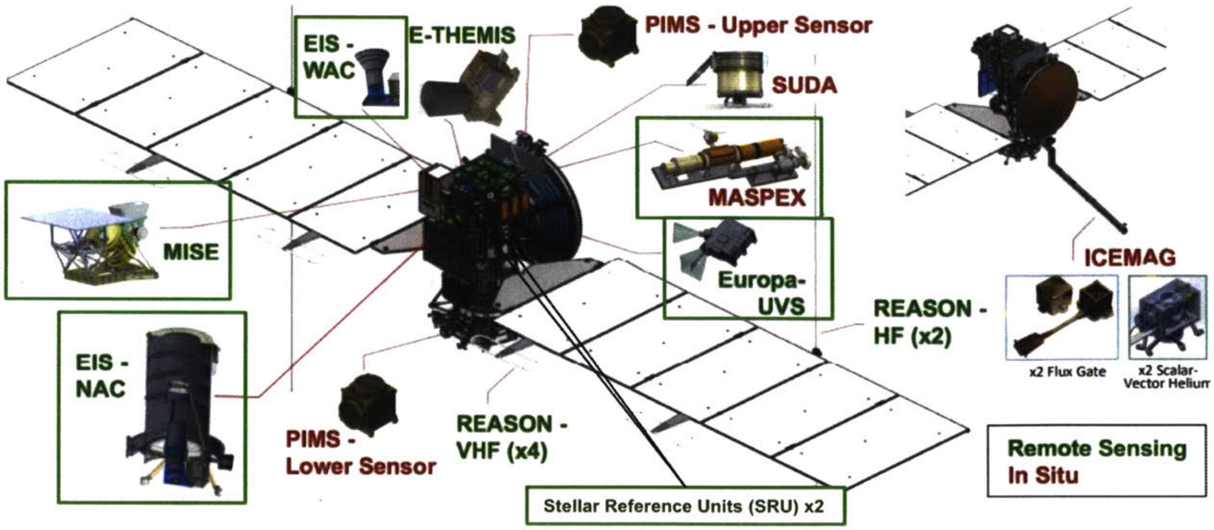

Figure 7-2: Diagram of the Europa Clipper instruments. Instruments that can be used for electron detection are in green boxes.

shielding.

The Mapping Imaging Spectrometer for Europa (MISE) is a near-infrared mapping spectrometer that will examine the surface composition of Europa [14]. Radiation noise on the detector can be used to characterize the energy deposited from energetic particles. At the present, on-board processing distinguishes infrared photons from electrons. The instrument will only operate near Europa (due to high power draw due to cooling needs), so it provides a complementary dataset to that of the UVS. Presently, the MISE team has performed transport simulations that were calibrated with beam-line tests of the full instrument. The team is developing an on-board algorithm capable of identifying radiation hits. To implement the technique in this thesis, we need 1D histograms (# pixels vs DN) of radiation hits from at least one image cube per region. This information can come from running the on-board algorithm (will require additional power) or downlinking raw data and post-processing it on the ground (will require additional data rate allocation). For MISE, we see several additional efforts that would increase the fidelity and radiation return. We recommend occassionally downlinking of a full image cube (map of radiation hits on the detector, $\sim$4.7 MB/map) to validate calibration. Current data processing can only provide estimates of approximately >10 MeV electrons. We suggest further communications with the MISE team to support the development of a technique capable of obtaining electron energy spectra from radiation noise data.

The Europa Imaging System (EIS) consists of a visible-spectrum wide and narrow angle camera instrument using CMOS detectors [109]. EIS will take dark frames for calibration, which are preferred to images for the radiation investigation since they contain radiation hits only. Currently, there are no radiation-related efforts other than the radiation hardness testing required by the Europa Clipper Project for EIS. Radiation transport simulations of the full instrument are needed to evaluate the radiation noise response that would allow us to measure the integral flux of MeV electrons. We also need downlinked radiation hit information for each frame, which can be obtained from on-board processing or raw data downlink processing on the ground. As for additional efforts, we recommend taking dark frames more often (at least once per orbit) to increase the amount of data available for the radiation investigation. We recommend proton and electron beam-line tests of the full instrument to calibrate and validate the transport simulations.

The Mass Spectrometer for Planetary Exploration (MASPEX) is a high-sensitivity, time-of-flight, mass spectrometer that will analyze the surface and subsurface of Europa by measuring the atmosphere and surface materials ejected [17]. MASPEX uses a MCP detector. Radiation monitoring requires MCP under high voltage, while ions are flying in the instrument and during warming-up. The MCP should not operate in the highest radiation zones to avoid degradation. The MASPEX team has performed modeling to estimate the required shielding thickness. Preliminary analysis of these simulations shows that the detector will be most sensitive to approximately >3 MeV electrons. Background radiation data will be part of the housekeeping telemetry, but will only exist while the instrument is on. We recommend beam-line tests to calibrate and validate radiation transport models. If radiation levels allow, we would also like to keep the MCP running to acquire radiation data whenever possible.

From the Europa engineering systems, Europa Clipper plans to have star trackers, which need calibration using transport models and beam-line tests (similar to MISE and EIS efforts). Recently, a Radiation Monitoring System (RMS) has been proposed.

It will include two to three charge monitors that will measure integral electron current. The lowest energy depends on the selected shielding, probably 0.2-3 MeV. The RMS will also include TID sensors for measuring the dose rate. Geant4 simulations are in progress and beam-line tests are planned.

7.1.3 Suggestion for dosimeters and SEU monitors

We suggest that future missions to Jupiter include dosimeters, which are light in resources (low mass, small size, and data rates are typically on the order of a few kBits per day or less). They are low in cost in general and can be simple, inexpensive pFETs (much like thermistors). We propose including dosimeters at selected locations in the radiation vault for instrument electronics, at locations of concern outside the vault, and co-located with solar arrays, if applicable. The primary value of dosimeters is that they measure the actual dose at a location and monitor it continuously, as opposed to particle detectors, which in the case of Juno and Galileo, do not typically cover the entire energy ranges of interest and do not provide continuous data. Actual dose is required to estimate effects on some components. Other components that could be included are transient pulse monitors or dedicated internal electrostatic discharge (IESD) monitors.

7.2 Earth Applications

This technique can be applied to instruments on spacecraft outside the Jovian radiation environment as well. Solid-state detectors are common on exploratory and science-based missions, as well as included as engineering instruments, such as in star trackers and LIght Detection And Ranging (LIDAR) sensors. At Earth, trapped electrons have a dual peak in intensity as a function of distance from Earth, comprising the Van Allen radiation belts. Figure 7-3 shows the integral electron flux as a function of energy and radial distance from Earth. The inner radiation belt, containing protons and electrons, can be found at L-shell values of ∼1-3 and the outer radiation belt, dominated by electrons, can be found at L-shell values around ∼4-6. The

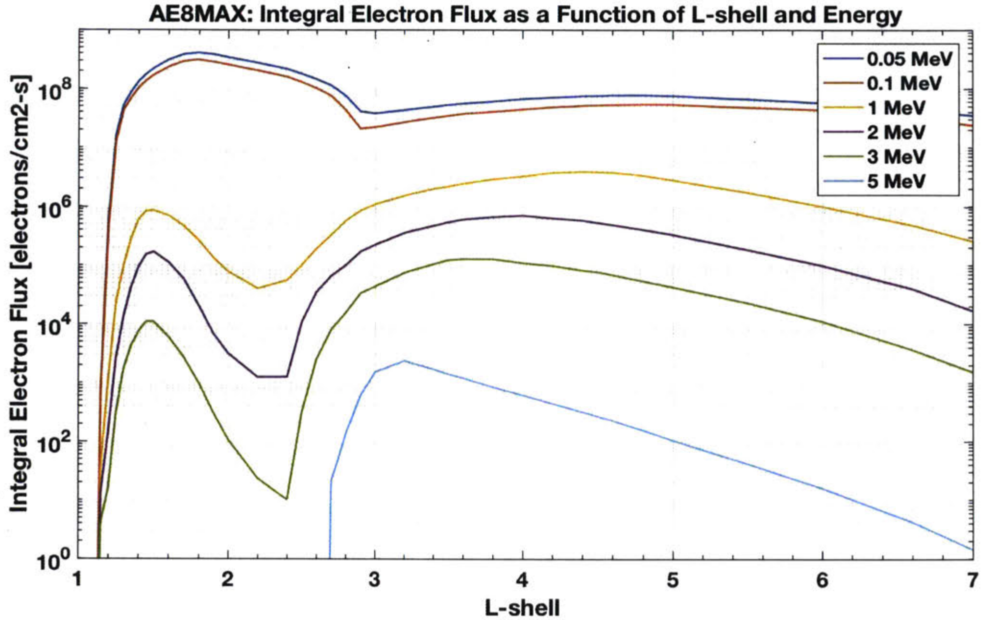

Figure 7-3: Integral electron flux at Earth as a function of L-shell and energy. Data are from the AE-8 trapped radiation model at solar maximum [112].

location and intensity of the electron belts is variable, especially in the outer belt; the locations are heavily dependent on geomagnetic storms. See Reeves et al. (2013, 2015) for details on recent observations from the Van Allen Probes satellites on belt variability [93, 94]. We also note that radiation in space may also originate from man-made sources, such as the 1962 Starfish Prime detonation, which generated a temporary artificial radiation belt, crippling or disabling at least six satellites [19, 55]. As such, spacecraft at Earth would derive great benefit from real-time knowledge of the belts for operational considerations and anomaly mitigation and resolution.

Several critical satellite constellations orbit at the inner edge of the outer electron belt. The Global Navigation Satellite System (GLONASS) and Global Positioning System (GPS) are space-based satellite navigation systems used extensively for both military and civilian applications. GLONASS, supported by the Russian Space Agency, consists of 24 satellites in three circular orbit planes at an altitude of 19,130 km ($\sim$3 R_E) with a 64.8 degree inclination. GPS, operated by the United States Air Force, consists of 31 satellites in circular orbits at six circular orbit planes at an altitude of 20,180 km ($\sim$3.2 R_E) with approximately a 55 degree inclination. As part

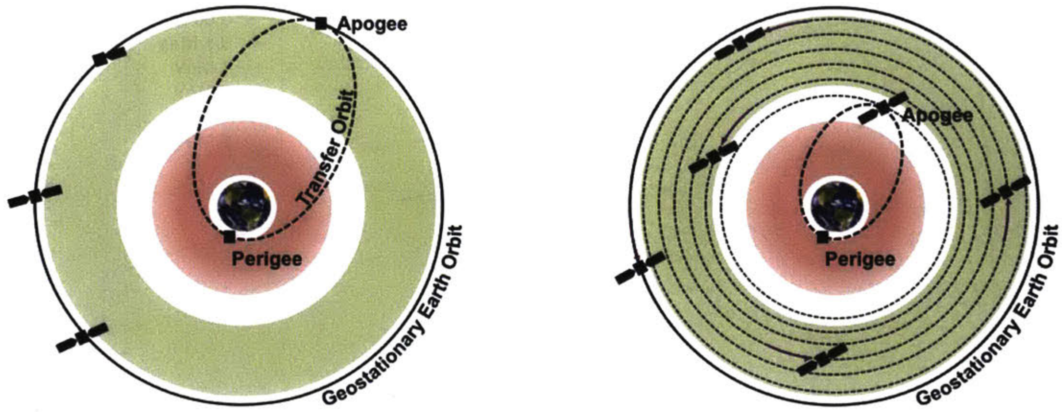

Figure 7-4: Comparison of traditional (chemical) and electric propulsion orbit trajectories to GEO, on the left and right, respectively. The red shading represents the inner Earth radiation belt, which is dominated by protons. The green shading represents the outer Earth radiation belt, which is dominated by electrons.

of the attitude determination and control systems for these spacecraft, Earth-horizon and Sun sensors are typically included [9]. These sensors require photodetectors, which could be used to collect additional information about their local electron environment. In addition, the sensors are often placed on the three axes of the spacecraft, providing the opportunity to investigate the directionality of the electrons with respect to the spacecraft and Earth.

Geostationary Earth orbit (GEO) communications satellites (ComSats), located at 6.6 R_E, are critical assets to communications, navigation, science, and defense industries worldwide. GEO ComSats make up over 50% of the satellites on orbit (with >600 ComSats reported on orbit in 2014), totaling over \$203B in revenue in 2014 [99]. The revenue is not in hardware sales, but in the services they provide. In addition, the increasing demand for and dependence on satellite services has driven technological evolution of spacecraft components to be smaller, more power efficient, and more capable, using smaller feature-size electronics. However, the smaller electronics are more complex and often more susceptible to radiation damage [78]. Additionally, recent developments in electric propulsion are starting to be used to boost GEO satellites to their final orbits. Electric propulsion is power-efficient, but comes at the cost of increased time to orbit (on the order of months), spiraling slowly to raise the orbit altitude, meaning more time in the electron belts [21]. Figure 7-4 shows the comparison of the path to orbit for chemical and electric propulsion. GEO ComSats often include imagers that could be used to inform decision-making algorithms on-board of potential hazards. Earth-horizon sensors, Sun sensors, and star trackers are common, which could be exploited using the technique developed in this thesis.

7.3 Future Work and Long-Term Applications

We plan to investigate the differential shielding of the NIMS instrument with the goal of extracting more than one integral energy channel. Initial analysis shows that the detectors near the outer edge of the focal plane array (Detectors 14-16) have less shielding and, empirically, have a higher radiation count rate than the detectors closer to the center of the focal plane array (Detectors 10-12) (see Figure 5-7). This implies that the edge detectors are likely sensitive to a lower minimum (threshold) energy. To determine this, we will perform additional Geant4 runs to calculate the scale factors and to determine the threshold energies for each of the NIMS detectors.

Future work includes the demonstration of this technique using an Earth-orbit spacecraft. The Geostationary Operational Environmental Satellite system, consisting of three spacecraft in GEO, presents a testbed that could be used for this demonstration. For the series of GOES satellites in orbit now, there are several imagers that can be evaluated: the Solar Ultraviolet Imager (SUVI), the Geostationary Lightning Mapper (GLM), and the Extreme Ultraviolet Sensor (EUVS) [85]. SUVI and GLM use CCDs for detection. EUVS has covered pixels for background measurements. To validate the technique, we would compare the calculated fluxes to the high-energy particle detector on GOES, the Space Environmental In Situ Suite (SEISS). The GEO belt sits on the outer edge of the electron Van Allen belt, but also experiences high-energy protons, especially during solar energetic particle events. As such, a key consideration would be the identification and removal of the proton events. There are several sources in the literature for identifying protons on imagers (see Section 2.3).

Future work also includes expanding the algorithms for use on-board and in near-real time. The high-energy flux information provided could feed into autonomous fault diagnosis and anomaly resolution. We also plan to look at how the technique can be modified for other types of imagers, especially for high-contrast imaging and other photon-counting detectors.

7.4 Summary of Research Contributions

This thesis presents a novel approach to high-energy electron detection using science imagers on spacecraft. The method combines particle transport simulations using detailed mechanical models of imaging cameras with experimental image analyses to obtain particle energy measurements. We demonstrate the technique using Galileo SSI images, in which we created a process for extracting electron radiation hits in an imager. We find that the SSI is capable of detecting $\geq$10 MeV electrons. Using geometric scaling factors computed for the SSI, we calculate the environment particle flux given a number of pixels with radiation hits. We compare the SSI results to measurements from the Galileo EPD, examining the electron fluxes from the $>$11 MeV integral flux channel. We find agreement with the EPD data within 3-sigma of the EPD log-normal average fit for 43 out of 43 (100%) of the SSI images evaluated. 62% of fluxes are also within 1-sigma of the EPD data. We validated the generalized procedure by analyzing a second imager, Galileo NIMS. We find that NIMS is sensitive to $\geq$5 MeV electrons and the calculated fluxes are consistent with the EPD. In addition, we have created guidelines for pre-flight testing and calibration, as well as in-flight operational procedures to use an imaging instrument for energetic particle measurements, including specific recommendations for the Juno and Europa Clipper missions.

Appendix A

Explanation of the 4π Isotropic Flux vs. the 2π Incident Current

In order to simulate an isotropic space environment in a radiation transport code, a cosine-law should be selected as a source angular distribution. This is because the uniform, isotropic distribution on a surface produces a cosine distribution, which is defined as a distribution that the equal number of particles is coming in per unit "solid angle," corresponding to a cosine-distribution.

We have simulated a spherical shell of electrons radiating inwards with a cosine angular distribution. But, in the real space environment, particles are everywhere and in every direction. The 4π isotropic distribution and the 2π cosine angular distribution are related by a factor of four, the derivation of which will be shown here.

In spherical coordinates, the surface element spanning from θ to $\theta + \mathrm{d}\theta$ and φ to $\varphi + \mathrm{d}\varphi$ on a spherical surface at (constant) radius r is: $\mathrm{d}S_r = r^2 \sin\theta \mathrm{d}\theta \mathrm{d}\varphi$. Thus, the differential solid angle is: $\mathrm{d}\Omega = \frac{\mathrm{d}S_r}{r^2} = \sin\theta \mathrm{d}\theta \mathrm{d}\varphi$. Figure A-1 shows a simple diagram of the variables.

Let $\phi(E, \theta)$ be the incident flux, which is a function of energy E and solid angle θ, which has units of $\#/\mathrm{cm}^2$-s-sr-MeV.

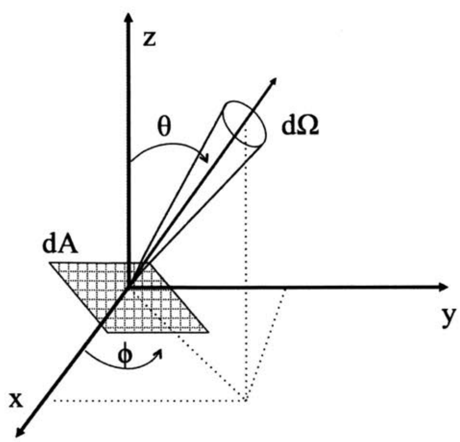

Figure A-1: Diagram of the solid angle and area for a generalized flux calculation.

4π Isotropic Flux. Assuming isotropic, $\phi(E,\theta) = \phi(E)$, the 4π isotropic flux becomes:

$$\begin{aligned}\Phi_{4\pi} &= \int_{\varphi=0}^{2\pi}\int_{\theta=0}^{\pi} \sin(\theta)\phi(E)\mathrm{d}\theta\mathrm{d}\varphi = \int_{\varphi=0}^{2\pi}\mathrm{d}\varphi\int_{\theta=0}^{\pi}\sin(\theta)\phi(E)\mathrm{d}\theta \\ &= 2\pi\int_{\theta=0}^{\pi}\sin(\theta)\phi(E)\mathrm{d}\theta = 2\pi\phi(E)\int_{\theta=0}^{\pi}\sin(\theta)\mathrm{d}\theta \\ &= 4\pi\phi(E) \qquad \text{(A.1)}\end{aligned}$$

2π Incident Current. The flux pertains to the number of particles crossing through a unit area perpendicular to the incident particle velocity vector. The current of particles crossing into the medium, per unit area of the plane boundary, is then

$$j(E,\theta) = \phi(E,\theta)\cos(\theta) \qquad \text{(A.2)}$$

for $0 \leq \theta \leq \pi/2$ where θ is the angle of incident with respect to the normal to the plane. The current j has the same units as the flux ϕ. The 2π total incident current from the spherical shell can be written as:

$$\begin{aligned}J_{2\pi} &= \int_{\varphi=0}^{2\pi}\int_{\theta=0}^{\pi/2} j(E)\sin(\theta)d\theta d\varphi = \int_{\varphi=0}^{2\pi}d\varphi\int_{\theta=0}^{\pi/2}j(E)\sin(\theta)d\theta \\ &= 2\pi\phi(E)\int_{0}^{\pi/2}\sin(\theta)\cos(\theta)d\theta\end{aligned}$$

Using u-substitution, letting $u = \sin(x)$,

$$\begin{aligned} J_{2\pi} &= 2\pi\phi(E)\frac{\sin^2(\theta)}{2}\Big]_0^{\pi/2} = 2\pi\phi(E)\big(\frac{1}{2}\big) \\ &= \pi\phi(E) \end{aligned} \tag{A.3}$$

From Eqns. A.1 and A.3, the 4π isotropic flux and the 2π incident current can be related as

$$\Phi_{4\pi} = 4J_{2\pi}, \text{ or} J_{2\pi} = \frac{\Phi_{4\pi}}{4} \tag{A.4}$$

Equation A.4 implies that simulating one cosine-law source particle in the 2π space is four times over-sampling of the isotropic environment in the 4π space. Therefore, the results obtained using cosine-law source distribution should be divided by four to get the corresponding results for isotropic source environment. This factor of four is accounted for in the geometric factors.

Appendix B

Geant4 Physics List

Physics definition uses in the Geant4 simulations:

```
//
// ********************************************************************
// * DISCLAIMER                                                       *
// *                                                                  *
// * The following disclaimer summarizes all the specific disclaimers *
// * of contributors to this software. The specific disclaimers,which *
// * govern, are listed with their locations in:                      *
// *   http://cern.ch/geant4/license                                  *
// *                                                                  *
// * Neither the authors of this software system, nor their employing *
// * institutes,nor the agencies providing financial support for this *
// * work  make  any representation or  warranty, express or implied, *
// * regarding  this  software system or assume any liability for its *
// * use.                                                             *
// *                                                                  *
// * This  code  implementation is the  intellectual property  of the *
// * GEANT4 collaboration.                                            *
// * By copying,  distributing  or modifying the Program (or any work *
// * based  on  the Program)  you indicate  your  acceptance of  this *
// * statement, and all its terms.                                    *
// ********************************************************************
//
//
// $Id: BeamTestPhysicsList.cc,v 1.18 2004/03/19 14:58:21 maire Exp $
// GEANT4 tag $Name: geant4-07-01-ref-02 $
//
//
```

```
//....oooOOOOOooo........oooOOOOOooo........oooOOOOOooo........oooOOOOOooo......
//....oooOOOOOooo........oooOOOOOooo........oooOOOOOooo........oooOOOOOooo......
#include "globals.hh"
#include "BeamTestPhysicsList.hh"

#include "G4ProcessManager.hh"
#include "G4ParticleTypes.hh"
#include "G4SystemOfUnits.hh"
#include "G4IonConstructor.hh"
//....oooOOOOOooo........oooOOOOOooo........oooOOOOOooo........oooOOOOOooo......

BeamTestPhysicsList::BeamTestPhysicsList():  G4VUserPhysicsList()
{
 defaultCutValue = 0.001*mm;
 SetVerboseLevel(1);
}

//....oooOOOOOooo........oooOOOOOooo........oooOOOOOooo........oooOOOOOooo......

BeamTestPhysicsList::~BeamTestPhysicsList()
{;}

//....oooOOOOOooo........oooOOOOOooo........oooOOOOOooo........oooOOOOOooo......


void BeamTestPhysicsList::ConstructParticle()
{
  ConstructBosons();
  ConstructLeptons();
  ConstructMesons();
  ConstructBaryons();
  G4IonConstructor pIonConstructor;
  pIonConstructor.ConstructParticle();

}

void BeamTestPhysicsList::ConstructBosons()
{
  // pseudo-particles
  G4Geantino::GeantinoDefinition();
  G4ChargedGeantino::ChargedGeantinoDefinition();

  // gamma
  G4Gamma::GammaDefinition();
}
```

```
//....oooOOOOOooo........oooOOOOOooo........oooOOOOOooo........oooOOOOOooo......

void BeamTestPhysicsList::ConstructLeptons()
{
  // leptons
  //  e+/-
  G4Electron::ElectronDefinition();
  G4Positron::PositronDefinition();
  // mu+/-
  G4MuonPlus::MuonPlusDefinition();
  G4MuonMinus::MuonMinusDefinition();
  // nu_e
  G4NeutrinoE::NeutrinoEDefinition();
  G4AntiNeutrinoE::AntiNeutrinoEDefinition();
  // nu_mu
  G4NeutrinoMu::NeutrinoMuDefinition();
  G4AntiNeutrinoMu::AntiNeutrinoMuDefinition();
}

//....oooOOOOOooo........oooOOOOOooo........oooOOOOOooo........oooOOOOOooo......

void BeamTestPhysicsList::ConstructMesons()
{
  //  mesons
  //    light mesons
  G4PionPlus::PionPlusDefinition();
  G4PionMinus::PionMinusDefinition();
  G4PionZero::PionZeroDefinition();
  G4Eta::EtaDefinition();
  G4EtaPrime::EtaPrimeDefinition();
  G4KaonPlus::KaonPlusDefinition();
  G4KaonMinus::KaonMinusDefinition();
  G4KaonZero::KaonZeroDefinition();
  G4AntiKaonZero::AntiKaonZeroDefinition();
  G4KaonZeroLong::KaonZeroLongDefinition();
  G4KaonZeroShort::KaonZeroShortDefinition();
}

//....oooOOOOOooo........oooOOOOOooo........oooOOOOOooo........oooOOOOOooo......

void BeamTestPhysicsList::ConstructBaryons()
{
  //  barions
  G4Proton::ProtonDefinition();
```

```
  G4AntiProton::AntiProtonDefinition();

  G4Neutron::NeutronDefinition();
  G4AntiNeutron::AntiNeutronDefinition();
}

//....oooOO0OOooo........oooOO0OOooo........oooOO0OOooo........oooOO0OOooo......

void BeamTestPhysicsList::ConstructProcess()
{
  AddTransportation();
  ConstructEM();
  ConstructGeneral();
   AddStepMax();
}


//....oooOO0OOooo........oooOO0OOooo........oooOO0OOooo........oooOO0OOooo......

#include "G4PhysicsListHelper.hh"

#include "G4ComptonScattering.hh"
#include "G4PenelopeComptonModel.hh"

#include "G4GammaConversion.hh"
#include "G4PenelopeGammaConversionModel.hh"

#include "G4PhotoElectricEffect.hh"
#include "G4PenelopePhotoElectricModel.hh"

#include "G4RayleighScattering.hh"
#include "G4PenelopeRayleighModel.hh"

#include "G4eMultipleScattering.hh"
#include "G4eIonisation.hh"
#include "G4PenelopeIonisationModel.hh"

#include "G4eBremsstrahlung.hh"
#include "G4PenelopeBremsstrahlungModel.hh"

#include "G4eplusAnnihilation.hh"
#include "G4PenelopeAnnihilationModel.hh"

#include "G4MuMultipleScattering.hh"
#include "G4MuIonisation.hh"
```

```
#include "G4MuBremsstrahlung.hh"
#include "G4MuPairProduction.hh"

#include "G4hMultipleScattering.hh"
#include "G4hIonisation.hh"
#include "G4hBremsstrahlung.hh"
#include "G4hPairProduction.hh"
#include "G4UniversalFluctuation.hh"

#include "G4ionIonisation.hh"
#include "G4Cerenkov.hh"
#include "G4Scintillation.hh"

//....oooOO0OOooo........oooOO0OOooo........oooOO0OOooo........oooOO0OOooo......

void BeamTestPhysicsList::ConstructEM()
{
   G4PhysicsListHelper* ph = G4PhysicsListHelper::GetPhysicsListHelper();

  theParticleIterator->reset();
  while( (*theParticleIterator)() ){
    G4ParticleDefinition* particle = theParticleIterator->value();
        G4ProcessManager* pmanager = particle->GetProcessManager();
    G4String particleName = particle->GetParticleName();

        G4double highEnergyLimit = 1*GeV;

    if (particleName == "gamma") {
      // gamma
      ph->RegisterProcess(new G4PhotoElectricEffect, particle);
      ph->RegisterProcess(new G4ComptonScattering,   particle);
      ph->RegisterProcess(new G4GammaConversion,     particle);



    } else if (particleName == "e-") {
      //electron
      ph->RegisterProcess(new G4eMultipleScattering, particle);
      ph->RegisterProcess(new G4eIonisation,         particle);
      ph->RegisterProcess(new G4eBremsstrahlung,     particle);


    } else if (particleName == "e+") {
      //positron
      ph->RegisterProcess(new G4eMultipleScattering, particle);
```

```
    ph->RegisterProcess(new G4eIonisation,         particle);
    ph->RegisterProcess(new G4eBremsstrahlung,     particle);
    ph->RegisterProcess(new G4eplusAnnihilation,   particle);



  } else if( particleName == "mu+" ||
             particleName == "mu-"    ) {
    //muon
    ph->RegisterProcess(new G4MuMultipleScattering, particle);
    ph->RegisterProcess(new G4MuIonisation,         particle);
    ph->RegisterProcess(new G4MuBremsstrahlung,     particle);
    ph->RegisterProcess(new G4MuPairProduction,     particle);
    ph->RegisterProcess(new G4Cerenkov,             particle);
    ph->RegisterProcess(new G4Scintillation,        particle);



  } else if( particleName == "proton" ||
             particleName == "pi-" ||
             particleName == "pi+"    ) {
    //proton
    ph->RegisterProcess(new G4hMultipleScattering, particle);
    ph->RegisterProcess(new G4hIonisation,         particle);
    ph->RegisterProcess(new G4hBremsstrahlung,     particle);
    ph->RegisterProcess(new G4hPairProduction,     particle);



  } else if( particleName == "alpha" ||
             particleName == "He3" )     {
    //alpha
    ph->RegisterProcess(new G4hMultipleScattering, particle);
    ph->RegisterProcess(new G4ionIonisation,       particle);

    ph->RegisterProcess(new G4Cerenkov,             particle);
    ph->RegisterProcess(new G4Scintillation,        particle);

  } else if( particleName == "GenericIon" ) {
    //Ions
    ph->RegisterProcess(new G4hMultipleScattering, particle);
    ph->RegisterProcess(new G4ionIonisation,       particle);

    } else if ((!particle->IsShortLived()) &&
               (particle->GetPDGCharge() != 0.0) &&
```

```
              (particle->GetParticleName() != "chargedgeantino")) {
        //all others charged particles except geantino
        ph->RegisterProcess(new G4hMultipleScattering, particle);
        ph->RegisterProcess(new G4hIonisation,         particle);
      }
    }
}

//....oooOO0OOooo........oooOO0OOooo........oooOO0OOooo........oooOO0OOooo......

#include "G4Decay.hh"

void BeamTestPhysicsList::ConstructGeneral()
{
  G4PhysicsListHelper* ph = G4PhysicsListHelper::GetPhysicsListHelper();

  // Add Decay Process
  G4Decay* theDecayProcess = new G4Decay();
  theParticleIterator->reset();
  while( (*theParticleIterator)() ){
    G4ParticleDefinition* particle = theParticleIterator->value();
    if (theDecayProcess->IsApplicable(*particle)) {
      ph->RegisterProcess(theDecayProcess, particle);
    }
  }
}

//....oooOO0OOooo........oooOO0OOooo........oooOO0OOooo........oooOO0OOooo......
#include "G4StepLimiter.hh"
#include "G4UserSpecialCuts.hh"
void BeamTestPhysicsList::AddStepMax()
{
  // Step limitation seen as a process
  G4StepLimiter* stepLimiter = new G4StepLimiter();
  ////G4UserSpecialCuts* userCuts = new G4UserSpecialCuts();

  theParticleIterator->reset();
  while ((*theParticleIterator)()){
      G4ParticleDefinition* particle = theParticleIterator->value();
      G4ProcessManager* pmanager = particle->GetProcessManager();

      if (particle->GetPDGCharge() != 0.0)
        {
          pmanager ->AddDiscreteProcess(stepLimiter);
          ////pmanager ->AddDiscreteProcess(userCuts);
```

```
        }
  }
}
void BeamTestPhysicsList::SetCuts()
{
  if (verboseLevel >0){
    G4cout << "BeamTestPhysicsList::SetCuts:";
    G4cout << "CutLength : " << G4BestUnit(defaultCutValue,"Length") << G4endl;
  }

  // set cut values for gamma at first and for e- second and next for e+,
  // because some processes for e+/e- need cut values for gamma
  //
 SetCutsWithDefault();

  if (verboseLevel>0) DumpCutValuesTable();
}

//....oooOOOOOooo........oooOOOOOooo........oooOOOOOooo........oooOOOOOooo......
```

Appendix C

Galileo SSI Geant4 Runs

Tables C.1, C.2, C.3, C.4, and C.5 are the results from five Geant4 simulations of one billion electrons with energies 1, 3, 5, 10, 30, 50, 100, and 200 MeV for particles that reach the SSI detector and deposit energy. Columns B and C are the numbers of unique primary and secondary particles that deposit energy on the detector, respectively, and their sum is in Column D. Column E is the ratio of the number of secondaries to the number of primaries. In general, the ratio of higher order particles to primary particles is less than 10%, which is consistent with Becker et al. (2017a, 2017b) [11, 12]. Column F is the total number of pixels with energy deposition ("hits") and Column H is the ratio of particles to pixel hits (Column D divided by Column F). Column G is the percentage of the 800 by 800 pixel array that has energy deposited.

Table C.1: SSI Geant4 Run 1

A	B	C	D	E	F	G	H
Energy [MeV]	# Hits from Primaries	# Hits from Secondaries	# Particles that Reach Detector (B+C)	Ratio of Secondaries to Primaries (C/B)	# of Pixels with Energy Deposited, P_0	Percent of 800 x 800 array	Particles per Pixels (D/F)
1	0	0	0	–	0	0.00	–
3	0	6	6	–	11	0.00	0.55
5	1	19	20	19.00	57	0.01	0.35
10	37	91	128	2.46	241	0.04	0.53
30	329	1063	1392	3.23	2529	0.40	0.55
50	626	2544	3170	4.06	5910	0.92	0.54
100	1197	8063	9260	6.74	17742	2.77	0.52
200	1975	20573	22548	10.42	44281	6.92	0.51

Table C.2: SSI Geant4 Run 2

A	B	C	D	E	F	G	H
Energy [MeV]	# Hits from Primaries	# Hits from Secondaries	# Particles that Reach Detector (B+C)	Ratio of Secondaries to Primaries (C/B)	# of Pixels with Energy Deposited, P_0	Percent of 800 x 800 array	Particles per Pixels (D/F)
1	0	0	0	–	0	0.00	–
3	0	3	3	–	11	0.00	0.27
5	0	16	16	–	26	0.00	0.62
10	48	99	147	2.06	225	0.04	0.65
30	296	1001	1297	3.38	2489	0.39	0.52
50	622	2661	3283	4.28	6151	0.96	0.53
100	1144	7989	9133	6.98	18263	2.85	0.50
200	1999	20496	22495	10.25	44650	6.98	0.50

Table C.3: SSI Geant4 Run 3

A	B	C	D	E	F	G	H
Energy [MeV]	# Hits from Primaries	# Hits from Secondaries	# Particles that Reach Detector (B+C)	Ratio of Secondaries to Primaries (C/B)	# of Pixels with Energy Deposited, P_0	Percent of 800 x 800 array	Particles per Pixels (D/F)
1	0	0	0	–	0	0.00	–
3	0	2	2	–	5	0.00	0.4
5	0	9	9	–	20	0.00	0.45
10	49	99	148	2.02	243	0.04	0.61
30	309	943	1252	3.05	2523	0.39	0.50
50	633	2554	3187	4.03	6226	0.97	0.51
100	1159	8039	9198	6.94	18442	2.88	0.50
200	1977	20833	22810	10.54	45525	7.11	0.50

Table C.4: SSI Geant4 Run 4

A	B	C	D	E	F	G	H
Energy [MeV]	# Hits from Primaries	# Hits from Secondaries	# Particles that Reach Detector (B+C)	Ratio of Secondaries to Primaries (C/B)	# of Pixels with Energy Deposited, P_0	Percent of 800 x 800 array	Particles per Pixels (D/F)
1	0	0	0	–	0	0	–
3	0	1	1	–	1	0.00	1
5	1	12	13	12	22	0.00	0.59
10	37	113	150	3.05	233	0.04	0.64
30	307	1040	1347	3.39	2612	0.41	0.52
50	581	2539	3120	4.37	5843	0.91	0.53
100	1211	8022	9233	6.62	17992	2.81	0.51
200	2004	20467	22471	10.21	44464	6.95	0.51

Table C.5: SSI Geant4 Run 5

A	B	C	D	E	F	G	H
Energy [MeV]	# Hits from Primaries	# Hits from Secondaries	# Particles that Reach Detector (B+C)	Ratio of Secondaries to Primaries (C/B)	# of Pixels with Energy Deposited, P_0	Percent of 800 x 800 array	Particles per Pixels (D/F)
1	0	0	0	–	0	0	–
3	0	2	2	–	2	0.00	1
5	1	10	11	10	27	0.00	0.41
10	36	104	140	2.89	261	0.04	0.54
30	301	1027	1328	3.41	2510	0.39	0.53
50	595	2608	3203	4.38	6177	0.97	0.52
100	1115	7921	9036	7.10	17505	2.74	0.52
200	1903	20642	22545	10.85	45065	7.04	0.50

Appendix D

Galileo SSI Data Processing Notes

D.1 Frame Modes and Integration Time

Each SSI frame sequence is comprised of a prepare cycle and a readout cycle, as shown in Figure D-1. The prepare cycle begins with a reset of the shutter position to guarantee its closed position, the filter wheel is stepped (if commanded), the array is readout quickly to reduce dark current, and the shutter is activated to expose the image. The radiation exposure time (called "Integration Time" in Figure D-1) is dominated by the readout cycle, when the shutter is closed. Therefore, we model the SSI in Geant4 with the shutter closed: two Aluminum elements with thicknesses of 5 mm and 2 mm.

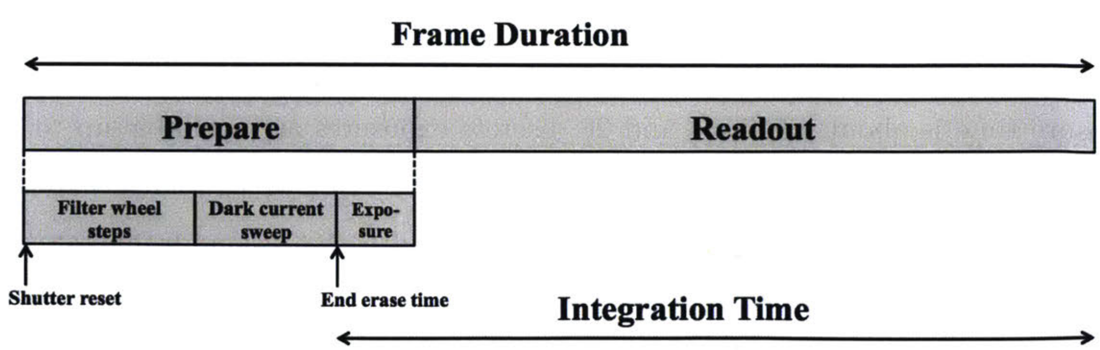

Figure D-1: SSI frame sequence. This figure has been adapted from [26]. The "Integration Time" is the time that the image is exposed to radiation. Note: There is no dark current sweep for the 2-1/3 second mode.

Table D.1: Imaging modes available for the SSI. Each frame contains a prepare and readout time, which is the total imaging mode time. "End of Erase Time" is the starting point of the integration time. There is no dark current sweep for the 2-1/3 second mode.

Imaging Modes	2-1/3 sec	8-2/3 sec	30-1/3 sec	60-2/3 sec
Readout Time	1.667 sec	6.667 sec	26.667 sec	53.333 sec
Prepare Time	0.667 sec	2 sec	3.667 sec	7.333 sec
End of Erase Time	N/A	1.14167 sec	2.80833 sec	6.475 sec
Filter Steps Allowed	1	2	3	7

There are four imaging modes available for the SSI, shown in Table D.1 with the time allocated to the prepare and readout cycles. The starting point of the integration time is at the conclusion of the CCD pre-exposure erase cycle, which occurs within the prepare cycle and shown in Table D.1 as "End of Erase Time". The integration time, t_L, for each line, L, is then given by:

$$t_L = (t_{\text{FrameDuration}} - t_{\text{Prep}}) * (L/800) + (t_{\text{Prep}} - t_{\text{EndEraseTime}}) \tag{D.1}$$

Eq. D.1 is used to compute the integration times for the flux calculations.

There are two exposure types: normal and extended. Exposures longer than 800 milliseconds for full frame images are taken in "Extended" mode. The minimum exposure time is about 4.167 ms and 28 discrete exposures are available up to 800 ms in "normal" exposure model, and from 1.067 s up to 51.2 s in "extended" exposure mode. For summation mode taken at 2-1/3 second and 15-1/6 second frame rates, all exposures greater than 400 ms and 533 ms, respectively, may be taken in extended exposure mode. For "extended" exposures, the exposure extends into what would be the read out time of the frame cycle. In this case, the image is not read out until the next frame cycle, and will have a correspondingly larger dark current, radiation exposure (integration time), etc.

D.2 Target Glow

In the SSI images, there is a "glow" surrounding a target that must be removed, lest it is considered radiation. This is why the technique described in Section 4.3.3 requires the background converges to a constant rate. To demonstrate this, Figure D-2 shows the glow after the target has been removed. The glow could be due to internal reflections within the telescope, albedo from the target, or relativistic electrons scattering. Future work will look into this further.

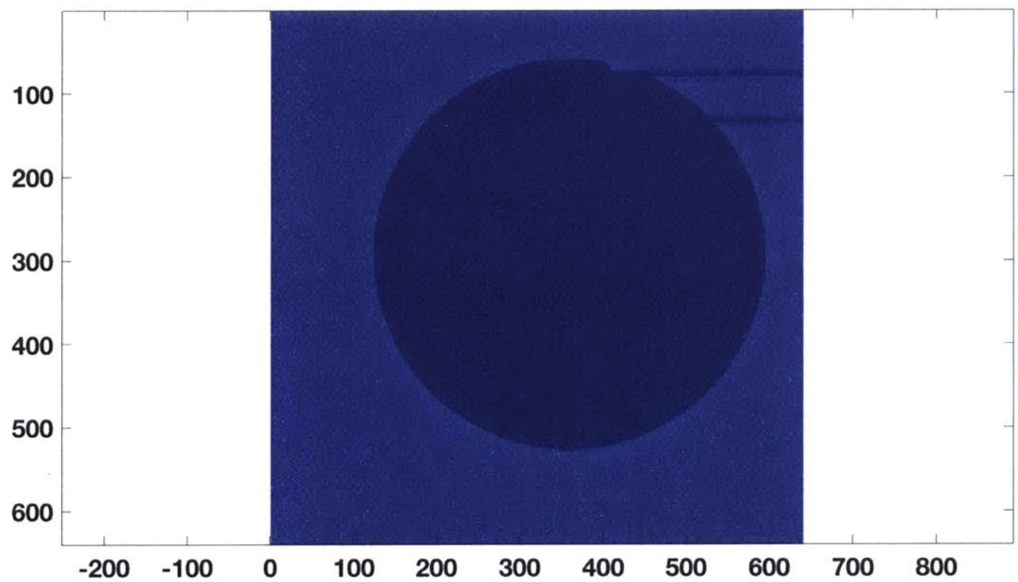

Figure D-2: Residual glow in a SSI image even after the target has been removed.

Bibliography

[1] Alberto Adriani, Gianrico Filacchione, Tatiana Di Iorio, Diego Turrini, Raffaella Noschese, Andrea Cicchetti, Davide Grassi, Alessandro Mura, Giuseppe Sindoni, Massimo Zambelli, et al. JIRAM, the Jovian infrared auroral mapper. *Space Science Reviews*, 213(1-4):393–446, 2017.

[2] S. Agostinelli, J. Allison, K. Amako, J. Apostolakis, H. Araujo, P. Arce, M. Asai, D. Axen, S. Banerjee, G. Barrand, F. Behner, L. Bellagamba, J. Boudreau, L. Broglia, A. Brunengo, H. Burkhardt, S. Chauvie, J. Chuma, R. Chytracek, G. Cooperman, G. Cosmo, P. Degtyarenko, A. Dell'Acqua, G. Depaola, D. Dietrich, R. Enami, A. Feliciello, C. Ferguson, H. Fesefeldt, G. Folger, F. Foppiano, A. Forti, S. Garelli, S. Giani, R. Giannitrapani, D. Gibin, J.J. Gómez Cadenas, I. González, G. Gracia Abril, G. Greeniaus, W. Greiner, V. Grichine, A. Grossheim, S. Guatelli, P. Gumplinger, R. Hamatsu, K. Hashimoto, H. Hasui, A. Heikkinen, A. Howard, V. Ivanchenko, A. Johnson, F.W. Jones, J. Kallenbach, N. Kanaya, M. Kawabata, Y. Kawabata, M. Kawaguti, S. Kelner, P. Kent, A. Kimura, T. Kodama, R. Kokoulin, M. Kossov, H. Kurashige, E. Lamanna, T. LampÃĺn, V. Lara, V. Lefebure, F. Lei, M. Liendl, W. Lockman, F. Longo, S. Magni, M. Maire, E. Medernach, K. Minamimoto, P. Mora de Freitas, Y. Morita, K. Murakami, M. Nagamatu, R. Nartallo, P. Nieminen, T. Nishimura, K. Ohtsubo, M. Okamura, S. O'Neale, Y. Oohata, K. Paech, J. Perl, A. Pfeiffer, M.G. Pia, F. Ranjard, A. Rybin, S. Sadilov, E. Di Salvo, G. Santin, T. Sasaki, N. Savvas, Y. Sawada, S. Scherer, S. Sei, V. Sirotenko, D. Smith, N. Starkov, H. Stoecker, J. Sulkimo, M. Takahata, S. Tanaka, E. Tcherniaev, E. Safai Tehrani, M. Tropeano, P. Truscott, H. Uno, L. Urban, P. Urban, M. Verderi, A. Walkden, W. Wander, H. Weber, J.P. Wellisch, T. Wenaus, D.C. Williams, D. Wright, T. Yamada, H. Yoshida, and D. Zschiesche. Geant4–a simulation toolkit. *Nuclear Instruments and Methods in Physics Research Section A: Accelerators, Spectrometers, Detectors and Associated Equipment*, 506(3):250–303, 2003.

[3] Jay Anderson and Luigi R. Bedin. An empirical pixel-based correction for imperfect CTE. I. HST's advanced camera for surveys. *Publications of the Astronomical Society of the Pacific*, 122(895):1035, 2010.

[4] Louis Archambault, Tina Marie Briere, and Sam Beddar. Transient noise characterization and filtration in CCD cameras exposed to stray radiation from a medical linear accelerator. *Medical physics*, 35(10):4342–4351, 2008.

[5] F. Bagenal and S. Bartlett. Jupiter's Magnetosphere. `http://lasp.colorado.edu/home/mop/resources/graphics/graphics/`. Accessed: 2018-02-22.

[6] Fran Bagenal, Timothy E. Dowling, and William McKinnon, editors. *Jupiter: The Planet, Satellites and Magnetosphere.* Cambridge University Press, New York, 2004. ISBN 0-521-81808-7.

[7] Gary Bailey. Design And Test Of The Near Infrared Mapping Spectrometer (NIMS) Focal Plane For The Galileo Jupiter Orbiter Mission. In *Proc. SPIE*, volume 197, pages 210–216, 1979.

[8] Daniel N. Baker. The Occurrence of Operational Anomalies in Spacecraft and Their Relationship to Space Weather. *IEEE Transactions on Plasma Science*, 28(6), 2000. doi:10.1109/27.902228.

[9] Los Angeles Air Force Base. GPS IIF. `http://www.losangeles.af.mil/About-Us/Fact-Sheets/Article/343724/gps-iif/`. Accessed: 2018-07-31.

[10] Wolfgang Baumjohann and Rudolf Treumann. *Basic Space Plasma Physics.* Imperial College Press, London, 2012.

[11] Heidi N. Becker, J.W. Alexander, A. Adriani, A. Mura, A. Cicchetti, R. Noschese, John Leif Jørgensen, Troelz Denver, Julia Sushkova, A. Jørgensen, et al. The Juno Radiation Monitoring (RM) Investigation. *Space Science Reviews*, 213(1-4):507–545, 2017.

[12] Heidi N. Becker, Daniel Santos-Costa, John L. Jørgensen, Troelz Denver, Alberto Adriani, Alessandro Mura, John E.P. Connerney, Scott J. Bolton, Steven M. Levin, Richard M. Thorne, et al. Observations of MeV electrons in Jupiter's innermost radiation belts and polar regions by the Juno radiation monitoring investigation: Perijoves 1 and 3. *Geophysical Research Letters*, 44(10):4481–4488, 2017.

[13] Michael J.S. Belton, Kenneth P. Klaasen, Maurice C. Clary, James L. Anderson, Clifford D. Anger, Michael H. Carr, Clark R. Chapman, Merton E. Davies, Ronald Greeley, Donald Anderson, Lawrence K. Bolef, Timothy E. Townsend, Richard Greenberg, James W. Head, Gerhard Neukum, Carl B. Pilcher, Joseph Veverka, Peter J. Gierasch, Fraser P. Fanale, Andrew P. Ingersoll, Harold Masursky, David Morrison, and James B. Pollack. The Galileo Solid-State Imaging experiment. *Space Science Reviews*, 60(1):413–455, 1992.

[14] D.L. Blaney, C. Hibbitts, R.N. Clark, J.B. Dalton, III, A.G. Davies, R.O. Green, M.M. Hedman, Y. Langevin, J.I. Lunine, T.B. McCord, S.L. Murchie, C. Paranicas, F.P. Seelos, IV, J.M. Soderblom, and M.L. Cable. The Mapping Imaging Spectrometer for Europa (MISE) Investigation. *AGU Fall Meeting Abstracts*, pages P13E–04, December 2015.

[15] S.J. Bolton, M. Janssen, R. Thorne, S. Levin, M. Klein, S. Gulkis, T. Bastian, R. Sault, C. Elachi, M. Hofstadter, A. Bunker, G. Dulk, E. Gudim, G. Hamilton, W.T.K. Johnson, Y. Leblanc, O. Liepack, R. McLeod, J. Roller, L. Roth, and R. West. Ultra-relativistic electrons in Jupiter's radiation belts. *Nature*, 415(6875):987–991, 2002.

[16] Marty Brennan and Stuart Stephens. Juno Orbit Geometry. `http://lasp.colorado.edu/home/mop/files/2018/06/Orbit_Geometry_Graphics_MJB_180302.pdf`. Accessed: 2018-07-31.

[17] T.G. Brockwell, K.J. Meech, K. Pickens, J.H. Waite, G.Miller, J.Roberts, J.I. Lunine, and P. Wilson. The mass spectrometer for planetary exploration (MASPEX). In *2016 IEEE Aerospace Conference*, pages 1–17, March 2016.

[18] A. Bross. Investigation of the use of charge coupled devices as high resolution position sensitive detectors of ionizing radiation. In *Proc. International Conference on Instrumentation for Colliding Beam Physics*, number 250, pages 51–55, Stanford Linear Accelerator Center, Stanford, California, 1982.

[19] W.L. Brown and J.D. Gabbe. The Electron Distribution in the Earth's Radiation Belts during July 1962 as Measured by Telstar. *Journal of Geophysical Research*, 68(3):607–618, March 1963. doi:10.1029/JZ068i003p00607.

[20] B.E. Burke, R.D. Petrasso, C.K. Li, and T.C. Hotaling. Use of charge-coupled device imagers for charged-particle spectroscopy. *Review of Scientific Instruments*, 68(1):599–602, 1997.

[21] David C. Byers and John W. Dankanich. Geosynchronous-Earth-Orbit Communication Satellite Deliveries with Integrated Electric Propulsion. 24(6):1369–1375, 2008.

[22] R.W. Carlson and K.P. Hand. Radiation Noise Effects at Jupiter's Moon Europa: In-Situ and Laboratory Measurements and Radiation Transport Calculations. *IEEE Transactions on Nuclear Science*, 62(5):2273–2282, 2015.

[23] R.W. Carlson, P.R. Weissman, W.D. Smythe, J.C. Mahoney, et al. Near-infrared mapping spectrometer experiment on Galileo. In *The Galileo Mission*, pages 457–502. Springer Netherlands, Dordrecht, 1992.

[24] Dakai Chen, James D. Forney, Ronald L. Pease, Anthony M. Phan, Martin A. Carts, Stephen R. Cox, Kirby Kruckmeyer, Sam Burns, Rafi Albarian, Bruce Holcombe, Bradley Little, James Salzman, Geraldine Chaumont, Herve Duperray, Al Ouellet, and Kenneth LaBel. The Effects of ELDRS at Ultra-Low Dose Rates. In *IEEE Radiation Effects Data Workshop*, Denver, CO, July 2010. doi:10.1109/REDW.2010.5619506.

[25] Christopher F. Chyba and Cynthia B. Phillips. Possible Ecosystems and the Search for Life on Europa. *Proceedings of the National Academy of Sciences of the United States of America*, 98(3):801–804, 2001.

[26] M.C. Clary, K.P. Klaasen, L.M. Snyder, and P.K. Wang. 800 x 800 Charge-Coupled Device (CCD) Camera For The Galileo Jupiter Orbiter Mission. In *Proc. SPIE*, volume 203, pages 98–109, 1979.

[27] John E.P. Connerney, Mario H. Acuña, Norman F. Ness, and Tsuyoshi Satoh. New models of Jupiter's magnetic field constrained by the Io flux tube footprint. *Journal of Geophysical Research: Space Physics*, 103(A6):11929–11939, 1998.

[28] John F. Cooper, Robert E. Johnson, Barry H. Mauk, Henry B. Garrett, and Neil Gehrels. Energetic Ion and Electron Irradiation of the Icy Galilean Satellites. *Icarus*, 149(1):133–159, 2001.

[29] E.J. Daly, A. Hilgers, G. Drolshagen, and Hugh Evans. Space Environment Analysis: Experience and Trends. In *Environment Modelling for Space-based Applications, Symposium Proceedings (ESA SP-392)*, Noordwijk, The Netherlands, 9 1996. doi:10.1007/978-94-015-9395-3.

[30] Taher Daud, James R. Janesick, Kenneth Evans, and Tom Elliott. Charge-Coupled-Device Response to Electron Beam Energies of less than 1 keV up to 20 keV. *Optical Engineering*, 26(8), 1987.

[31] Michael W. Davidson. Understanding Digital Imaging. `http://zeiss-campus.magnet.fsu.edu/print/basics/digitalimaging-print.html`. Accessed: 2018-06-27.

[32] Imke de Pater and David E. Dunn. VLA observations of Jupiter's synchrotron radiation at 15 and 22 GHz. *Icarus*, 163(2):449–455, 2003.

[33] Maria de Soria-Santacruz, Henry B. Garrett, Robin W. Evans, Insoo Jun, Wousik Kim, Christopher Paranicas, and A. Drozdov. An empirical model of the high-energy electron environment at Jupiter. *Journal of Geophysical Research: Space Physics*, 121(10):9732–9743, 2016.

[34] Maria de Soria-Santacruz Pich, Henry B. Garrett, Robin W. Evans, Insoo Jun, Wousik Kim, and Christopher Paranicas. The GIRE2 model and its application to the Europa mission. In *2016 IEEE Aerospace Conference*, pages 1–7, 2016.

[35] Leonid V. Didkovsky, D.L. Judge, A.R. Jones, E.J. Rhodes, and J.B. Gurman. Measuring proton energies and fluxes using EIT (SOHO) CCD areas outside the solar disk images. *Astronomische Nachrichten*, 327(4):314–320, 2006.

[36] Neil Divine and Henry B. Garrett. Charged particle distributions in Jupiter's magnetosphere. *Journal of Geophysical Research: Space Physics*, 88(A9):6889–6903, 1983.

[37] Mehlman et al. Introduction to the Galileo Near-Infrared Mapping Spectrometer (NIMS) Cube CD-ROM Set, Version 2.2. `https://pdsimage2.wr.usgs.gov/archive/go-j-nims-3-tube-v1.0/go_1116/document/volinfo.txt`, 2001.

[38] Joseph Fennell, H.C. Koons, Jim Roeder, and J.B. Blake. Spacecraft Charging: Observations and Relationships to Satellite Anomalies. Aerospace Report tr-2001(8570)-5, Aerospace Corporation, El Segundo, CA, 2001.

[39] Paul D. Fieseler. *The Galileo Star Scanner as an Instrument for Measuring Energetic Electrons in the Jovian Environment.* PhD thesis, University of Southern California, 2000.

[40] Paul D. Fieseler, S. M. Ardalan, and A. R. Frederickson. The radiation effects on Galileo spacecraft systems at Jupiter. *IEEE Transactions on Nuclear Science*, 49(6), 2002. doi:10.1109/TNS.2002.805386.

[41] A. Fludra. Modulation of Galactic Cosmic Rays Observed at L1 in Solar Cycle 23. *The Astrophysical Journal*, 799(1):31, 2015.

[42] Peter G. Ford and Catherine E. Grant. Using the Chandra ACIS X-ray imager as a background particle flux detector. In *Space Telescopes and Instrumentation 2012: Ultraviolet to Gamma Ray*, volume 8443. International Society for Optics and Photonics, 2012.

[43] Arthur R. Frederickson. Upsets Related to Spacecraft Charging. *IEEE Transactions on Nuclear Science*, 23(2):426–441, 1996. doi:10.1109/23.490891.

[44] Henry Garrett and Albert Whittlesey. *Guide to Mitigating Spacecraft Charging Effects.* JPL Space Science and Technology Series. John Wiley & Sons, Inc., Pasadena, CA, May 2012.

[45] Henry B. Garrett, Insoo Jun, Martin J. Ratliff, Robin W. Evans, G.A. Clough, and R.W. McEntire. Galileo Interim Radiation Model, JPL Publication 03-006. Technical report, Jet Propulsion Laboratory, National Aeronautics and Space Administration, Pasadena, CA, 2002.

[46] Henry B. Garrett, Ira Katz, Insoo Jun, Wousik Kim, Albert C. Whittlesey, and Robin W. Evans. The Jovian Charging Environment and Its Effects – A Review. *IEEE Transactions on Plasma Science*, 40(2):144–154, 2012.

[47] Henry B. Garrett, Steven M. Levin, Scott J. Bolton, Robin W. Evans, and Bidushi Bhattacharya. A revised model of Jupiter's inner electron belts: Updating the Divine radiation model. *Geophysical Research Letters*, 32(4), 2005. L04104.

[48] G. Randall Gladstone, Steven C. Persyn, John S. Eterno, Brandon C. Walther, David C. Slater, Michael W. Davis, Maarten H. Versteeg, Kristian B. Persson, Michael K. Young, Gregory J. Dirks, Anthony O. Sawka, Jessica Tumlinson, Henry Sykes, John Beshears, Cherie L. Rhoad, James P. Cravens, Gregory S. Winters, Robert A. Klar, Walter Lockhart, Benjamin M. Piepgrass, Thomas K. Greathouse, Bradley J. Trantham, Philip M. Wilcox, Matthew W. Jackson, Oswald H. W. Siegmund, John V. Vallerga, Rick Raffanti, Adrian Martin, J.-C.

Gérard, Denis C. Grodent, Bertrand Bonfond, Benoit Marquet, and François Denis. The Ultraviolet Spectrograph on NASA's Juno Mission. *Space Science Reviews*, 213(1):447–473, 2017.

[49] Barry Goldstein, Robert Pappalardo, Brian Cooke, Tom Magner, Louise Prockter, and David Senske. Europa Clipper Update. Presentation at the Europa Clipper OPAG, unpublished. `https://www.lpi.usra.edu/opag/meetings/jan2014/presentations/9_Clipper.pdf`, January 2014.

[50] Catherine E. Grant, B. Lamarr, M. W. Bautz, and S.L. O'Dell. Using ACIS on the Chandra X-ray Observatory as a particle radiation monitor II. *Space Telescopes and Instrumentation 2012: Ultraviolet to Gamma Ray*, 8443, 2012.

[51] Catherine E. Grant, B. Lamarr, M.W. Bautz, and S.L. O'Dell. Using ACIS on the Chandra X-ray Observatory as a particle radiation monitor. *Space Telescopes and Instrumentation 2010: Ultraviolet to Gamma Ray*, 7732:80, 2010.

[52] P. Hand, Christopher F. Chyba, J.C. Priscu, R.W. Carlson, and K.H. Nealson. Astrobiology and the potential for life on Europa. In Pappalardo et al. [87], part V, pages 589–629.

[53] C.J. Hansen, M.A. Caplinger, A. Ingersoll, M. A. Ravine, E. Jensen, S. Bolton, and G. Orton. JunoCam: Juno's Outreach Camera. *Space Science Reviews*, 213(1):475–506, 2017.

[54] Daniel Hastings and Henry Garrett. *Spacecraft-Environment Interactions*. Cambridge Atmospheric and Space Science Series. Cambridge University Press, Cambridge, UK, 1996.

[55] Wilmot N. Hess. The Effects of High Altitude Explosions. Technical Report TN D-2402, National Aeronautics and Space Administration, 1964.

[56] D.G. Hicks, C.K. Li, R.D. Petrasso, F.H. Séguin, B.E. Burke, J.P. Knauer, S. Cremer, R.L. Kremens, M.D. Cable, and T.W. Phillips. Design of an electronic charged particle spectrometer to measure $<\rho\mathrm{R}>$ on inertial fusion experiments. *Review of Scientific Instruments*, 68(1):589–592, 1997.

[57] James R. Janesick. *Scientific Charge-Coupled Devices*, volume PM83. SPIE Press, Bellingham, Washington, 2001.

[58] James R. Janesick, J. Hynecek, and M.M. Blouke. Virtual phase imager for Galileo. In *Solid-State Imagers for Astronomy*, volume 290, pages 165–174. International Society for Optics and Photonics, 1981.

[59] S.E. Jaskulek, R.E. Gold, and R.W. McEntire. Spaceborne energetic particle instrumentation. *Johns Hopkins APL Technical Digest*, 6:20–27, 1985.

[60] Michael R. Johnson. The Galileo High Gain Antenna Deployment Anomaly. Technical Report N94-33319, California Institute of Technology, Jet Propulsion Laboratory, Pasadena, CA, 1994.

[61] R.E. Johnson, M.H. Burger, T.A. Cassidy, F. Leblanc, M. Marconi, and W.H. Smyth. Composition and detection of Europa's sputter-induced atmosphere. In Pappalardo et al. [87], part IV, pages 507–527.

[62] R.E. Johnson, R.W. Carlson, J.F. Cooper, C. Paranicas, M.H. Moore, and M.C. Wong. Radiation effects on the surfaces of the Galilean satellites. In Bagenal et al. [6], chapter 20, pages 485–512.

[63] T.V. Johnson and L.A. Soderblom. Volcanic Eruptions on Io: Implications for Surface Evolution and Mass Loss. In *IAU Colloq. 57: Satellites of Jupiter*, page 634, 1981.

[64] T.M. Jordan. Report No. EMPC 97.01. 02.01. *NOVICE: A radiation transport/shielding code: Users guide*, 1997. `https://empc.com/novice-software/`.

[65] Insoo Jun, Henry B. Garrett, Randall Swimm, Robin W. Evans, and Gene Clough. Statistics of the variations of the high-energy electron population between 7 and 28 Jovian radii as measured by the Galileo spacecraft. *Icarus*, 178(2):386–394, 2005.

[66] Insoo Jun, Shawn Kang, Robin Evans, Michael Cherng, and Randall Swimm. Radiation Transport Tools for Space Applications: A Review. In *5th Geant4 Space Users' Workshop*, Tokyo, Japan, 2008.

[67] Insoo Jun, J. Martin Ratliff, Henry B. Garrett, and Robert W. McEntire. Monte Carlo simulations of the Galileo energetic particle detector. *Nuclear Instruments and Methods in Physics Research Section A: Accelerators, Spectrometers, Detectors and Associated Equipment*, 490(3):465–475, 2002.

[68] L. Kamp. Project Galileo Software Interface Specification: Near-Infrared Mapping Spectrometer Experiment Data Record (NIMS EDR) for Phase 2. Technical Report D-3048, GLL Project 232-08, SFOC0038-02-00-03, SFOC1-MPS-GLL-NIMSEDR, Revision A, 1996.

[69] Krishan K. Khurana, Margaret G. Kivelson, Vytenis M. Vasyliunas, Norbert Krupp, Joachim Woch, Andreas Lagg, Barry Mauk, and William S. Kurth. The Configuration of Jupiter's Magnetosphere. In Bagenal et al. [6], chapter 24, pages 559–616.

[70] Krishan K. Khurana and Hannes K. Schwarzl. Global structure of Jupiter's magnetospheric current sheet. *Journal of Geophysical Research: Space Physics*, 110(A7), 2005. A07227.

[71] Ken Klaasen. Galileo solid-state imaging subsystem calibration report: part 2. JPL Document 1625-210, California Institute of Technology, Jet Propulsion Laboratory, Pasadena, CA, 1993.

[72] Kenneth P. Klaasen, Michael J.S. Belton, H. Herbert Breneman, Alfred S. McEwen, Merton E. Davies, Robert J. Sullivan, Clark R. Chapman, Gerhard Neukum, Catherine M. Heffernan, Ann P. Harch, James M. Kaufman, William J. Merline, Lisa R. Gaddis, William F. Cunningham, Paul Helfenstein, and Timothy R. Colvin. Inflight performance characteristics, calibration, and utilization of the Galileo solid-state imaging camera. *Optical Engineering*, 36(11):3001–3027, 1997.

[73] Kenneth P. Klaasen, H. Herbert Breneman, William F. Cunningham, James M. Kaufman, James E. Klemaszewski, Kari P. Magee, Alfred S. McEwen, Helen B. Mortensen, Robert T. Pappalardo, David A. Senske, et al. Calibration and performance of the Galileo solid-state imaging system in Jupiter orbit. *Optical Engineering*, 38(7):1178–1200, 1999.

[74] Kenneth P. Klaasen, H. Herbert Breneman, Amy Simon-Miller, Donald J. Banfield, and Greg C. Levanas. Operations and calibration of the solid-state imaging system during the Galileo extended mission at Jupiter. *Optical Engineering*, 42(2):494–510, 2003.

[75] Kenneth P. Klaasen, Maurice C. Clary, and James R. Janesick. Charge-Coupled Device Television Camera For NASA's Galileo Mission To Jupiter. *Optical Engineering*, 23(3), 1984.

[76] Claude A. Klein. Bandgap dependence and related features of radiation ionization energies in semiconductors. *Journal of Applied Physics*, 39(4):2029–2038, 1968. doi: 10.1063/1.1656484.

[77] Norbert Krupp, Vytenis M. Vasyliunas, Joachim Woch, Andreas Lagg, Krishan K. Khurana, Margaret G. Kivelson, Barry H. Mauk, E.C. Roelof, D.J. Williams, S.M. Krimigis, William S. Kurth, L.A. Frank, and W.R. Paterson. Dynamics of the Jovian Magnetosphere. In Bagenal et al. [6], chapter 25, pages 617–638.

[78] Hugh de Lacy and Alun Jones. Shrinking Silicon Feature Sizes: Consequences for Reliability. In *Conference for Military and Space Electronics (CSME)*, Portsmouth, UK, 2008.

[79] C.K. Li, D. G. Hicks, R.D. Petrasso, F.H. Seguin, M.D. Cable, T.W. Phillips, T.C. Sangster, J.P. Knauer, S. Cremer, and R.L. Kremens. Charged-coupled devices for charged-particle spectroscopy on OMEGA and NOVA. *Review of Scientific Instruments*, 68(1):593–595, 1997.

[80] Giles M. Marion, Christian H. Fritsen, Hajo Eicken, and Meredith C. Payne. The Search for Life on Europa: Limiting Environmental Factors,

Potential Habitats, and Earth Analogues. *Astrobiology*, 3(4):785–811, 2003. doi:10.1089/153110703322736105.

[81] G.W. McKinney, D.J. Lawrence, T.H. Prettyman, R.C. Elphic, W.C. Feldman, and J.J. Hagerty. MCNPX benchmark for cosmic ray interactions with the Moon. *Journal of Geophysical Research: Planets*, 111(E6), 2006.

[82] B. Mehlman, F. Leader, B. Carlson, B. Smythe, L. Kamp, A. Davies, V. Henderson, T. Brown, E. Eliason, and C. Isbell. VOLINFO.txt., Version 2.1 (G2 encounter) In: Mission to Jupiter. Galileo NIMS Gaspra, Ida, SL9 & Ganymede 1 Encounters, Spectral Image Cubes and Browse Products. `https://pds-imaging.jpl.nasa.gov/data/go-j-nims-3-tube-v1.0/go_1112/document/volinfo.txt`, 1999.

[83] National Aeronautics and Space Administration. JunoCAM. `https://www.missionjuno.swri.edu/junocam/`. Accessed: 2018-06-20.

[84] Q. Nénon, A. Sicard, P. Kollmann, H.B. Garrett, S.P.A. Sauer, and C. Paranicas. A Physical Model of the Proton Radiation Belts of Jupiter inside Europa's Orbit. *Journal of Geophysical Research: Space Physics*, 123(5):3512–3532, 2018.

[85] National Oceanic, Atmospheric Administration, National Aeronautics, and Space Administration. Geostationary Operational Environmental Satellite - R Series. `https://www.goes-r.gov/org/contacts.html`. Accessed: 2018-07-28.

[86] National Institute of Standards and Technology. ESTAR: Stopping-Power and Range Tables for Electrons. `https://physics.nist.gov/PhysRefData/Star/Text/ESTAR.html`. Accessed: 2017-03-14.

[87] Robert T. Pappalardo, William B. McKinnon, and Krishan K. Khurana, editors. *Europa*. Space Science Series. University of Arizona Press, Tucson, 2009.

[88] C. Paranicas, J.F. Cooper, H.B. Garrett, R.E. Johnson, and S.J. Sturner. Europa's Radiation Environment and Its Effects on the Surface. In Pappalardo et al. [87], part IV, pages 529–544.

[89] G. Wesley Patterson, Chris Paranicas, and Louise M. Prockter. Characterizing electron bombardment of Europa's surface by location and depth. *Icarus*, 220(1):286–290, 2012.

[90] J. Perl. HepRep: a Generic Interface Definition for HEP Event Display Representables. Technical Report SLAC-PUB-8332, Stanford University, Palo Alto, CA, 2000.

[91] Cynthia B. Phillips and Robert T. Pappalardo. Europa Clipper Mission Concept: Exploring Jupiter's Ocean Moon. *EoS, Transactions American Geophysical Union*, 95(20):165–167, 2014.

[92] Thibaut Prod'homme, Berry Holl, Lennart Lindegren, and Anthony G.A. Brown. The impact of CCD radiation damage on Gaia astrometry–I. Image location estimation in the presence of radiation damage. *Monthly Notices of the Royal Astronomical Society*, 419(4):2995–3017, 2012.

[93] Geoffrey Reeves, Reiner H.W. Friedel, Brian A. Larsen, Ruth M. Skoug, Herbert O. Funsten, Seth G. Claudepierre, Joseph F. Fennell, Drew L. Turner, Mick H. Denton, Harlan E. Spence, J. Bernard Blake, and Daniel N. Baker. Energy-dependent dynamics of keV to MeV electrons in the inner zone, outer zone, and slot regions. *Journal of Geophysical Research: Space Physics*, 121(1):397–412, 2015.

[94] Geoffrey Reeves, Steve Morley, and Greg Cunningham. Long-Term Variations in Solar Wind Velocity and Radiation Belt Electrons. *Journal of Geophysical Research: Space Physics*, 118:1040–1048, March 2013. doi:10.1002/jgra.50126.

[95] K. D. Retherford, R. Gladstone, T. K. Greathouse, A. Steffl, M. W. Davis, P. D. Feldman, M. A. McGrath, L. Roth, J. Saur, J. R. Spencer, S. A. Stern, S. Pope, M. A. Freeman, S. C. Persyn, M. F. Araujo, S. C. Cortinas, R. M. Monreal, K. B. Persson, B. J. Trantham, M. H. Versteeg, and B. C. Walther. The Ultraviolet Spectrograph on the Europa Mission (Europa-UVS). *AGU Fall Meeting Abstracts*, pages P13E–02, December 2015.

[96] C. T. Russell. Planetary Magnetospheres. *Reports on Progress in Physics*, 56(6):687, 1993.

[97] C.T. Russell. The Dynamics of Planetary Magnetospheres. *Planetary and Space Science*, 49(10-11):1005–1030, 2001. Magnetosphere of the Outer Planets Part II.

[98] Selesnick R. S. Cosmic ray access to Jupiter's magnetosphere. *Geophysical Research Letters*, 29(9):12–1–12–4, 2002.

[99] Satellite Industry Association. State of the Satellite Industry. May 2015. Prepared by The Tauri Group.

[100] D. M. Sawyer and James Vette. AP-8 Trapped Proton Environment for Solar Maximum and Solar Minimum. *NASA STI/Recon Technical Report N*, 77, December 1976.

[101] Z.N. Shen and G. Qin. A study of cosmic ray flux based on the noise in raw CCD data from solar images. *Journal of Geophysical Research: Space Physics*, 121(11):10712–10727, 2016.

[102] Scott Sheppard. The Jupiter Satellite and Moon Page. `http://home.dtm.ciw.edu/users/sheppard/satellites/jupsatdata.html`. Last updated: October 2017. Accessed: 2018-05-30.

[103] Angelica Sicard and Sebastien Bourdarie. Physical Electron Belt Model from Jupiter's surface to the orbit of Europa. *Journal of Geophysical Research: Space Physics*, 109(A2), 2004. A02216.

[104] Angelica Sicard-Piet, Sebastien Bourdarie, and Norbert Krupp. JOSE: A New Jovian Specification Environment Model. *IEEE Transactions on Nuclear Science*, 58(3):923–931, June 2011.

[105] Alan R. Smith, Richard J. McDonald, Donna C. Hurley, Steven E. Holland, Donald E. Groom, William E. Brown, David K. Gilmore, Richard J. Stover, and Mingzhi Wei. Radiation events in astronomical CCD images. In *Proc. SPIE*, volume 4669, pages 172–183, 2002.

[106] A.J. Steffl, A.B. Shinn, G. Randall Gladstone, Joel W. Parker, K.D. Retherford, David C. Slater, Maarten H. Versteeg, and S. Alan Stern. MeV electrons detected by the ALICE UV spectrograph during the New Horizons flyby of Jupiter. *Journal of Geophysical Research: Space Physics*, 117(A10), 2012.

[107] S. Alan Stern, David C. Slater, John Scherrer, John Stone, Greg Dirks, Maarten Versteeg, Michael Davis, G. Randall Gladstone, Joel W. Parker, Leslie A. Young, et al. ALICE: The ultraviolet imaging spectrograph aboard the New Horizons Pluto–Kuiper Belt mission. In *New Horizons*, pages 155–187. Springer, New York, 2009.

[108] James E. Turner. *Atoms, radiation, and radiation protection.* John Wiley & Sons, 2008.

[109] E.P. Turtle, A.S. McEwen, G.C. Collins, L. Fletcher, C.J. Hansen, A.G. Hayes, T.A. Hurford, R.L. Kirk, A.C. Barr Mlinar, F. Nimmo, G.W. Patterson, L.C. Quick, J.M. Soderblom, N. Thomas, and C.M. Ernst. The Europa Imaging System (EIS): High-Resolution Imaging and Topography to Investigate Europa's Geology, Ice Shell, and Potential for Current Activity. In *Lunar and Planetary Science Conference*, volume 47 of *Lunar and Planetary Science Conference*, page 1626, March 2016.

[110] J.A. Van Allen, D.N. Baker, B.A. Randall, M.F. Thomsen, D.D. Sentman, and H.R. Flindt. Energetic electrons in the magnetosphere of Jupiter. *Science*, 183(4122):309–311, 1974.

[111] J.A. Van Allen, B.A. Randall, D.N. Baker, C.K. Goertz, D.D. Sentman, M.F. Thomsen, and H.R. Flindt. Pioneer 11 observations of energetic particles in the Jovian magnetosphere. *Science*, 188(4187):459–462, 1975.

[112] James Vette. The AE-8 Trapped Electron Model Environment. *NASA STI/Recon Technical Report N*, 92, November 1991.

[113] R.E. Vogt, W.R. Cook, A.C. Cummings, T.L. Garrard, N. Gehrels, E.C. Stone, J.H. Trainor, A.W. Schardt, T. Conlon, N. Lal, et al. Voyager 1: Energetic

ions and electrons in the Jovian magnetosphere. *Science*, 204(4396):1003–1007, 1979.

[114] R.E. Vogt, A.C. Cummings, T.L. Garrard, N. Gehrels, E.C. Stone, J.H. Trainor, A.W. Schardt, T.F. Conlon, and F.B. McDonald. Voyager 2: Energetic ions and electrons in the Jovian magnetosphere. *Science*, 206(4421):984–987, 1979.

[115] John G. Webster and Halit Eren, editors. *Measurement, Instrumentation, and Sensors Handbook: Electromagnetic, Optical Radiation, Chemical, and Biological Measurement.* Taylor & Francis Group, LLC, 2nd edition, 2014. ISBN 9781439848838.

[116] D.J. Williams, R.W. McEntire, S. Jaskulek, and B. Wilken. The Galileo Energetic Particles Detector. *Space Science Reviews*, 60(1):385–412, 1992.

[117] Gordon Wrenn. Conclusive Evidence for Internal Dielectric Charging Anomalies on Geosynchronous Communications Spacecraft. *Journal of Spacecraft and Rockets*, 32(3):514–520, May 1995. doi:10.2514/3.26645.

[118] A. Yamashita, T. Dotani, M. Bautz, G. Crew, H. Ezuka, K. Gendreau, T. Kotani, K. Mitsuda, C. Otani, A. Rasmussen, G. Ricker, and H. Tsunemi. Radiation damage to charge coupled devices in the space environment. *IEEE Transactions on Nuclear Science*, 44(3):847–853, June 1997.